



National Library  
of Canada

Acquisitions and  
Bibliographic Services Branch

395 Wellington Street  
Ottawa, Ontario  
K1A 0N4

Bibliothèque nationale  
du Canada

Direction des acquisitions et  
des services bibliographiques

395, rue Wellington  
Ottawa (Ontario)  
K1A 0N4

Your file / Votre référence

Our file / Notre référence

## NOTICE

The quality of this microform is heavily dependent upon the quality of the original thesis submitted for microfilming. Every effort has been made to ensure the highest quality of reproduction possible.

If pages are missing, contact the university which granted the degree.

Some pages may have indistinct print especially if the original pages were typed with a poor typewriter ribbon or if the university sent us an inferior photocopy.

Reproduction in full or in part of this microform is governed by the Canadian Copyright Act, R.S.C. 1970, c. C-30, and subsequent amendments.

## AVIS

La qualité de cette microforme dépend grandement de la qualité de la thèse soumise au microfilmage. Nous avons tout fait pour assurer une qualité supérieure de reproduction.

S'il manque des pages, veuillez communiquer avec l'université qui a conféré le grade.

La qualité d'impression de certaines pages peut laisser à désirer, surtout si les pages originales ont été dactylographiées à l'aide d'un ruban usé ou si l'université nous a fait parvenir une photocopie de qualité inférieure.

La reproduction, même partielle, de cette microforme est soumise à la Loi canadienne sur le droit d'auteur, SRC 1970, c. C-30, et ses amendements subséquents.

**Modelling Study of Nutrients Cycles in the  
North Atlantic Ocean**

by

Lin Su

Department of Atmospheric and Oceanic Sciences

and

Centre for Climate and Global Change Research

McGill University, Montreal

January, 1996

A thesis submitted to the Faculty of Graduate Studies and Research

in partial fulfilment of the requirements for the degree of

Doctor of Philosophy

Copyright by Lin Su, 1996



National Library  
of Canada

Acquisitions and  
Bibliographic Services Branch

395 Wellington Street  
Ottawa, Ontario  
K1A 0N4

Bibliothèque nationale  
du Canada

Direction des acquisitions et  
des services bibliographiques

395, rue Wellington  
Ottawa (Ontario)  
K1A 0N4

Your file / Votre référence

Our file / Notre référence

**The author has granted an irrevocable non-exclusive licence allowing the National Library of Canada to reproduce, loan, distribute or sell copies of his/her thesis by any means and in any form or format, making this thesis available to interested persons.**

**L'auteur a accordé une licence irrévocable et non exclusive permettant à la Bibliothèque nationale du Canada de reproduire, prêter, distribuer ou vendre des copies de sa thèse de quelque manière et sous quelque forme que ce soit pour mettre des exemplaires de cette thèse à la disposition des personnes intéressées.**

**The author retains ownership of the copyright in his/her thesis. Neither the thesis nor substantial extracts from it may be printed or otherwise reproduced without his/her permission.**

**L'auteur conserve la propriété du droit d'auteur qui protège sa thèse. Ni la thèse ni des extraits substantiels de celle-ci ne doivent être imprimés ou autrement reproduits sans son autorisation.**

ISBN 0-612-12491-6

**Canada**

# Contents

<b>List of Table</b>	v
<b>List of Figures</b>	vii
<b>Abstract</b>	xiv
<b>Résumé</b>	xvi
<b>List of Symbols</b>	xviii
<b>List of Abbreviation</b>	xxi
<b>Acknowledgments</b>	xxii
<b>Statement of Originality</b>	xxiv
<b>1 Introduction</b>	1
1.1 An overview .....	1
1.2 New production and downward transport of organic matter .....	3
1.3 Seasonal cycle of oxygen .....	9
1.4 Particle cycling .....	12
1.5 Organization of the thesis .....	17

<b>2 Model description and formulation</b>	<b>20</b>
2.1 Physical model .....	20
2.2 Biological model .....	22
2.3 Model of seasonal oxygen cycle .....	27
2.4 An alternative model of organic particles .....	28
2.5 Summary .....	31
<b>3 Nitrate cycle modelling in the North Atlantic Ocean</b>	<b>38</b>
3.1 Introduction .....	38
3.2 Experiment design .....	41
3.3 Zonal nitrate distribution .....	42
3.4 Meridional transport of nitrate and DON .....	44
3.5 Remineralization and nitrate regeneration .....	47
3.6 Summary .....	50
<b>4 Modelling the seasonal cycle of oxygen in the North Atlantic Ocean</b>	<b>64</b>
4.1 Introduction .....	64
4.2 Model and experimental design .....	66
4.3 Seasonal cycle of oxygen .....	67
4.4 Oxygen flux .....	72
4.5 Summary .....	79

<b>5 Particle cycle modelling in the open ocean</b>	<b>92</b>
5.1 Introduction .....	92
5.2 Analysis of the 1-dimensional Clegg and Whitfield (1990) particle cycling model .....	95
5.3 Numerical results from the 1-dimensional particle cycling model .....	100
5.4 Embedding of the 1-dimensional particle model in the 3-dimensional circulation model .....	105
5.5 Summary .....	109
<b>6 Conclusions</b>	<b>120</b>
<b>Bibliography</b>	<b>124</b>

## List of Tables

Table 2.1	Depths (m) at the bottom, and thickness (m) of each layer in the 3-dimensional planetary geostrophic model. . . . .	32
Table 2.2	Parameters of the 1-dimensional particle cycle model. $N$ is the level number corresponding to the depth $z$ (m). $\gamma$ , $r_1$ and $r_2$ are the rates constants for remineralization, aggregation and disaggregation respectively, all in units of $\text{yr}^{-1}$ . . . . .	33
Table 2.3	Parameters of the 3-dimensional particle cycle model. $N$ is the level number corresponding to the depth $z$ (m). $\gamma$ , $r_1$ and $r_2$ are the rates constants for remineralization, aggregation and disaggregation respectively, all in units of $\text{yr}^{-1}$ . . . . .	34
Table 3.1.	Parameter values for numerical simulations of the nitrate distribution in the North Atlantic.. . . .	52
Table 3.2.	The upper panel shows the simulated meridional nutrient transport across $24^\circ\text{N}$ and $36^\circ\text{N}$ , and the new production rate. The latter is obtained using a N:C Redfield ratio of	

	16:103, with the rate in <i>Gt yr<sup>-1</sup></i> shown in italics. Estimates from other observational and modelling studies are shown in the lower panel.. . . . .	53
Table 4.1	Parameter values for the different experiments. $\sigma_d$ is the fraction of new production used to generate dissolved nitrogen, with the remainder $(1-\sigma_d)$ being put into sinking particulate organic nitrogen. $A_v$ is the vertical diffusivity. $z'$ is e-folding depth scale of remineralization rate ( $\kappa$ ) of non-sinking and dissolved organic nitrogen (Eq. (2.14)), except in Experiment PK1, where a constant $\kappa$ is assumed.. . . . .	81
Table 4.2	The oxygen production rate as a result of new production of Experiment P5 at the mid (M) and high (H) latitude locations, in unit of $\text{mmol-O}_2 \text{ m}^{-2} \text{ day}^{-1}$ . A Redfield ratio is used to convert nitrate to oxygen production. . . . .	82
Table 4.3	The vertically integrated OUR signal of the deep ocean (600-4000 m) as a percentage fraction of that of the aphotic zone (114-4000 m), for Experiments P7, P5, P2, PK1, and PK3.. . . . .	83

## List of Figures

- Figure 1.1 Schematic of the role of photosynthesis and decomposition in carbon and nitrogen transfer in surface waters. . . . . 18
- Figure 1.2 Dissolved organic carbon (DOC) and the other major source of organic carbon in the world's ocean (data taken from Cauwet, 1978), unit is:  $10^{14}$  kg . . . . . 19
- Figure 2.1 A simple schematic diagram of the cycling of organic matter in the ocean. Organic matter is formed in the euphotic zone during photosynthetic uptake of inorganic nutrient. It is then transported below the euphotic zone by ocean circulation and particle sinking, where it is remineralized back to inorganic nutrient. The figure is adapted from Najjar (1990). . . . . 35
- Figure 2.2 A comparison of the normalized production rates of the kinetic ( $NP/R$ ) and restoring ( $NP/NP_{max}$ ) models, as a function of the dimensionless nitrate concentration ( $[NO_3]/H$ ). The restoring and kinetic models are close to

	each other when $[\text{NO}_3] < H$ .. . . . .	36
Figure 2.3	A schematic description of the particle model. Small particles ( $P_s$ ) are produced at a rate $P_r$ corresponding to primary production and exchanged with a reservoir of large particles ( $P_l$ ) by aggregation and disaggregation, with rate constants $r_1$ and $r_2$ . Large particles ( $P_l$ ) are removed from the water column by sinking, with sinking rate $S$ . Remineralization, with rate constant $\gamma$ , returns particulate material to the inorganic state. This figure is adapted from Clegg and Whitfield (1990).. . . . .	37
Figure 3.1	(a) The meridional overturning stream function ( $Sv$ ). (b) The horizontal circulation ( $\text{m s}^{-1}$ ) at a depth of 46 m. The fields of (a) and (b) are averaged over last 100 years of 2100 year integration, after an initial spin-up of 1200 years. . . . .	54
Figure 3.2	Meridional sections of the zonally averaged inorganic nitrate distribution ( $\text{mmol-N m}^{-3}$ ) for Experiments (a) E3.5, (b) P3.5, (c) P3.7. . . . .	55
Figure 3.3	The basin averaged nitrate profiles for Experiments (a) E3.5, (b) E6.5, (c) E3.6, (d) P3.5, (e) P6.5 and (f) P3.7. The solid and dashed curves are from the model and observations (Broecker and Peng, 1982) respectively. . . . .	56

- Figure 3. 4 Zonally and vertically integrated meridional nitrate transport ( $\text{kmol s}^{-1}$ ) for Experiments (a) E3.5, (b) P3.5. The dashed curves are the vertical integrated transport over the top 1000 m, while the solid curves are integrated over the depth of the ocean. . . . . 57
- Figure 3.5 Zonally and vertically integrated meridional dissolved organic nitrogen transport ( $\text{kmol s}^{-1}$ ) for Experiments (a) E3.5, (b) P3.5. The dashed curves are the vertically integrated transport over the top 1000 m, while the solid curves are integrated over the depth of the ocean. . . . . 58
- Figure 3. 6 Zonally and vertically integrated nitrate transport ( $\text{kmol s}^{-1}$ ) for Experiment P6.5 at the western ( $3^{\circ}$ - $17^{\circ}$  longitude), central ( $24^{\circ}$ - $38^{\circ}$  longitude), eastern ( $42^{\circ}$ - $56^{\circ}$  longitude) sections of the basin. The dashed curves are the vertically integrated transport over the top 1000 m, while the solid curves are integrated over the depth of the ocean. Notice the ordinate used in (a) is larger than in (b) and (c). . . . . 59
- Fig.3. 7 Vertically integrated new production in the euphotic zone (solid line), and remineralization of total organic matter including both of PON and DON in the aphotic zone (dashed line) for Experiments (a) E3.5, (b) E6.5, (c) E3.6, (d) P3.5, (e) P6.5 and (f) P3.7. The unit is  $\text{mol-C m}^{-2} \text{ yr}^{-1}$ ;

	the Redfield ratio used is N:C=16:103. The vertical dashed lines indicate the 24°-36°N latitude band. . . . .	50
Fig.3. 8	Ratio in %, of the DON remineralization to the total DON and PON remineralization in the aphotic zone for Experiments P3.5 (solid), P6.5 (asterisk) and P3.7 (dashed). The vertical dashed lines indicate the 24°-36°N latitude band. . . . .	61
Fig.3. 9	The horizontal distribution of remineralization anomaly (the negative values are in dashed line) for the Experiments (a) P6.5 and (b) P3.5. The vertical integration in aphotic zone is carried out from the base of euphotic zone to the bottom. The units is mol-C m <sup>-2</sup> yr <sup>-1</sup> . . . . .	62
Fig. 3.10	The zonally and vertically averaged horizontal advection ( $V \cdot \nabla [NO_3]$ , solid) and diffusion ( $A_h \nabla^2 [NO_3]$ , dashed) terms for Experiment P6.5. The unit is 10 <sup>-5</sup> mmol-N m <sup>-2</sup> s <sup>-1</sup> . . . . .	63
Figure 4.1	The magnitude of the thermohaline circulation (Sv) after 2000 years of model simulation of Experiment P5, for (a) February, and (b) July. . . . .	84
Figure 4.2	Meridional section of zonal averaged dissolved oxygen distribution (ml l <sup>-1</sup> ) for Experiment P5 for (a) February, and (b) July. . . . .	85
Figure 4.3	The seasonal cycle of temperature (°C) and density ( $\sigma$ unit)	

	for Experiment P5 at the mid (M) and high (H) latitude location. . . . .	86
Figure 4.4	As Figure 3, but for Experiment G5 with an increased vertical diffusivity. . . . .	87
Figure 4.5	The seasonal cycle of oxygen supersaturation ( $\text{ml l}^{-1}$ ) and percentage supersaturation (%) in the top 200 m at the mid (M) and high (H) latitude locations, for Experiment P5. . . . .	88
Figure 4.6	The seasonal cycle of the vertically and zonally averaged oxygen production ( $\text{mmol-O}_2 \text{ m}^{-2} \text{ day}^{-1}$ ) due to new production in the euphotic zone, for Experiment P5. . . . .	89
Figure 4.7	The seasonal cycle of the oxygen flux to atmosphere ( $\text{mmol-O}_2 \text{ m}^{-2} \text{ day}^{-1}$ ) at the mid (M) and high (H) latitude locations, for Experiment P5 . . . . .	90
Figure 4.8	The vertical OUR profiles ( $\text{mmol-O}_2 \text{ m}^{-3} \text{ day}^{-1}$ ) for Experiments P7 (dashed), P5, P2, PK1, and PK3 at upper layer (100-600 m) for (a) February, and (b) July. . . . .	91
Figure 5.1	The normalized flux $F/F_{100}$ and $F(z)/F_{100}$ for the exponential formulation of Eq. (5.10) with sinking rates $S=100$ (solid), 200 (asterisk), 300 (circle) $\text{m day}^{-1}$ . The dashed line is from Martin et al. 's (1987) power law formulation, Eq. (5.11). . . . .	111
Figure 5.2	Vertical profile of primary production with primary	

- production rates ( $P_0$ ) of 103 g-C m<sup>-2</sup> yr<sup>-1</sup> of Clegg and Whitfield (1990) (solid), 130 g-C m<sup>-2</sup> yr<sup>-1</sup> of Martin et al. (1987) (dashed), and 245 g-C m<sup>-2</sup> yr<sup>-1</sup> of Knauer and Martin (1981) (asterisk). The open circles (o) represent the primary production used in Clegg and Whitfield's (1990) particle cycling model. . . . . 112
- Figure 5.3** The simulated particulate organic carbon sinking flux using the remineralization rates of Table 2.2 (solid), and half (dashed) and double (asterisk) that rate. The observational data (o) are from Knauer and Martin (1981). The unit are g-C m<sup>-2</sup> yr<sup>-1</sup>. . . . . 113
- Figure 5.4** The simulated large particle organic carbon flux ( $F_l$ ) using different primary production rates ( $P_0$ ): (a) 103 g-C m<sup>-2</sup> yr<sup>-1</sup> of Clegg and Whitfield (1990); (b) 130 g-C m<sup>-2</sup> yr<sup>-1</sup> of Martin et al. (1987). The solid curves are the simulated flux, while the dashed curves are the fluxes calculated by Clegg and Whitfield (their Table A1) in (a), and Martin et al. (their Figure 5) in (b). . . . . 114
- Figure 5.5** (a) The simulated total organic carbon concentration ( $P_s+P_l$ ) (solid), and the Clegg and Whitfield's (1990; their Figure 8) estimate (dashed). (b) The percentage of mass ratio  $P_l/P_s$  simulated by the model. The maximum value of 6.2% is

- reached in the upper 20 m. A primary production rate of  $103 \text{ g-C m}^{-2} \text{ yr}^{-1}$  from Clegg and Whitfield (1990) is assumed. . . . . 115
- Figure 5.6 (a) The simulated aggregation ( $r_1 P_s$ ; solid) and disaggregation ( $r_2 P_i$ ; asterisk) rates at steady state. (b) The simulated particulate organic carbon concentration ( $P_s + P_i$ ) using the aggregation and disaggregation rates of Table 2.2 (solid), and an increase of these rates by a factor of 5 below 600 m, keeping their ratio constant (asterisk). The primary production rate used is  $103 \text{ g-C m}^{-2} \text{ yr}^{-1}$ , as in Figure 5.5. . . . . 116
- Figure 5.7 The simulated zonally averaged distribution of (a) large particle flux ( $F_D$ ); and (b) suspended particulate organic carbon concentration ( $P_s$ ). . . . . 117
- Figure 5.8 The horizontal distribution of (a) the large particle flux ( $F_D$ ), and (b) the concentration of suspended organic carbon particles ( $P_s$ ); at a depth of 114 m, the bottom of the euphotic zone. . . . . 118
- Figure 5.9 The domain averaged vertical profile of (a) total organic carbon concentration ( $P_s + P_i$ ), and (b) large particle flux ( $F_D$ ), simulated by the 3-dimensional model. Results from Clegg and Whitfield's (1990; their Figure 8 and Table A1) 1-dimensional model are shown by the open circles. . . . . 119

## Abstract

We have coupled a 3-dimensional physical planetary geostrophic ocean general circulation model to different biological models to investigate the interaction between physical and biological processes. A 1-dimensional particle cycle model with two particle size classes has been developed and coupled to the physical model as well.

The ocean model (Zhang et al., 1992) is based on the planetary geostrophic equations in spherical coordinates. The model equations include the full prognostic temperature and salinity equations. The momentum equations are diagnostic and include geostrophic balance, and a linear friction term in order to provide a western boundary current. The wind stress is applied at the top level of the model. The temperature and salinity distributions used in the surface boundary restoring condition are taken from climatological data. The model domain consists of a flat-bottomed box of  $60^\circ$  longitude extending between  $5^\circ\text{N}$  and  $65^\circ\text{N}$ . The horizontal resolution is  $2.3^\circ$  in both latitude and longitude with 14 levels in the vertical.

The physical model is first coupled to a biological model where new production is given by a restoring condition of surface nitrate towards its observed concentration. The coupled model is used to examine Martin et al.'s (1987) hypothesis that lateral

transport and decomposition of slow or non-sinking organic matter can cause a non-local balance between the remineralization rate and the overlying new production rate in open ocean regions. The role of the Gulf Stream in nutrient transport is examined. The model results agree well with the North Atlantic nutrient transport calculated from observed nutrients and hydrographic data. The model results suggest that the thermohaline overturning circulation and the Gulf Stream horizontal recirculation play an important role in the North Atlantic nutrient distribution.

The physical model is then tested in the seasonal mode, and coupled with a biological model which is based on nitrate limiting the rate of new production. The model simulated seasonal oxygen cycle agrees well with the results of observational studies and 1-dimensional model simulations. The oxygen utilization rate below the euphotic zone provides a useful estimate of new production.

A 1-dimensional time dependent particle cycling model with two particle size classes based on Clegg and Whitfield (1990) is then developed. The simulated total organic carbon concentration and large particle flux are consistent with observations and other 1-dimensional model simulations. The downward transport of organic carbon is mainly accomplished by the fast sinking large particles, which comprise a small fraction of the total particulate mass. The steady state version of the particle model is also coupled with the 3-dimensional physical model. The magnitudes of simulated organic carbon flux and total organic matter concentration are comparable with observations.

## Résumé

Nous avons utilisé un modèle tridimensionnel planétaire géostrophique (PG) de circulation générale océanique et des modèles biologiques pour étudier les interactions entre les processus physiques et biologiques. Un modèle unidimensionnel de cycle de particules a été créé et appliqué avec succès aux conditions océaniques.

Le modèle océanique (Zhang et al., 1992) est basé sur les équations planétaires géostrophiques en coordonnées sphériques. Le modèle se compose des équations pronostiques de température et de salinité. Les équations du mouvement sont diagnostiques et incluent l'équilibre géostrophique ainsi qu'un terme de friction linéaire afin de créer un "western boundary current". La tension du vent est appliquée au niveau supérieur du modèle. Les conditions de rappel de température et de salinité proviennent des données climatiques. Le domaine du modèle se compose de 60° de boîte carrée latitude-longitude à fond plat et s'étend de 5°N à 65°N. Le modèle a 14 niveaux et une résolution de 2.3° en latitude et en longitude.

Un modèle couplé physique-biologique a été employé pour vérifier l'hypothèse de Martin et al. (1987) à l'effet que le transport latéral et la décomposition de matière organique en précipitation lente ou en suspension produisent un équilibre non-local entre

le taux de reminéralisation et celui de production nouvelle dans les couches supérieures de certaines régions océaniques. Le rôle du Gulf Stream dans le transport de nutriments a aussi été étudié. Les résultats suggèrent que la circulation thermohaline méridionale et la recirculation horizontale du Gulf Stream jouent des rôles très importants dans la distribution de nutriments dans l'Atlantique du Nord.

Le modèle tridimensionnel planétaire géostrophique a été testé en mode saisonnier et puis couplé à un modèle biologique basé sur le nitrate limitant le taux de production nouvelle. Le cycle saisonnier d'oxygène simulé par le modèle couplé est en bon accord avec les observations et les simulations du modèle à une dimension. Les résultats du modèle suggèrent que le taux d'utilisation d'oxygène (OUR) sous la zone euphotique donne un bon estimé de la production nouvelle.

Un modèle unidimensionnel non-stationnaire de cycle de particules basé sur le modèle de Clegg and Whitfield (1990) a été créé pour deux classes de tailles de particule. Ce modèle a simulé des concentrations de particules de carbone organique et des flux de particules réalistes. Ces simulations s'accordent aussi bien avec les observations qu'avec les résultats d'autres modèles à une dimension. Les résultats du modèle démontrent que le transport vers le bas de carbone organique est produit principalement par la précipitation rapide de grandes particules dont la masse a un rapport faible à la masse totale des particules. Le mode stationnaire de ce modèle de particules a été couplé au modèle tridimensionnel planétaire géostrophique de l'Atlantique du Nord. Ce modèle couplé a simulé des flux de carbone organique et des concentrations de particules organiques qui se comparent bien aux observations.

## List of Symbols

$x, y, z$ : eastward, northward, upward Cartesian coordinates

$u$ :  $x$  component of velocity, positive eastward,

$v$ :  $y$  component of velocity, positive northward

$w$ :  $z$  component of velocity, positive upward

$z_e$ : depth of euphotic zone

$z^*$ : remineralization depth scale

$z'$ : depth constant for remineralization rate

$t$ : time

$\rho$ : density

$p$ : pressure

$Q$ : tracer field including temperature ( $T$  in  $^{\circ}\text{C}$ ), salinity ( $S$  in parts per thousand) and chemical tracer.

$F_s$ : surface forcing for tracer field

$K_w$ : piston velocity

$S_c$ : Schmit number

$A_h$ : horizontal diffusivity in 3-dimensional ocean circulation model

$A_v$ : vertical diffusivity in 3-dimensional ocean circulation model

$K_{vs}$ : vertical diffusivity in 1-dimensional particle model

$\tau$  : restoring time for surface nutrient in restoring model

$\sigma_d$ : non-sinking and dissolved fraction of new production

$\kappa$  : remineralization constant for dissolved organic matter

$H$  : adjusted constant in kinetic model

$R$  : maximum growth rate of new production in kinetic model

$R_{N:O_2}$ : Redfield ratio of N:-O<sub>2</sub>

$R_{N:C}$ : Redfield ratio of N:C

$\gamma$  : remineralization rate constant for fine and large particles in 1-dimensional particle model

$r_1$ : aggregation rate constant

$r_2$ : disaggregation rate constant

$S$  : sinking rate of large particle

$P_f$ : concentration of fine particle

$P_l$ : concentration of large particle

$F_l$  : sinking flux of large particle

$F_e$ : sinking flux of large particle at bottom of euphotic zone

$P_p$ : primary production rate in 1-dimensional particle model

$CON$ : convective adjustment

$[NO_3]$ : model nitrate concentration in model

$[\text{NO}_3]^o$ : observed nitrate concentration of observation

$[\text{O}_2]$ : model oxygen concentration in model

$[\text{O}_2]^a$ : atmospheric oxygen concentration

## List of Abbreviations

PG: planetary geostrophic

NP: new production

RP: regenerated production

PP: primary production

HTCO: high temperature catalytic oxidation

DOM: dissolved organic matter

DOC: dissolved organic carbon

DON: dissolved organic nitrogen

POM: particulate organic matter

PON: particulate organic nitrogen

POC: particulate organic carbon

## Acknowledgments

I wish to express my sincere gratitude to my thesis advisor, Dr. Charles A. Lin, whose dedicated guidance and supervision made it possible for this research to be accomplished.

I am also grateful to my thesis co-supervisor, Dr. Kenneth L. Denman for his help and guidance during the research work. I am especially thankful for the opportunity to work at the Institute of Ocean Sciences during the summer of 1994.

Drs. J. L. Sarmiento and W. J. Jerkins provided many suggestions in the nutrient cycling study. Dr. R. Najjar answered many questions, and Dr. N. Price was helpful during the course of this study.

I would also like to thank Drs. G. Ingram, D. Straub, L. Mysak, S. Zhang, W. M. Xu, J. Sheng, P. Chen, D. L. Zhang, A. Weaver, J. P. Gan, H. Lin, Mr. Ning Bao, Mr. Chun-qian Li, Mr. Liang Ma and Mr. Jin-Hui Huang for interesting and informative discussions. Mr. A. Schwartz provided excellent technical assistance in computing. Mr. M. Klasa translated the abstract to French.

I thank members of the Department of Atmospheric and Oceanic Science, and the Centre for Climate and Global Change Research (C<sup>2</sup>GCR), who helped me in many ways during my graduate studies. Thanks also go out to my friends at McGill, who made me

feel loved away from home.

My grandmother and parents supported me during my period of study. I wish to express my appreciation for their constant source of attention, concern and love by dedicating this thesis to them. I also wish to thank my brothers and my wife for their love and care.

Funding for this work was provided by the National Sciences and Engineering Research Council (NSERC) through the Canadian JGOFS (Joint Global Ocean Flux Study) program and research grants to Dr. C. A. Lin.

# Statement of Originality

## Nitrate Cycle Simulation

- Compare the restoring and kinetic model formulations used in the parameterization of new production.
- Test the hypothesis (Martin et al., 1987) that lateral transport and decomposition of slow and non-sinking organic matter can cause a non-local balance between remineralization rate and the overlying new production rate in the open ocean. Model results show more than 50% of the remineralization is due to the remineralization of dissolved and non-sinking organic matter.
- The Gulf Stream horizontal recirculation flow plays an important role in the nitrate transport in the North Atlantic Ocean. This flow accounts for a significant fraction of the transport of dissolved and non-sinking organic matter from high to mid-latitudes. The oxidation of non-sinking organic matter during its transit in the subtropical gyre can result in large oxygen utilization rate (A research paper based on this work has been submitted to the journal *Global Biogeochemical Cycles*).

## **Oxygen Seasonal Cycle Simulation**

- Test the planetary geostrophic physical model in the seasonal mode. The resulting seasonal variation of temperature and density fields drives the oxygen seasonal cycle.
- Simulate the seasonal cycle of oxygen in the North Atlantic. New production is shown to be important in maintaining the oxygen super-saturation in the surface layer.

## **Particle Cycle Modelling**

- Examine the 1-dimensional particle cycling model of Clegg and Whitfield (1990) analytically for the steady state version, and numerically for the time dependent version.
- Couple the steady state 1-dimensional particle model with the annual mean planetary geostrophic physical model. The magnitude of simulated large particle flux and total organic carbon particle concentration are consistent with observations.

# Chapter 1

## Introduction

### 1.1 An overview

Carbon dioxide (CO<sub>2</sub>) is the principal greenhouse gas of the atmosphere. Carbon is cycled continually between the atmosphere, terrestrial biosphere and the oceans. To understand the global carbon cycle, we need an improved knowledge of the ocean carbon cycle, ocean surface layer productivity, and the removal of biogenic matter to the sea-bed. This is because the carbon entering the ocean from the atmosphere undergoes complex biological and chemical cycling. As the ocean holds about 60 times more carbon than the atmosphere, small changes in carbon biogeochemistry can produce a marked change in the atmospheric carbon reservoir. Evidence for this link between atmospheric CO<sub>2</sub> and ocean carbon chemistry can be found, for example, in the  $\Delta^{13}\text{C}$  record of deep-sea foraminifera (Berger et al., 1989).

Ocean biogenic cycles play an important role in the natural carbon cycle. In the surface waters, photosynthesis converts aqueous  $\text{CO}_2$  into organic compounds. A fraction of the biogenic material sinks or is transported out of the surface layers into deeper layers where it is decomposed and oxidized back to  $\text{CO}_2$ . This combination of processes, referred to as the "biological pump" (Longhurst and Harrison, 1989), would continually strip  $\text{CO}_2$  from the surface ocean and sequester it in the deeper ocean. Two other relevant biological processes are the "solubility" and "carbonate" pumps. The solubility of  $\text{CO}_2$  increases with decreasing temperature. The solubility pump (Volk and Hoffert, 1985) thus refers to increased absorption of  $\text{CO}_2$  from the atmosphere as warm tropical water travels poleward at the surface ocean. Due to surface cooling, its density can become sufficiently large to cause sinking, thus creating a vertical gradient in  $\text{CO}_2$ . The carbonate pump refers to the downward transport of carbon accomplished through the sinking of calcareous shells and tests. The formation of this material, which is mostly calcium carbonate ( $\text{CaCO}_3$ ) removes carbon from the surface ocean. The biological pump, in conjunction with the solubility and carbonate pumps, maintain the vertical gradient of dissolved inorganic carbon. Although there have been field programs to measure the productivity and downward flux of carbon, available observational data are still very limited due to the difficulty of obtaining such observations in the open ocean. Coupled biological-physical numerical models are thus needed to better understand biological processes at work in the oceanic carbon cycle.

## 1.2 New production and downward transport of organic matter

A key element in studying the ocean carbon cycle is to determine the amount of new production and the associated transport of organic carbon and nutrients (e.g. Jahnke, 1990). Eppley and Peterson (1979) divided the primary production into two categories based on the source of the fixed nitrogen utilized (Figure 1.1). The portion of the primary production supported by nitrogen supplied by the decomposition of organic matter within the euphotic zone is termed "regenerated production". Ammonium ( $\text{NH}_4^+$ ) is the dominant form of the nitrogen supplied through such decomposition (Dugdale and Goering, 1967). On the other hand, new production is that portion of photosynthesis which depends on inorganic nitrate supplied from outside the euphotic zone, mainly from below the euphotic zone. The nitrogen fixed is primarily in the form of nitrate ( $\text{NO}_3^-$ ). At steady state, it is important to distinguish between new production and regenerated production. Regenerated production represents a cycling of fixed nitrogen only within the euphotic zone. It is therefore not limited by the abundance of fixed nitrogen, but simply by the speed at which nitrogen is cycled between producers and decomposers. New production (NP), on the other hand, is supported by the input of nitrogen from outside the euphotic zone. If the nitrogen content of the euphotic zone is not changing, this input must then be balanced by an export of organic nitrogen from the euphotic zone. Thus while the rate of regenerated production depends on factors solely within the euphotic zone, new production is controlled by nutrient input rates to the euphotic zone and equals the organic nitrogen export rate.

Martin (1990) hypothesized that new production is also limited by availability of iron, and the increased new production by iron fertilization may reduce the future rate of increase of atmospheric carbon dioxide concentration. This hypothesis has been examined through simulations with box models (Joos et al., 1990a,b; Peng and Broecker, 1991a,b) and 3-dimensional ocean general circulation models (Sarmiento and Orr, 1991; Kurz and Maier-Reimer, 1993), and also tested by experiments in the equatorial Pacific (Martin et al., 1994; Watson et al., 1994; Kolber et al., 1994). The results suggest that the addition of iron has an easily measurable effect on the marine ecosystem in short term, but after a brief disequilibrium, the ecosystem responds by recycling carbon rapidly back to inorganic form, with a small overall effect on atmospheric carbon dioxide levels.

New production can be estimated by measurements of  $\text{NO}_3^-$  utilization rate. Analysis of N:C ratio shows that this ratio varies in exported organic matters, indicating that remineralization processes have occurred. For this reason, it has been suggested that the portion of primary production that results in a flux of organic carbon away from the euphotic zone be designated as "export production" (Murray et al., 1989).

The concept of new production has provided a very useful framework to assess the relationships among primary production, hydrodynamic conditions controlling nutrient inputs, and the transport of organic carbon from the euphotic zone. The ratio of new production to total primary production, the "f-ratio", tends to be lowest in the central oceanic gyres where the supply of new nutrients is minimal, and highest in the coastal ocean where mixing with deeper water is vigorous. Eppley and Peterson (1979) observed that typical f-ratio values are 6% in oligotrophic waters, 13% in transition waters between

subtropical and subpolar zones, 18% in area of equatorial upwelling and the subpolar ocean, 30% in inshore waters.

Primary production takes the form of particulate organic matter and dissolved organic matter. Particulate organic matter includes both living and non-living particles in the sea larger than  $1\mu\text{m}$ , most of which is of biological origin in the surface waters (e.g., Silver and Gowing, 1991). They can be subdivided according to size. The smallest particles of up to a few tens of  $\mu\text{m}$  comprise bacteria, algal cells, and other fine organic detritus. The range between a tens to a few hundred  $\mu\text{m}$  represents large detritus, fecal pellets, and products of biological aggregation or packaging (McGave, 1984; Johnson and Kepkay, 1992). In contrast to particulate matter, dissolved organic matter includes colloidal as well as purely dissolved material, and is operationally defined as all organic matter passing through a filter with a nominal pore size in the order of  $0.5\mu\text{m}$  (e.g., Wakeham and Canuel, 1988). The majority of particles in suspension of size less than  $5\mu\text{m}$  consists of free-living bacteria, subsisting mainly on dissolved organic matter compounds. The latter include organic acids, vitamins and sugars, which are produced mainly as metabolic byproducts of phytoplanktons (O'Melia, 1987; O'Melia and Tiller, 1993).

The division of organic matter into broad categories is important because the different categories reflect distinct processes. The average sinking rate of large particulate organic matter is  $100\text{ m day}^{-1}$  (Bacon et al., 1985); it is generally unaffected by ocean current, unlike suspended and dissolved organic matter. These large particles sinking out of the euphotic zone are degraded directly below where they are produced, thus providing

a coupling between organisms inhabiting the euphotic zone and those at depth. Empirical relationships have been proposed to represent the organic carbon flux in the water column below the base of the euphotic zone as depending on the mean net primary production rate at the surface and a depth-dependent consumption function (Suess, 1980; Betzer et al., 1984).

The most frequently measured flux of organic matter is that of sinking particles. Fluxes of suspended and dissolved organic matter are difficult to estimate. Until recently, it was generally thought that new production is transported almost entirely by vertically sinking particulate organic carbon (POC). However, measurements of dissolved organic carbon (DOC) using a new analytical technique (Sugimura and Suzuki, 1988) have revealed an active dissolved organic carbon pool that is several times larger than is indicated by previous measurements. The new technique is based on high temperature catalytic oxidation (HTCO). It was believed to recover 200 to 400% more dissolved organic carbon than previous methods, such as photo-oxidation. Such high dissolved organic carbon values imply that there is an undiscovered pool of DOC in the ocean, which would be important for estimates of ocean carbon fluxes (e.g., Toggweiler, 1988, 1989; Jackson, 1988). However, there has since been a steady downward revision of DOC pool size. HTCO now appears to recover an absolute maximum of 10-40% more dissolved organic carbon than photo-oxidation (Chen and Wangersky, 1993; Ridal and Moore, 1993). The magnitude of the marine DOC pool is thus still an open question. It appears that earlier estimates (e.g. Cauwet, 1978) of dissolved organic carbon in the world's ocean (Figure 1.2) are probably not far off from values obtained using newer

methods (Sharp, 1993; Sharp et al., 1994). In any case, DOC is still more abundant than any other marine source of organic carbon by at least a factor of 10 (Druffel et al., 1992).

Carlson et al. (1994) found significant changes in DOC concentrations occur over short temporal and spatial scales. They have termed a portion of DOC as "semi-labile", along with the traditional "refractory" and "very labile" portions. The refractory pool has turnover times on the same order as ocean mixing (several hundred years), while the very labile pool has turnover times of order hours to a day. The semi-labile pool would have turnover times of many months to a few years. This pool is important in determining the vertical and horizontal carbon fluxes away from the areas of production. In the Sargasso Sea, Carlson et al. (1994) found DOC advected downwards out of the euphotic zone via deep winter mixing to be greater than the particulate organic carbon captured by sediment traps at a depth of 150 m. Along the equatorial Pacific, Murray et al. (1994) concluded that nearly 60 to 90% of new production is transport from the equatorial region by ocean current, most likely in the form of DOC. Altabet (1989) computed the suspended particulate organic matter flux at 100 m in Sargasso Sea from the product of the vertical diffusivity and the suspended particulate organic nitrogen gradient. In the annual mean, the results showed that the particulate organic nitrogen flux is 40% of the total nitrogen flux.

We now turn to modelling studies. Toggweiler (1989) and Siegenthaler and Sarmiento (1993) found that model simulations were close to observations if the vertical transport of both DOC and POC were included, instead of POC alone. Najjar (1990) and Najjar et al. (1992) used a phosphorus-based nutrient model coupled to a general

circulation model to evaluate the relative roles of dissolved and sinking particulate phases in the downward transport of organic matter. In the case of sinking particles dominating the downward transport and remineralizing according to a formulation based on sediment trap observations, the simulated particle fluxes and thermocline nutrient concentrations are higher than observed in equatorial upwelling regions. This is due to a positive feedback whereby upwelling leads to enhanced new production, enhanced remineralization and nutrient concentration in the upwelling waters, which increases further new production. The anomalous high nutrient concentration cannot be eliminated by using a different particle flux remineralization depth. In the case of dissolved organic matter dominating the downward transport, the anomalously high nutrient concentration in both upwelling and convective regions is completely eliminated, suggesting that dissolved organic material production may be significant in the euphotic zone in this region.

Bacastow and Maier-Reimer (1991) used a general circulation model to simulate the phosphate distribution. They performed experiments where new production is transported mainly by either falling particulate organic carbon, or by dissolved organic carbon. The simulated phosphate field agrees significantly better with the observations in the latter case.

The importance of the dissolved and suspended phases in the downward transport of organic matter is also suggested by nitrate budget calculations. Rintoul and Wunsch (1989) computed the nitrate fluxes across  $24^{\circ}\text{N}$  and  $36^{\circ}\text{N}$  in the Atlantic ocean using hydrographic data, and measurements of silicate and nitrate. They inferred the velocity field using the thermal wind relation and imposed constraints in the flux of mass and

silicate across these sections. If all of the nitrogen taken up within the euphotic zone is remineralized directly below, as would be the case if new production was in the form of large sinking particles, then the nitrate flux across these latitudes should be zero. This assumes that the available single summer measurements are representative of the annual mean, and the nitrate input from rivers and the Arctic ocean is negligible. However, Rintoul and Wunsch found a significant northward flux of nitrate of  $119 \pm 35 \text{ kmol s}^{-1}$  at  $36^{\circ}\text{N}$ . This must be balanced by a southward flux of organic nitrogen in suspended and dissolved form. Martin et al. (1987) suggested that oxidation of slowly sinking or non-sinking particles carried around the subtropical gyre would lead to nitrate regeneration. Following Martin et al's (1987) arguments, Rintoul and Wunsch (1989) hypothesized that the Gulf Stream recirculation gyre contributes to a southward flux of organic nitrogen.

The role of the Gulf Stream gyre in the North Atlantic ocean nitrate cycle is still uncertain. A modelling study will enhance our understanding of nutrient cycling in the North Atlantic ocean, including the relative importance of the dissolved and suspended organic matter in the nitrate transport.

### **1.3 Seasonal cycle of oxygen**

The distribution of oxygen ( $\text{O}_2$ ) in the water column can be used to assess organic carbon export out of euphotic zone in two ways. Oxygen is produced as a byproduct of photosynthesis and is consumed during respiration (Figure 1.1). Thus in a water mass where production and respiration occur in equal amounts, there is no net change in the

oxygen content. However, primary production that results in a flux of organic matter from the euphotic zone yields a net production of oxygen within the euphotic zone, and a net consumption of oxygen in the underlying thermocline waters. It is at the latter location where the majority of the exported material is respired. Thus the organic carbon export from the euphotic zone can be estimated either by using the oxygen production rate in the euphotic zone, or the oxygen consumption rate in the thermocline.

There have been recent studies which examine different aspects of metabolic processes in the surface waters. Upper ocean particle trapping has an uncertain efficiency and is biased toward transport by large particles (McCave, 1975; Honjo, 1982). The mass balance oxygen method does not suffer from this difficulty; it has been used to calculate net biological oxygen production in the euphotic zone (Shulenberger and Reid, 1981). The mass balance approach has led to a continuing reassessment of the mechanisms of nutrient recycling in the upper ocean and the level of global productivity (e.g., Platt and Harrison, 1985; Jenkins, 1988).

Physical processes such as radiation heating and air injection may produce oxygen supersaturation which is unrelated to biological activity. On the other hand, much of the biogenic oxygen may be lost from the seasonal thermocline via vertical mixing with deep waters and gas exchange with the atmosphere. Measurements of dissolved argon can quantify these effects; argon is an inert gas whose physical properties (e.g. solubility and diffusivity) are close to those of oxygen with a similar temperature dependence (Benson, 1965). Craig and Hayward (1987) compared oxygen and argon supersaturation at two stations in the subtropical North Pacific; argon was found to be much less supersaturated

than oxygen, suggesting that most of the oxygen supersaturation was photosynthetically produced. Spitzer and Jenkins (1989) used the 1-dimensional model of Price et al. (1986) to study the seasonal cycle near Bermuda. They found that the argon supersaturation is 3-4 times smaller than that of oxygen, and only a small fraction of the subsurface oxygen supersaturation maximum can be attributed to physical causes. Thus the oxygen supersaturation must be mainly due to photosynthetic production. This is similar to the observational results of Craig and Hayward (1987). Furthermore, most of the oxygen produced by biological processes is subsequently lost to vertical mixing and gas exchange.

Emerson (1987) interpreted Ocean Weather Station P oxygen data from 1969 to 1979, using a simple quasi-steady state model of mixed layer heating, gas exchange, and net biological oxygen production. Oxygen production and net carbon export are assumed to be stoichiometrically related, giving a carbon flux of 100-300 mg-C m<sup>-2</sup> day<sup>-1</sup>. Emerson et al. (1991) reported that mass balance requires a net carbon production in the euphotic zone of ±140 mg C m<sup>-2</sup> day<sup>-1</sup>. The net rate of biological oxygen production in the subarctic Pacific inferred using an upper ocean mass balance of the major atmospheric gases (O<sub>2</sub>, Ar, N<sub>2</sub>) (Emerson et al., 1993) and oxygen isotopes δ<sup>18</sup>O<sub>2</sub> (Quay et al., 1993) are consistent with earlier estimates of Emerson (1987) and Emerson et al. (1991).

The 1-dimensional modelling studies have also been carried out to investigate the evolution of oxygen supersaturation in the surface layers (e.g. Jenkins; 1988, Archer et al., 1993). Thomas et al. (1990) used a one-dimensional integral mixed layer model (Gaspar, 1988) to examine the temporal evolution of monthly averaged dissolved oxygen content of surface waters at Station P. They found that gas exchange, biological

production and entrainment of sub-mixed layer water all contribute approximately equally to the oxygen supersaturation during warming periods and to the under-saturation during cooling periods. In a later study, Thomas et al. (1993) used another upper ocean model, the eddy kinetic energy model of Gaspar et al. (1990), to examine the Station P oxygen mixed layer concentration. The eddy kinetic model simulates better both the seasonal and short time evolution of the oxygen concentration, compared to the integral mixed layer model.

The oxygen evolution in the surface layer is determined by both biological and physical processes, and their relative roles are still uncertain. A 3-dimensional modelling approach will improve our understanding of the interaction of biological and physical processes, and the surface ocean productivity.

#### **1.4 Particle cycling**

Most of the suspended matter in the ocean exists as aggregates, made up of organic detritus, inorganic particles, and microorganisms (Riley, 1963). Although large particles are less abundant than fine suspended particulate (McCave, 1984), the downward transport of mass flux is mainly carried out by these large fast sinking particles (McCave, 1975; Honjo et al., 1984; Asper, 1987). The existence of large marine-snow-sized particles has been demonstrated for the open ocean (e.g. Trent et al, 1978; Alldredge, 1979; Silver and Alldredge, 1981), and coastal and estuarine environments of high turbidity (Eisma et al., 1983; Well and Shanks, 1987). Mass aggregation of diatoms has also been observed

during phytoplankton blooms (Smetacek, 1985; Kranck and Milligan, 1988; Riebesell, 1989, 1991a, b). These studies show that during the early phase of the bloom, detrital aggregates are dominant. Diatom-dominated algal flocs are found around the peak of the bloom, while aggregates containing both algal and detrital components dominate the post-bloom interval.

Fowler and Knauer (1986) and Lee and Wakeham (1988) reviewed the large, rapidly sinking particulate material collected by sediment trap experiments. The smaller aggregates can coalesce on a large scale to produce the macroaggregates known as "marine snow" (Alldredge and Hartwig, 1986). Sinking large particles consist mainly of marine snow, zooplankton fecal pellets and intact organisms, with the most abundant component being marine snow particles. The latter are amorphous, heterogeneous aggregates with size larger than 500  $\mu\text{m}$  and are composed of detrital material, living organism and inorganic matter (Alldredge and Silver, 1988, Alldredge and Gottschalk, 1989). Sinking particles which consist of both fecal pellets and marine snow aggregates are rare, but their fast settling rates lead to short turnover times. These particles are responsible for the most of the vertical transport of material from the ocean to the sea floor (Alldredge and Gottschalk, 1988; Silver and Gowing, 1991).

Fine material suspended in water constitutes most of the standing stock of particulate matter in the ocean. The spectrum of particle sizes in the water column is sustained in approximate steady state by a continuous exchange between larger sinking particles and smaller suspended non-sinking particles, through aggregation and disintegration (e.g. Farley and Morel, 1986; Johnson and Kepkay, 1992). Suspended

matter and colloid aggregation have been identified as an important mechanism for transferring suspended colloid organic matter up the particle size spectrum to form microaggregates (Honeyman and Santschi, 1989; Santschi and Honeyman, 1991a,b). The aggregation process moves colloids up the size spectrum, producing aggregates of size from tens of  $\mu\text{m}$  to mm scales.

The formation of large particles and marine snow is controlled by both biological and physical processes. McCave (1984) examined four major mechanisms which can bring particles together: Brownian motion, fluid shear, differential settlement, and animal feeding. He concluded that animal feeding must be the dominant mode by which particles are aggregated into sizes which are large enough to contribute to material fluxes. Of the physical mechanisms, smaller colloids are transported to bacterial cells by Brownian motion. This multi-directional transport of particles on a small scale is a major factor contributing to fine particle collisions (O'Melia, 1987, O'Melia and Tiller, 1993). Differential settlement dominates coagulation between similarly sized particles of size between 1 and 100  $\mu\text{m}$ . The collision of small particles with larger ones, resulting in the formation of marine-snow-sized aggregate, is mainly controlled by shear. Jackson (1990), assuming a constant cell stickiness, proposed that physical processes alone could determine the time and extent of algal aggregation. Based on a physical coagulation model, he showed that the rate of aggregation depends strongly on algal concentration. Above a critical maximum concentration, physical aggregation would become the dominant factor leading to a rapid flocculation of a large portion of the algal biomass.

The sinking of particulate organic matter and detritus can cause a progressive

downward movement of nutrient out of the photic zone. Wakeham and Canuel (1988) found that the suspended pool, characterized by very long residence times from years to decades, consists of labile organic compounds. Slow sinking or advection and diffusion of suspended and dissolved material from the surface cannot be a significant source of suspended material at depth, as the long transit time would lead to extensive material degradation. The disaggregation of fecal pellet is an unlikely source, as the organic matter contained in these pellet indicates high degradation. Wakeham and Canuel suggested that the suspended pool at depth is a result of the disaggregation of fast-sinking marine snow particles which contains fresh, labile organic material from the surface. This pool of labile organic matter is difficult to reconcile with the conventional notion that suspended particulate matter is more refractory than sinking particulate matter (e.g. Altabet, 1988). This difficulty needs to be resolved to better understand the interaction between suspended and large sinking particles.

Small particles less than approximately 10  $\mu\text{m}$  are thought to constitute the bulk of total particulate mass and surface area in the water column, and trace metals are assumed to be absorbed onto this fraction only. The scavenging process refers to the process where large particles capture smaller ones and sink, and the elements absorbed onto the surface of fine particles are then removed from the water column (Coale and Bruland, 1987; Buesseler et al., 1990). For metals that bind strongly to particle surfaces with no biological function, absorption and scavenging are passive processes, as they act merely as an agent of transport. The dominant removal process is provided by the partitioning into marine particulate material which subsequently sinks, thus leading to a

transport of the metals to greater depths (Fowler and Knauer, 1986).

Thorium isotopes have a high reactivity with suspended particles and are readily scavenged from the water column (Krishnaswami et al., 1976). Observations suggest that in the productive surface layers, thorium and the other radioisotopes are rapidly removed by biological process (Coale and Bruland, 1985; Bacon and Anderson, 1982). Insight on thorium behaviour was also obtained from the sediment trap studies of Anderson et al. (1983) in the Atlantic and Pacific. Examination of radioisotope ratios suggest that in the open ocean, rapidly sinking particles deliver most of the dissolved  $^{230}\text{Th}$  to the sediments.

The scavenging process for thorium has been characterized as a reversible absorption onto small non-sinking particles that constitute the bulk of the standing stock in the water column (Bacon, 1988; Moore and Hunter, 1985). Buesseler et al. (1992) measured a series of four dissolved and particulate  $^{234}\text{Th}$  profiles over a 36-day period at  $47^{\circ}\text{N}$ ,  $20^{\circ}\text{W}$  as a part of the JGOFS North Atlantic Bloom Experiment. The results show that during the bloom period, when both particle and  $^{234}\text{Th}$  concentrations were changing rapidly, the ocean mixing effect needed to be taken into account. Simple models which have been applied to these data (e.g. Nozaki et al., 1987) often incorporate particles cycling dynamics in addition to the reversible absorption that characterizes the uptake of scavenged metals. Clegg and Whitfield (1990) developed a steady state particle cycling model. This model has been successfully applied to simulate the particle standing stock (Clegg and Whitfield, 1990) and the thorium vertical distribution in the open ocean (Clegg and Whitfield, 1991).

It is difficult to directly observe the interaction between small particle and large

sinking particle pools in the ocean. It is thus of great interest to conduct a modelling study to investigate particle cycling.

## **1.5 Organization of the Thesis**

In this thesis, we couple a biological model to a 3-dimensional physical planetary geostrophic ocean circulation model with idealized geometry to examine nutrient cycling in the North Atlantic. The coupled model is used to evaluate the role of the Gulf Stream recirculation gyre in the North Atlantic nitrate cycle. The seasonal oxygen cycle in the upper surface layer is also simulated using the coupled model. A 1-dimensional time dependent particle model is developed and coupled to the 3-dimensional model to simulate particle sinking fluxes and standing stock. These nutrient cycling studies contribute to the understanding of the interaction of biological and physical processes in the ocean, and the role of this interaction in the oceanic carbon cycle.

Chapter 2 describes the formulation of the physical and biological models. Chapter 3 investigates the role of the Gulf Stream gyre in the transport of nitrate and non-sinking organic matter in the North Atlantic. In Chapter 4, we describe simulations of the seasonal cycle of oxygen in the upper surface waters. Chapter 5 examines the simulated particulate organic carbon flux and fine particle standing stock. The conclusions are presented in Chapter 6.

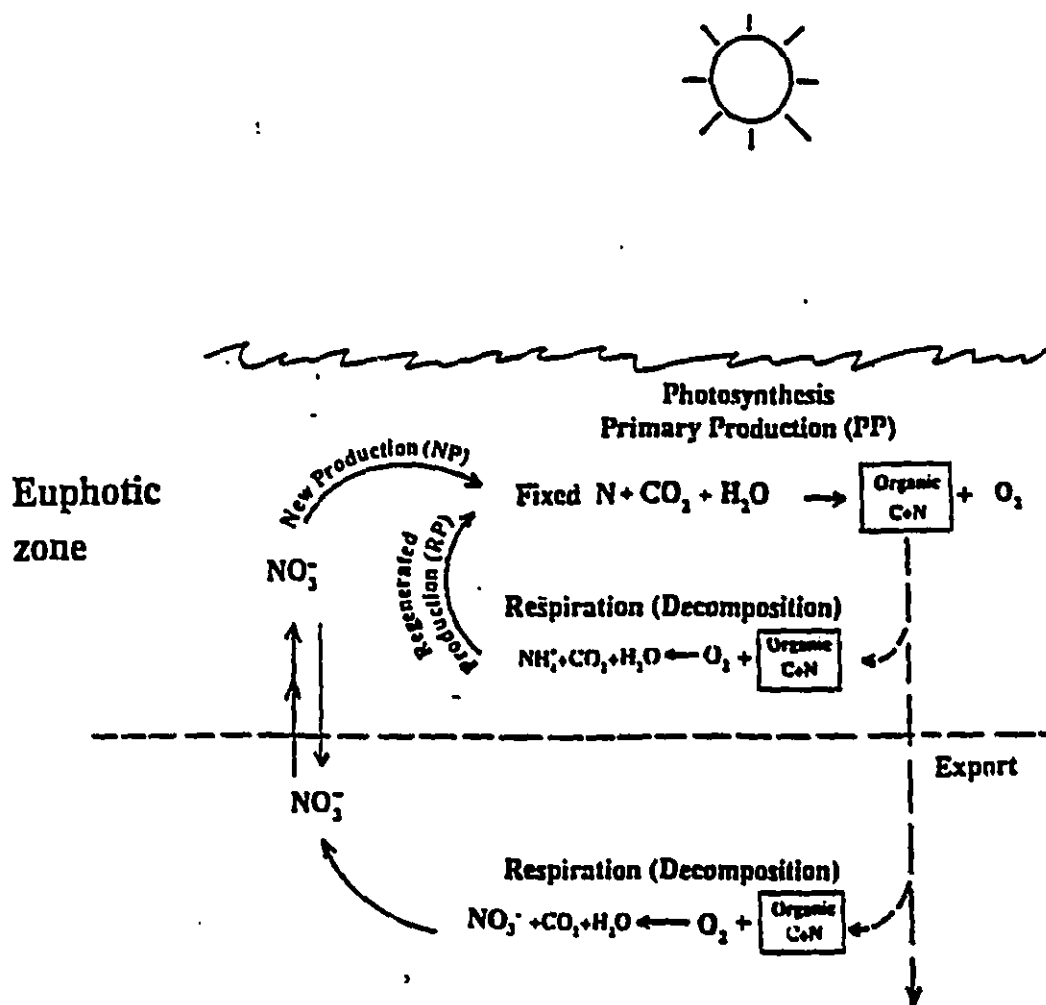


Figure 1.1 Schematic of the role of photosynthesis and decomposition in carbon and nitrogen transfer in surface waters.

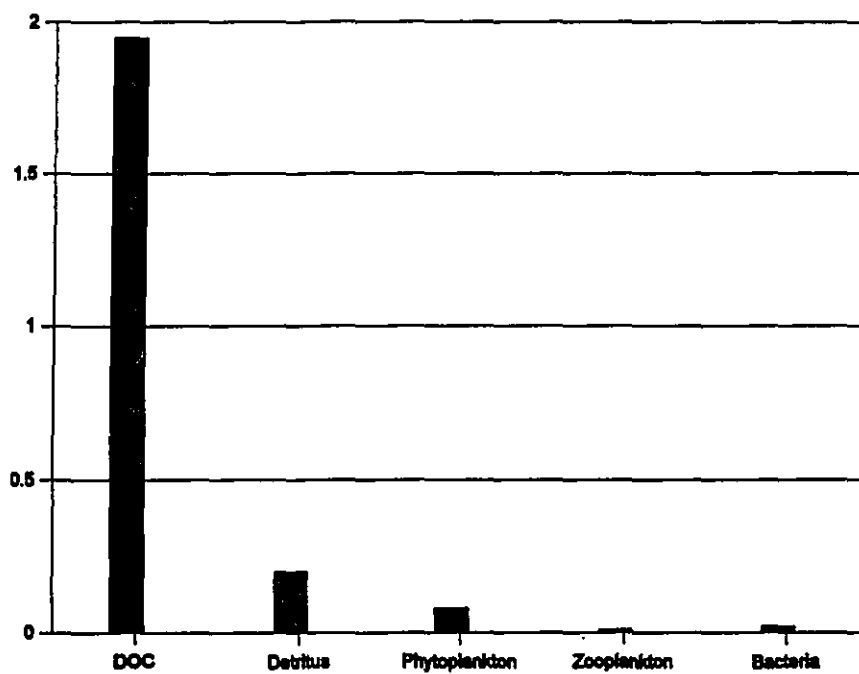


Figure 1.2 Dissolved organic carbon (DOC) and the other major source of organic carbon in the world's ocean (data taken from Cauwet, 1978), unit is:  $10^{14}$  kg.

## Chapter 2

### Model description and formulation

#### 2.1 Physical model

The ocean circulation model used in this study is a multilevel planetary geostrophic numerical model in spherical coordinates (Zhang et al., 1992), the governing equations are shown below.

$$f\mathbf{K} \times \mathbf{V} = -\rho_0^{-1} \nabla p + (\tau_s / \rho_0 H_1) \mathbf{G}(z) - \gamma_f \mathbf{V}^* \quad (2.1)$$

$$p_z = -\rho g \quad (2.2)$$

$$w_z + \nabla \cdot \mathbf{V} = 0 \quad (2.3)$$

$$Q_t + \nabla \cdot (\mathbf{V}Q) + (wQ)_z = A_h \nabla^2 Q + A_v Q_{zz} + F_b + CON \quad (2.4)$$

$$\rho = \rho(S, T) = 0.77S - 0.072T(1 + 0.072T) \quad (2.5)$$

The notation used is standard. Dependent variables are horizontal velocity ( $\mathbf{V}$ ), vertical velocity ( $w$ ), pressure ( $p$ ), density ( $\rho$ ), salinity ( $S$  in parts per thousand), temperature ( $T$ )

in °C);  $\rho_0$  is a reference density. Independent variables are time ( $t$ ), longitude, latitude and depth ( $z$ ). The remaining variables are the Coriolis parameter ( $f$ ), wind stress ( $\tau_s$ ), thickness of top model layer ( $H_1$ ), frictional dissipation coefficient ( $\gamma_f$ ), horizontal ( $A_H$ ) and vertical ( $A_v$ ) eddy diffusivity.  $Q$  is a tracer field such as temperature, salinity or a chemical tracer, with surface forcing for tracer field ( $F_b$ ); *CON* is convective adjustment to remove static instability. The vertical structure function  $G(z)$  for the surface forcing is unity in the top model layer, which is taken to be the mixed layer, and vanishes elsewhere. Eqs. (2.1)-(2.5) are the horizontal momentum, hydrostatic, continuity, tracer conservation and state equations respectively. The model equations consist of full prognostic temperature and salinity equations and diagnostic momentum equations. The latter include the geostrophic balance terms, and a linear friction in the vertically averaged component ( $V^*$ ) to provide a western boundary current. The wind stress is applied at the top level of the model. Zhang et al. (1992) showed that planetary geostrophic dynamics are capable of reproducing many of the features of the Bryan-Cox primitive equation models (Bryan, 1969; Cox and Bryan, 1984; Cox, 1985), such as the thermocline structure, tracers and potential vorticity distributions. The model has been thoroughly tested (Zhang et al., 1992) and applied to different problems in ocean-climate studies (Zhang et al., 1993, 1995).

In this study, the model domain consists of a flat-bottomed,  $60^\circ$  square box in latitude-longitude space extending between  $5^\circ\text{N}$  and  $65^\circ\text{N}$ . The horizontal resolution is  $2.3^\circ$  in both latitude and longitude, with 14 levels in the vertical. Table 2.1 gives the depth at the bottom and the thickness of each layer.

For annual mean mode simulations, the surface wind stress is zonally uniform with the meridional component being zero. The surface boundary values of temperature and salinity used in the restoring condition are taken from climatological data (Levitus, 1982). The vertical and horizontal diffusivity coefficients are  $0.63 \times 10^{-4} \text{ m}^2 \text{ s}^{-1}$  and  $2.0 \times 10^3 \text{ m}^2 \text{ s}^{-1}$  respectively.

In the seasonal mode, climatological monthly mean fields of wind stress, surface temperature and salinity are used (Hellerman and Rosenstein, 1983; Esbensen et al., 1981). The surface wind stress forcing is again zonally uniform with the northward component being zero. The horizontal diffusivity coefficient is as before, while the vertical diffusivity ranges from 0.63 to 0.83  $\text{cm}^2/\text{s}$ .

## **2.2 Biological model**

The model for the cycling of organic matter in the ocean used in this study is shown schematically in Figure 2.1 (Najjar, 1990; Najjar et al., 1992; Anderson et al., 1993). Inorganic nutrient is taken up in the euphotic zone and released below, while at the same time, organic matter is formed in the euphotic zone and consumed below. The cycles are closed by transport processes, including ocean circulation and particle settling. These processes carry organic matter from the surface layer to the deep ocean, and inorganic nutrient in the opposite direction.

New production (NP) is parameterized following Najjar (1990) and Najjar et al. (1992). New production is determined by restoring the nitrate concentration in the

euphotic zone to a horizontally uniform vertical distribution determined from observations. This model of new production will be termed the "restoring biological model". The top three model levels, extending to a depth of 114 m, make up the euphotic zone. New production occurs whenever the surface nitrate concentration exceeds observations:

$$NP = - \{ [NO_3] - [NO_3]^* \} / \tau, \quad z > z_e, \quad [NO_3] > [NO_3]^* \quad (2.6)$$

$$NP = 0, \quad z > z_e, \quad [NO_3] \leq [NO_3]^* \quad (2.7)$$

where  $[NO_3]^*$  is the observed nitrate concentration,  $[NO_3]$  is the model nitrate concentration,  $z_e = -114$  m is the depth of the euphotic zone, and  $\tau$  is a restoring time scale which characterizes the forcing of the surface nitrate concentrations towards, but not precisely at, their observed values. For a large spatial scale of order 1000 km and a velocity scale of order  $0.1 \text{ m s}^{-1}$ , the restoring time scale is taken to be the advective time scale, which is about 100 days. Note that  $z$  is positive upwards.

New production can also be parameterized using an extension of the Michaelis-Menton enzyme kinetic equation applied to whole organisms (Dugdale, 1967). This model will be termed the "kinetic biological model", and is similar to the biological model of Bacastow and Maier-Reimer (1991). In this case, new production is calculated in the euphotic zone according to Dugdale (1967).

$$NP = R[NO_3]/(H + [NO_3]) \quad (2.8)$$

Here,  $[NO_3]$  is the model simulated nitrate concentration, with  $R$  and  $H$  being constants. The constants are adjusted to give the best simulation compared to observations.

The relation between the kinetic (Eq. (2.8)) and restoring (Eq. (2.6)) models can be understood as follows. When  $[NO_3]/H < 1$ , the equation for the kinetic model can be

expanded as,

$$\begin{aligned} NP &= R/H([NO_3] - [NO_3]^2/H + [NO_3]^3/H^2 - \dots) \\ &\approx R/H[NO_3] ; \text{ when } [NO_3] \ll H \end{aligned} \quad (2.9)$$

For most of the ocean, the observed nitrate concentration  $[NO_3]^*$  is close to 0. Thus the restoring model becomes close to the kinetic model, if the restoring time scale is chosen appropriately:  $1/\tau = R/H$ . If on the other hand,  $[NO_3]/H > 1$ , the kinetic model becomes,

$$NP = R\{1 - H/[NO_3] + (H/[NO_3])^2 - (H/[NO_3])^3 + \dots\} \quad (2.10)$$

In this limit, the restoring model is different from the kinetic model.

Consider in more detail the limit of  $[NO_3]/H < 1$ . As noted already, choosing  $\tau = H/R$  matches the time scales of the two models. In this case, the maximum production rate for the kinetic model is  $R = H/\tau$ . The production rate for the restoring model is  $NP = [NO_3]/\tau$ , which has a maximum value of  $NP_{\max} = H/\tau$  in this limit. The maximum production rates calculated from both models are identical. With  $H = \text{constant}$ , the normalized production rate can be defined as  $NP/R$  for the kinetic model, and  $NP/NP_{\max}$  for the restoring model. The variation of the normalized production rate as a function of the dimensionless nitrate concentration  $[NO_3]/H$  is shown in Figure 2.2. We see that for  $[NO_3] < H$ , the restoring model is well approximated by the kinetic model. For  $[NO_3] > H$ , i.e., plentiful nutrient, the two models are quite different from each other, and the production rate should be given by the kinetic model.

Estimates of the maximum production rate for the kinetic model are available for some species. Using Riley's (1963) data of the diatoms generation time and PON concentration from the Black Sea, Dugdale (1967) computed this maximum

consumption/production rate. They range from 0.034 mmol-N m<sup>-3</sup> hr<sup>-1</sup> for *Rhizosolenia alata* Bright, to 0.068 mmol-N m<sup>-3</sup> hr<sup>-1</sup> for *Chaetoceros socialis* and 0.226 mmol-N m<sup>-3</sup> hr<sup>-1</sup> for *Skeletonema costatum*. The production rate can thus vary significantly depending on species. For the restoring model, the choice of  $\tau = 30$  or 60 days yields production rates of 0.014 and 0.007 mmol-N m<sup>-3</sup> hr<sup>-1</sup> respectively, for  $H=10$  mmol-N m<sup>-3</sup>. With  $\tau=30$  or 60 days, the maximum growth rate from the kinetic model  $R=H/\tau$ , which is obtained in the limit of  $[NO_3]/H < 1$ , is comparable with some of these lower production rate estimates.

A certain fraction ( $\sigma_p$ ) of new production is taken to be non-sinking particulate and dissolved organic nitrogen (together designated as DON), while the remainder ( $1-\sigma_p$ ) is put into sinking particulate organic nitrogen (PON). PON is immediately transferred out of the euphotic zone, with a sinking flux  $F(z)$ . Remineralization of this flux is parameterized as an instantaneous process, using a power law (Martin et al., 1987),

$$F(z) = F_e(z/z_e)^a \quad (2.11)$$

or an exponential function (Volk and Hoffert, 1985),

$$F(z) = F_e \exp[(z - z_e)/z^*] \quad (2.12)$$

where  $a$ ,  $z^*$  are constants which are estimated using observational data;  $z_e = -114$  m is the depth of euphotic zone.  $F_e$  is the flux of particulate organic matter at the base of the euphotic zone, obtained by integrating the particle concentration generated within the euphotic zone each time step. All the PON reaching the seafloor at any given location is immediately remineralized in the bottom ocean box.

An effective length scale for the particle flux is the depth below the euphotic zone

at which the particle flux is equal to 1/e of its value at the bottom of euphotic zone. For the power law parameterization with  $z_c = -114$  m and  $a = 0.858$ , this depth is 365.6 m, a relatively shallow remineralization depth. The exponential formulation was used by Volk and Hoffert (1985) and by Fiadeiro and Craig (1978) for the deep ocean. Volk and Hoffert (1985) found  $z^* = 700$  m, and Najjar et al. (1992) chose  $z^* = 800$  m for their simulation. A value of 800 m was chosen in our simulations.

Non-sinking and dissolved organic nitrogen (DON) is allowed to advect and diffuse out of the euphotic zone; once below the euphotic zone it remineralizes at a rate which is proportional to its concentration,

$$J_{\text{DON}} = -\kappa[\text{DON}] \quad (2.13)$$

where  $\kappa$  is the rate constant for DON remineralization. Since there are no data available to determine  $\kappa$ , it is calculated based on the condition that total DON consumption below the euphotic zone is equal to total DON production within the euphotic zone. It is possible that at depth, bacteria are the exclusive consumers of dissolved organic matter, so  $\kappa$  might be proportional to bacterial abundance. A rough fit to the bacterial biomass data of Cho and Azam (1988) gives an e-folding depth scale of  $z^* = 750$  m; we thus take  $\kappa$  to vary exponentially with depth with this scale,

$$\kappa = \kappa' \exp[(z - z_c)/z^*] \quad (2.14)$$

where,  $\kappa'$  is a remineralization rate for DON at the base of the euphotic zone and calculated at each time step to ensure the total remineralization equals the new production at each time step.

## 2.3 Model of seasonal oxygen cycle

When there is new production in the model, oxygen is generated through a Redfield ratio ( $R_{N:O_2}$ ).

$$\text{Production of } O_2 = NP / R_{N:O_2} \quad (2.15)$$

where NP is calculated from either Eq. (2.6) or Eq. (2.8), and  $R_{N:O_2}$  is  $N:(-O_2)=16:172$ , taken from Takahashi et al. (1985).

Below the euphotic zone, oxygen consumption ( $J_O$ ) is proportional to organic nitrogen remineralization, only when dissolved oxygen is available. In anoxic regions below the euphotic zone, consumption of dissolved oxygen is set equal to zero. Thus for  $z < z_e$ ,

$$J_O = (J_{DON} + \partial(F(z))/\partial z) / R_{N:O_2}, \quad [O_2] > 0 \quad (2.16)$$

$$J_O = 0, \quad [O_2] = 0 \quad (2.17)$$

$[O_2]$  is dissolved oxygen concentration;  $J_{DON}$  and  $F(z)$  have already been defined in Eq. (2.13) and Eq. (2.11) respectively. Note that in our model remineralization of nitrogen is unaffected by oxygen concentration.

The oxygen exchange with the atmosphere is parameterized as:

$$K_w([O_2]^* - [O_2]) = A_v \partial[O_2]/\partial z \quad (2.18)$$

where  $[O_2]^*$  is the concentration of dissolved oxygen in seawater at equilibrium with moist air;  $K_w$  is the piston velocity with units of  $\text{cm h}^{-1}$ .  $[O_2]^*$  is primarily a function of temperature with a weak dependence on salinity, and is computed from the formula of Weiss (1970). The piston velocity is calculated according to the Liss and Merlivat (1986)

formulation:

$$K_w = 0.17 U_{10} (600/S_c)^{0.66}, U_{10} < 3.6 \text{ m s}^{-1} \quad (2.19a)$$

$$K_w = (2.85 U_{10} - 9.65)(600/S_c)^{0.5}, 3.6 < U_{10} < 13 \text{ m s}^{-1} \quad (2.19b)$$

$$K_w = (5.9 U_{10} - 49.3)(600/S_c)^{0.5}, U_{10} > 13 \text{ m s}^{-1} \quad (2.19c)$$

$S_c$  is the Schmidt number, which has a strong temperature dependence and a weak dependence on salinity (Jahne et al., 1987). Jahne (1980) has measured the Schmidt number of oxygen in pure water at various temperatures. A polynomial fit to his data (Najjar, 1990) gives for  $S_c$ :

$$S_c(\text{O}_2) = 1450 - 72.416T + 1.3125T^2 - 0.99708T^3 \quad (2.20)$$

The Schmidt number is calculated by using climatological monthly temperature.

## 2.4 An alternative model of organic particles

Dissolved organic matter is operationally defined as that fraction of particulate organic matter that passes through a filter of pore size of the order of 0.5  $\mu\text{m}$ . Therefore, we could also consider all organic matter to exist as particles in two size fractions, a reservoir of fine particles which is suspended in the water column and does not sink due to gravity, and a small number of large, sinking particles. Based on this division, the time dependent 1-dimensional particle cycle model shown below is a simple representative of oceanic organic particle cycling (Figure 2.3). The model is similar to, but not identical with the one formulated by Clegg and Whitfield (1990, 1991),

$$\partial P_s / \partial t = P_r - P_s(\gamma + r_1) + r_2 P_l + K_{vs}(\partial^2 P_s / \partial z^2) \quad (2.21)$$

$$0 = r_1 P_s - P_l(\gamma + r_2) - \partial F_l / \partial z \quad (2.22)$$

$$F_l = P_l S \quad (2.23)$$

where  $F_l$  is the large particle flux,  $z$  (m) is the depth, and  $S$  is the particle falling speed. The physical processes described by the model are shown in Figure 2.3. In surface waters, gross primary production ( $P_g$ ;  $\text{g m}^{-3} \text{ yr}^{-1}$ ) supports the reservoir of small, suspended particles ( $P_s$ ;  $\text{g m}^{-3}$ ), which make up most of the particle mass. The primary organic matter thus produced can either be remineralized back to inorganic matter with rate constant  $\gamma$  ( $\text{yr}^{-1}$ ), or are aggregated with rate constant  $r_1$ , ( $\text{yr}^{-1}$ ) to produce large, sinking particles ( $P_l$ ;  $\text{g m}^{-3}$ ). The large particles may sink, be remineralized to inorganic matter, or broken up with rate constant  $r_2$  ( $\text{yr}^{-1}$ ) to return material to the suspended particle reservoir. The suspended particle pool is also influenced by diffusion and advection processes. The vertical diffusivity for suspended particles in the 1-dimensional model is  $K_{vs} = 1 \text{ cm}^2 \text{ s}^{-1}$ . When this model is later embedded in the 3-dimensional planetary geostrophic model, the physical vertical diffusivity of the latter is used instead.

Our model is different from the time dependent model used by Cleg and Whitfield (1993). The later does not simulate  $P_s$ , but instead, its daily values are obtained from observational data. The time series of  $P_s$  values and daily primary production rates are used to calculate the particle flux. In our model, the initial  $P_s$  and  $P_l$  fields are set to zero, and we only use vertically integrated observational primary production rate as the forcing term. Both the  $P_s$  and  $P_l$  fields, as well as the particle flux, are simulated by numerical integration. This particle cycling model used here is to examine interactions between the large sinking particle and fine suspended particle, thus is different from the

biological model used for parameterization of new production which was presented in section 2.2 and section 2.3.

The gross primary production ( $P_g$ ) only takes place in the euphotic zone; elsewhere, it is set to zero. Aggregation and disaggregation are the result of different physical and biological processes operating over the full particle size spectrum. There are some observations available to determine the values of the model parameters. Nozaki et al. (1987) estimate the rate constants  $r_1$  and  $r_2$  based on data of scavenged thorium isotopes in the western Pacific sites AN-1 and AN-4. Their results show that for sinking rates exceeding  $36 \text{ m day}^{-1}$ , the ratio  $r_1/r_2$  is almost constant. Using the particulate matter distributions and flux data set of Bishop et al. (1980), Clegg and Whitfield (1990) also obtained estimates of these rate constants independently of trace metal data, which are consistent with the values estimated by Nozaki et al. (1987). In this work, we use the rate constants of aggregation ( $r_1$ ) and disaggregation ( $r_2$ ) of Clegg and Whitfield (1990).

In this work, we use a remineralization rate ( $\gamma$ ) which is 50% larger than Clegg and Whitfield (1990). We have performed experiments using  $\gamma$  values which ranges from half to double Clegg and Whitfield's values. We found that the choice of a distribution which is 50% higher than Clegg and Whitfield's value gave the best agreement with observations (Knauer and Martin, 1981); the higher remineralization rates were also used in a later study by Clegg et al. (1991). In chapter 5, we show sensitivity results to variations in the remineralization rates. Table 2.2 shows the distribution of the model parameters (rate constant of remineralization, aggregation and disaggregation) for the 1-dimensional model. Table 2.3 shows the parameter values for the 3-dimensional model,

where the 1-dimensional particle model is embedded in the 3-dimensional physical model. The values shown in Table 2.2 and 2.3 are similar except the vertical resolution is decreased from 27 to 14 levels. For the large particles, an averaged sinking velocity ( $S$ ) of  $100 \text{ m day}^{-1}$  (Bacon et al., 1985) is used.

For the numerical integration of the 1-dimensional time dependent particle model, we use a time step of  $\Delta t=10\text{-}30$  minutes, which satisfies the stability requirement of  $(\gamma+r_1)\Delta t < 1$  and  $r_2\Delta t < 1$ . The 3-dimensional planetary geostrophic physical model was developed for climate studies, and it uses a time step of order of a few days. In this work, a time step of 1 day is used. Thus the steady state version of the 1-dimensional particle model is embedded in the 3-dimensional model, with the latter run in the annual mean mode.

## 2.5 Summary

We have described the physical and biological components of the model to be used in this study. In the next three chapters, we present and discuss the results of three coupled model simulations. In chapter 3, the annual mean physical model and the restoring biological model are coupled to study nutrient cycling. Chapter 4 examines the oxygen seasonal cycle, using the seasonal version physical model coupled to the kinetic biological model. In chapter 5, organic particle cycling in the ocean is examined by introducing a 1-dimensional particle model, and coupling the steady state of this 1-dimensional particle model with the annual physical model.

Table 2.1 Depths (m) at the bottom, and thickness (m) of each layer in the 3-dimensional planetary geostrophic model.

Layer	Depth	Thickness
1	28	28
2	65	37
3	114	49
4	179	65
5	265	89
6	378	113
7	528	150
8	726	198
9	989	263
10	1336	347
11	1796	460
12	2404	608
13	3202	798
14	4000	798

Table 2.2 Parameters of the 1-dimensional particle cycle model. N is the level number corresponding to the depth z (m).  $\gamma$ ,  $r_1$  and  $r_2$  are the rates constants for remineralization, aggregation and disaggregation respectively, all in units of  $\text{yr}^{-1}$ .

N	z	$\gamma$	$r_1$	$r_2$
1	5	37.1	366.0	6007.0
2	10	61.5	327.0	9881.0
3	15	62.3	290.0	10123.0
4	20	59.1	257.0	9566.0
5	30	49.5	201.0	8014.0
6	40	41.5	158.0	6575.0
7	60	27.6	104.0	4526.0
8	80	20.5	74.0	3331.0
9	100	16.2	57.0	2622.0
10	120	11.5	40.0	1861.0
11	140	9.6	34.0	1569.0
12	160	8.4	29.0	1352.0
13	180	7.4	25.5	1185.0
14	200	6.5	22.7	1052.0
15	250	5.1	17.6	815.0
16	300	4.1	14.2	660.0
17	350	3.5	11.9	551.0
18	400	2.9	10.1	470.0
19	600	1.8	6.2	287.0
20	800	1.2	4.3	199.0
21	1000	0.9	3.2	148.0
22	1500	0.5	3.2	148.0
23	2000	0.3	3.2	148.0
24	2500	0.2	3.2	148.0
25	3000	0.2	3.2	148.0
26	3500	0.1	3.2	148.0
27	4000	0.1	3.2	148.0

Table 2.3 Parameters of the 3-dimensional particle cycle model. N is the level number corresponding to the depth z (m).  $\gamma$ ,  $r_1$  and  $r_2$  are the rates constants for remineralization, aggregation and disaggregation respectively, all in units of  $\text{yr}^{-1}$ .

N	z	$\gamma$	$r_1$	$r_2$
1	28	28.5	201.0	8400.0
2	65	17.0	100.0	4200.0
3	114	8.0	45.0	1950.0
4	179	4.9	25.5	1185.0
5	265	3.0	16.0	780.0
6	378	2.2	11.0	505.0
7	528	1.5	7.8	350.0
8	726	0.9	5.0	240.0
9	989	0.6	3.2	148.0
10	1336	0.4	3.2	148.0
11	1796	0.3	3.2	148.0
12	2404	0.2	3.2	148.0
13	3202	0.1	3.2	148.0
14	4000	0.1	3.2	148.0

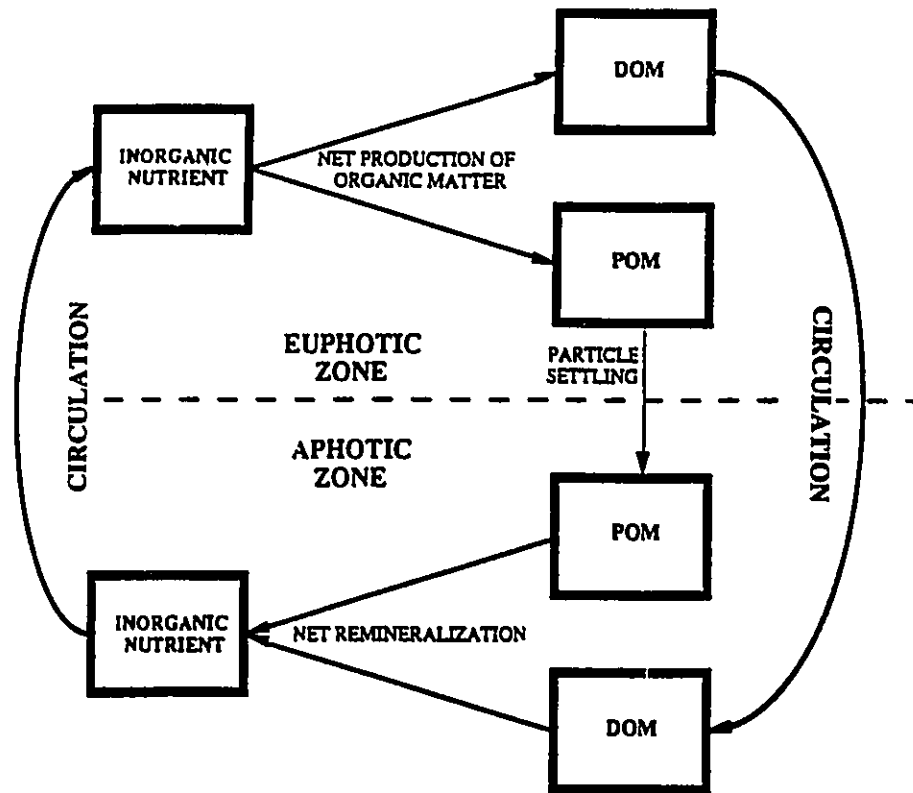


Figure 2.1 A simple schematic diagram of the cycling of organic matter in the ocean. Organic matter is formed in the euphotic zone during photosynthetic uptake of inorganic nutrient. It is then transported below the euphotic zone by ocean circulation and particle sinking, where it is remineralized back to inorganic nutrient. The figure is adapted from Najjar (1990).

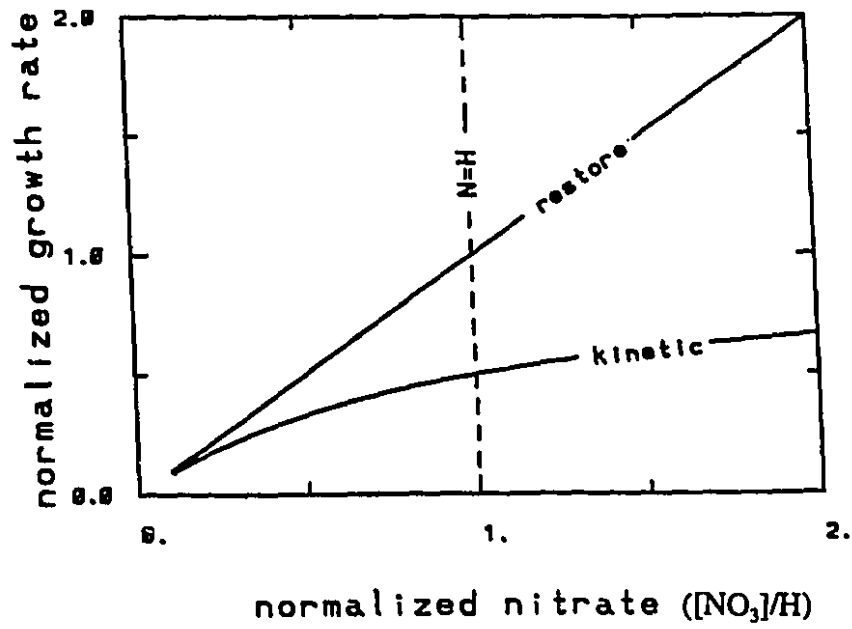


Figure 2.2 A comparison of the normalized production rates of the kinetic (NP/R) and restoring (NP/NP<sub>max</sub>) models, as a function of the dimensionless nitrate concentration ([NO<sub>3</sub>]/H). The restoring and kinetic models are close to each other when [NO<sub>3</sub>] < H.

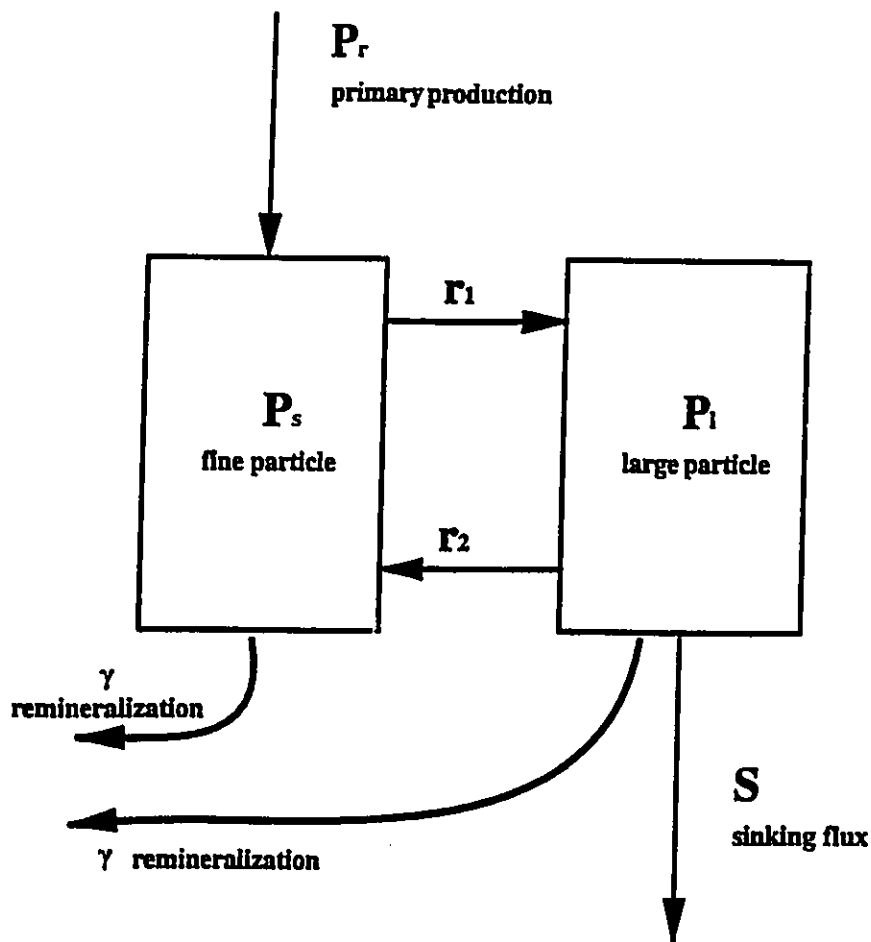


Figure. 2.3 A schematic description of the particle model. Small particles ( $P_s$ ) are produced at a rate  $P_r$  corresponding to primary production and exchanged with a reservoir of large particles ( $P_l$ ) by aggregation and disaggregation, with rate constants  $r_1$  and  $r_2$ . Large particles ( $P_l$ ) are removed from the water column by sinking, with sinking rate  $S$ . Remineralization, with rate constant  $\gamma$ , returns particulate material to the inorganic state. This figure is adapted from Clegg and Whitefield (1990).

## Chapter 3

# Nitrate cycle modelling in the North Atlantic ocean

### 3.1 Introduction

The observed distribution of nutrients in the ocean results from the interplay of biological processes, such as nutrient uptake in the euphotic zone and remineralization of organic matter at depth, with the physical transport processes of advection and diffusion.

A current controversial and important problem is the determination of new production rates in the oligotrophic ocean. Measurements of oxygen consumption (Jenkins, 1982; Jenkins and Goldman, 1985) suggest that open ocean new production is much higher ( $\sim 4 \text{ mol-C m}^{-2} \text{ yr}^{-1}$ ) than previously believed. To support such a high new production rate, large amount of nutrients would have been introduced into the euphotic

zone. This new value is comparable with previous estimates of the primary production rate in oligotrophic waters (e.g. Ryther, 1969), suggesting that the  $^{14}\text{C}$  technique may underestimate rates of primary production, if f-ratios, i.e., ratio of new production to total production, of typical oligotrophic oceans are applied (Eppley and Peterson, 1979). On the other hand, using the averaged f-ratios factors, Platt and Harrison (1985) found that rate of primary production as currently measured are representative of those occurring *in situ*. Clearly, accurate estimation of new production in the oligotrophic ocean is of fundamental importance in understanding the role of the biological pump in the oceanic carbon cycle.

As mentioned earlier, measurements of oxygen consumption suggest that open ocean new production is much higher than previous believed. Martin et al. (1987) offered a hypothesis to explain the difference between new production estimates from the VERTEX experiment in the North Pacific and results from OUR (oxygen utilization rate) calculations. Their explanation is based on evidence from radionuclide work that both large and small particles must be considered in order to understand the carbon and nutrient cycles in the ocean. Martin et al. suggested that slow or non-sinking organic matter will be entrained by water sinking from the surface in the North Atlantic. As this water flows along isopycnals in the Sargasso Sea, the entrained particulate organic matter (POM) decomposes. This remineralization together with that from the fast sinking particles exiting the overlying local surface waters results in high remineralization rates ( $3.1\text{-}3.8 \text{ mol-C m}^{-2} \text{ yr}^{-1}$ ). Most of this remineralization results from the lateral transport of the non-sinking POM originally produced some distance away at the surface. If this

hypothesis is correct, unusually large amounts of new production would not have had to occur in the oligotrophic waters of the Sargasso Sea and unaccountably large amounts of fixed nitrogen would not have had to be introduced into the photic zone to fuel this new production.

Rintoul and Wunsch (1991) examined the distribution and transport of nutrients in the subtropical North Atlantic. They used Wunsch's (1978) inverse method to determine the extent to which different properties are independent, and to test a variety of conservation and flux constraints. Their results indicate a net divergence of nitrate in the mid-latitude band. Following Martin et al.'s (1987) arguments, Rintoul and Wunsch hypothesized that remineralization of horizontally advected non-sinking organic matter along isopycnals could provide the source required to balance this nitrate divergence.

Najjar et al. (1992) used a phosphorus-based model of nutrient cycling and a general circulation model to evaluate the roles of the dissolved phases in the downward transport of organic matter in the ocean. Their results show that the downward transport of organic matter occurs primarily in the dissolved phase. Model simulations performed by Bacastow and Maier-Reimer (1991) suggested that a significantly better agreement between predicted and observed oceanic phosphate concentrations can be obtained if a large part of the new production flux occurs as transport of dissolved organic carbon.

There are still few reliable measurements of organic matter concentration over the water column to test the Martin et al. (1987) hypothesis. Numerical modelling can improve our understanding of nutrient cycles in the North Atlantic ocean. In this chapter, we use the numerical model described in chapter 2 to test the hypothesis of Martin et al.

(1987), and to evaluate the role of the Gulf Stream in nutrient transport.

Our work will focus on the nitrate budget in the North Atlantic subtropical gyre. In this region, anoxic conditions or denitrification have not been observed. In the following section we describe the experimental design; and in section 3.3 we present results of the simulated nitrate zonal distribution; in section 3.4 the meridional transport and its spatial distribution; in section 3.5 nitrate regeneration is discussed, and in section 3.6 the summary.

## 3.2 Experiments design

As mentioned in Chapter 2, we couple an ocean circulation model representing the annual mean mode with a restoring biological model. The goal is to examine nitrate cycling in the North Atlantic.

We have conducted six simulations, summarized in Table 3.1. All simulations include non-sinking and dissolved organic matter (ie.  $\sigma_d > 0$ , the fraction of new production that is dissolved or non-sinking). Observations of organic phosphorus fluxes as a fraction of new production suggest values of  $\sigma_d$  between 0.4 and 0.8 (Najjar et al., 1992). Anderson and Sarmiento (1994) and Anderson (1993), using the model of Najjar et al. (1992) to study the time-mean, basin-wide Redfield ratio, suggested that the value  $\sigma_d=0.5$  is a reasonable choice.

The nitrate and dissolved organic nitrogen distributions were initialized using typical depth profiles. The nitrate vertical profile was taken from Broecker and Peng

(1982), resulting in a mean North Atlantic nitrate concentration of  $20.37 \text{ mmol-N m}^{-3}$ . For non-sinking and dissolved organic nitrogen, values in the top 900 m were taken from Jackson and Williams (1985), and held constant at the value at 900 m below that depth. Both nitrate, PON and DON are conserved in the model.

The circulation model was first spun up for 1200 years, with a timestep of 3 days. With the nutrient field included, the model was run for another 2100 years. Convective adjustment takes place when the density in any control volume exceeds the value below it; temperature, salinity and density in two adjacent volumes are then mixed in such a way as to guarantee a stable profile. When convection occurs, the nutrient field is treated in the same way as the salinity field. Model diagnostics were constructed from averages during last 100-year period of the simulation.

### **3.3 Zonal nitrate distribution**

Figure 3.1 shows the transport by the meridional overturning circulation and horizontal velocity fields at a depth of 46 m at the end of 2100 years of integration: the maximum transport is 12.4 Sv. Toggweiler et al. (1989a, b) used radiocarbon to investigate the Geophysical Fluid Dynamics Laboratory global coarse resolution ocean model's ability to ventilate deep water. In their prognostic model simulation, the model yields a transport of 15 Sv in the North Atlantic ocean. Their model is based on the primitive equation model described by Bryan (1979), and Bryan and Lewis (1979). Our model, based on the planetary geostrophic equations, thus yields a comparable maximum overturning

transport in the North Atlantic.

The simulated nutrient distribution for a zonally averaged meridional section for three simulations is shown in Figure 3.2. For the biological model we employed, new production is parameterized by restoring the nutrient field towards the observed nutrient field at every time step. When upwelled water rich in nitrate is exposed to the sun light, photosynthesis will take place, and the new production utilizes the newly supplied nitrate. The nitrate distributions are in reasonable agreement with the observations of Fukumori et al. (1991, their Figures 45 and 51). The low values near the surface result from both biological and physical processes. Primary production removes the nitrate in the euphotic zone, thus lowering the nitrate concentration. Near the northern boundary, convective adjustment mixes the entire water column, giving a local minimum. The downwelling advects the nutrient depleted water to the deep ocean. This also can be seen in the domain averaged vertical profiles (Figure 3.3). The upwelling of water rich in nitrate causes the nitrate concentrations to be higher than observed in the upper layers, triggering primary production in the model. The localized downwelling of water poor in nitrate at the northern edge of the model results in lower concentrations than observed.

In the deep layers, the simulated vertical nitrate profiles of Experiments P3.5, P6.5 and P3.7 using the power law for remineralization are closer to the observed profile than those obtained with the exponential formulation (Figure 3.3). Figure 3.3 also shows that the exponential function results in higher values at mid-depths (800-2000 m). The root-mean-square difference between the simulated basin averaged and the observed profile are 1.08, 1.01, 1.07, 0.90, 0.81, 0.99 ( $\text{mmol-N m}^{-3}$ ) for the six Experiments E3.5,

E6.5, E3.6, P3.5, P6.5 and P3.7 respectively, thus confirming the better performance of the power law representation.

### 3.4 Meridional transport of nitrate and DON

The vertically and zonally integrated meridional nitrate transport for Experiments E3.5 and P3.5 are shown in Figure 3.4: transport is calculated as the product of the meridional velocity ( $v$ ) and the nitrate concentration ( $[NO_3]$ ). All six experiments produce a general net northward transport in the mid-latitude, peaking near  $30^\circ N$ . Table 3.2 shows numerical values of the transports across  $24^\circ N$  and  $36^\circ N$ . These latitudes are selected as Rintoul and Wunsch (1991) provided estimates of transports across these latitudes using an inverse method. The northward transport at  $24^\circ N$  ranges from 15.2 to 23.3  $kmol\ s^{-1}$  and from 77.2 to 91.7  $kmol\ s^{-1}$  across  $36^\circ N$ . This flux divergence across the  $24^\circ$ - $36^\circ N$  latitude band means there is a net advective loss of nitrate in this band, which must be replaced by a source. For the top 1000 m, the northward transport across  $30^\circ N$  is about 260  $kmol\ s^{-1}$ , and in a steady state the total vertically integrated transport is around 95  $kmol\ s^{-1}$  for Experiments E3.5 and P3.5 (Figure 3.4). This means that there must be a southward transport of about 165  $kmol\ s^{-1}$  in the lower layer, between 1000 m and the bottom. From Table 3.2, we see that the simulated transports across  $24^\circ N$  and  $36^\circ N$  are within Rintoul and Wunsch's estimates  $-8 \pm 39\ kmol\ s^{-1}$  across  $24^\circ N$  and  $119 \pm 35\ kmol\ s^{-1}$  across  $36^\circ N$ .

Figure 3.5 shows the vertically and zonally integrated non-sinking and dissolved

organic nitrogen meridional transport calculated as the product of the meridional velocity ( $v$ ) and the DON concentration ( $[DON]$ ). The southward total transport across  $24^{\circ}N$  range from 17.8-33.8  $kmol\ s^{-1}$ , while it is between 63.1-81.7  $kmol\ s^{-1}$  across  $36^{\circ}N$  (Figure 3.5; Table 3.2). There is thus a flux convergence, or net gain of non-sinking and dissolved organic matter in the latitude band  $24^{\circ}$ - $36^{\circ}N$ . The large input across  $36^{\circ}N$  is essential to balance the divergent transport of nitrate out of this band. A more detailed discussion of regeneration of nitrate will be presented in section 3.5.

We now discuss the effect of the restoring time scale ( $\tau$ ) for the parameterization of new production. We have tested  $\tau = 30, 60$  days for both the exponential and power law formulations. As mentioned earlier, the advective time scale for the large spatial scale is of order 100 days; the restoring time scale is thus less than the advective time scale. Table 3.2 indicates that a longer restoring time scale (Experiments E6.5 and P6.5) results in lower new production and less meridional transport. This is because a longer restoring time implies a slower turnover rate of nitrogen species between the nitrate pool and the non-sinking and dissolved organic matter pool, thus resulting in a lower rate of primary production.

Martin et al. (1987) suggested horizontal transport of non-sinking organic matter results in a high rate of remineralization in the aphotic zone compared to the new production rate in the euphotic zone in the mid-latitude water column. For the  $24^{\circ}$ - $36^{\circ}N$  mid-latitude band, the simulated net divergence of inorganic nitrate and convergence of non-sinking organic matter is consistent with this hypothesis.

We now examine the longitudinal distribution of the nitrate transport across the

basin. To do this, the model domain has been divided into three meridional sections, each of them  $14^{\circ}$  wide. They are designated western ( $3^{\circ}$ - $17^{\circ}$  longitude), central ( $24^{\circ}$ - $38^{\circ}$  longitude) and eastern ( $42^{\circ}$ - $56^{\circ}$  longitude) sections. Figure 3.6 shows the zonally and vertically integrated nitrate meridional transport in these sections for Experiment P6.5; the other experiments yield similar results. In the western section, there is a strong northward transport in the upper 1000 m at mid-latitude between  $15^{\circ}$ N to  $40^{\circ}$ N. North of latitude  $40^{\circ}$ N, the nutrient transport is close to zero in the upper 1000 m, but the total transport is southward and carried by deep water below 1000 m. In the central and eastern sections, upper layer nutrient transport accounts for most of the southward transport at mid-latitudes between  $15^{\circ}$ - $35^{\circ}$ N, and transports are northward north of latitude  $40^{\circ}$ N. The zonally averaged meridional transport (Figure 3.4) shows a net northward transport, and we see from Figure 3.6 that this is mainly accomplished by the Gulf Stream in the western section. Bennett and White (1986) calculated the meridional heat flux in the North Pacific, and found that their estimate was largely dependent on whether or not they captured a strong northward flow of the Kuroshio south of Japan. In our simulations, a northward nutrient flux results from a correlation of high nutrient concentration with a strong northward Gulf Stream flow. These correlations are decreased by averaging the observational data over the entire basin (Rintoul and Wunsch, 1991). Hence, the data smoothing scheme used in nutrient transport calculations should be carefully chosen to resolve signals from the Gulf Stream.

The northward flowing upper layers of the Gulf Stream are exposed to the atmosphere and cooled. The vertical mixing driven by this strong cooling introduces a

large flux of nitrate into the sunlit surface layers and supports the very high productivity in the northern region. This high productivity region can also be observed along the axis of the North Atlantic Current in satellite images of ocean colour (e.g., Esaias et al., 1986). In our model, the new production is divided into two pools, particulate organic nitrogen (PON), and non-sinking particulate and dissolved organic nitrogen (DON). The PON pool is locally remineralized back to nitrate below the euphotic zone according to the power law or exponential formulations. Only the DON pool is transported and diffused. A significant fraction of this DON pool is then transported southward by the Gulf Stream return flow in the central and eastern sections of the basin.

### **3.5 Remineralization and nitrate regeneration**

In the model simulation, DON, transported by the ocean circulation, is remineralized below the euphotic zone at a rate proportional to its concentration. In section 3.3, we showed that there is a divergence of the nitrate flux, and hence a convergence of the DON flux in the mid-latitude band  $24^{\circ}$ - $36^{\circ}$ N. To balance the nitrate divergence, an input of regenerated nitrate to the Gulf Stream region is required. Model results suggest that a significant source of nitrate within this latitude band could be provided by the remineralization of DON transported into the band from the north.

In the northern North Atlantic, there is no obvious sink of nitrate. Inflow from the Pacific through the Arctic Ocean and river run-off are in fact a net source of nitrate to the North Atlantic, adding to the mid-latitude convergence (Meybeck, 1982). Evidence

from sediment cores suggests that organic matter is not being buried in the sediments in the northern North Atlantic in large amounts at the present time (Broecker and Peng, 1982). The nitrate flux must support a high productivity, whereby the nitrate is converted to organic matter. Part of the organic matter is transported southward by the ocean circulation as DON. Most of the southward transport occurs in the top 1000 m (Figure 3.6), suggesting that it is the horizontal circulation associated with the Gulf Stream return flow that transports most of the DON to the mid-latitude region.

Figure 3.7 shows the vertically and zonally averaged new production in the euphotic zone, and the vertically and zonally averaged remineralization of total organic matter, including both PON and DON, in the aphotic zone. Most of the new production occurs in the northern part of the basin, which also supports a large remineralization rate. For all 6 experiments, the remineralization rate integrated over the  $24^{\circ}\text{N}$ - $36^{\circ}\text{N}$  mid-latitude band exceed the new production rate. This imbalance means that an outside supply of organic matter is required. As particulate organic matter is remineralized immediately in the water column below the euphotic zone, the only possible source is from the transport of non-sinking organic matter into this latitude band. In latitude band  $24^{\circ}$ - $36^{\circ}\text{N}$ , more than half of the remineralization results from oxidation of DON (Figure 3.8). In the case of P3.7, it goes up to 70%. The high remineralization rate in this region is a combined result of oxidation of DON, both local and that transported from the north, and of PON falling from the euphotic zone above the water column. With more organic matter in the non-sinking and dissolved phase, as in the case of P3.7, the relative DON remineralization rate is greater.

At high latitudes, the new production rate is higher than remineralization rate. Since all PON is remineralized in the water column directly below where it is produced, and there must be a DON surplus, this DON could be carried southward by the Gulf Stream recirculation gyre before it can all be remineralized. The remineralization anomaly in a water column is defined as the residual of vertically integrated remineralization of total organic matter (PON and DON) in the aphotic zone, minus the vertically integrated new production in the euphotic zone. The horizontal distribution of this anomaly is shown in Figure 3.9. The positive value in the mid-latitude region ( $15^{\circ}$ - $45^{\circ}$ N) shows the remineralization exceeds the new production, and indicates that nitrate is formed from oxidation of DON which has been transported southward by the Gulf Stream recirculation gyre. The importance of DON in the nitrate budget are also pointed out by other modelling studies (Najjar et al., 1992; Bacastow and Maier-Reimer (1991).

The zonally and vertically integrated horizontal advection ( $V \cdot \nabla[\text{NO}_3]$ ) and diffusion ( $A_h \nabla^2[\text{NO}_3]$ ) are shown in Figure 3.10. These two terms are of the same order, and equally important in the total nutrient transport. Horizontal diffusion is greater than advection in the northern latitudes due to the presence of strong horizontal gradients, but weaker in the mid-latitude band of  $15^{\circ}$ - $35^{\circ}$ N due to the strong Gulf Stream transport.

The latitude range of  $15^{\circ}$ N to  $35^{\circ}$ N is selected to examine the new production rate in open ocean conditions. Using the Redfield ratio of Takahashi et al. (1985, N:C=16:103), the zonally averaged new production in this mid-latitude region are: 1.3, 1.0, 1.5, 1.1, 0.82 and 1.2 mol-C  $\text{m}^{-2} \text{yr}^{-1}$  for P3.5, P6.5, P3.7, E3.5, E6.5 and E3.6 respectively. These values are consistent with the Martin et al.'s (1987) estimate of 1.53

mol-C m<sup>2</sup> yr<sup>-1</sup> for the subtropics region of Pacific ocean, and are comparable with typical values for the oligotrophic ocean (Eppley and Peterson, 1979). The models result can also be used to obtain an estimate of the net new production. We obtain domain averaged new production rates in the range 2.3-3.6 mol-C m<sup>2</sup> yr<sup>-1</sup> (Table 3.2), which is higher than the estimate of Rintoul and Wunsch (1991) and comparable with the estimate of Najjar et al. (1992).

### 3.6 Summary

We have used a 3-dimensional planetary geostrophic ocean general circulation model and a simple biological model to examine nutrient cycling in an idealized Northern Atlantic basin. The northward transport of nitrate is divergent in the mid-latitude band (24<sup>o</sup>-36<sup>o</sup>N), and convergent north of that band. On the other hand, the flux of non-sinking and dissolved organic nitrogen is convergent in the mid-latitude band. The conversion of organic matter to inorganic matter within the mid-latitude band supplies the required source for the nitrate divergence. Most of the northward nitrate transport is located in the upper 1000 m of the western section of the basin, associated with the Gulf Stream flow.

The nitrate carried to the north by the Gulf Stream supports the high primary production in the northern section of the basin. There, new production exceeds remineralization. As the water flows back to the south in the Gulf Stream return flow, a significant fraction of non-sinking and dissolved organic matter is advected to the mid-latitude band. Remineralization (i.e., oxidation) of this non-sinking organic matter during

its transit of the subtropical gyre account for the large OUR observed by Jenkins and Goldman (1985).

Remineralization is larger than the new production in the mid-latitude water band between  $15^{\circ}$ - $35^{\circ}$ N. Remineralization of non-sinking and dissolved organic matter contributes at least half of the total remineralization in the band. This newly generated nitrate provides the source required to balance the northward transport of inorganic nutrient (nitrate) out of the mid-latitude band. The lateral transport and decomposition of non-sinking and dissolved organic matter is required to explain observations in open ocean regions (Martin et al., 1987). In the Atlantic, the subtropical gyre return flow is responsible for this transport. Zonally and vertically integrated horizontal advection and diffusion terms are equally important for total nutrient transport.

The model results are dependent on several adjustable parameters. The restoring timescale for nitrate in the surface layer ( $\tau$ ) is effectively the inverse of the rate of new production. Non-sinking and dissolved organic matter remineralization occurs at a rate proportional to the amount present. The inverse of the remineralization rate ( $\kappa$ ) of non-sinking and dissolved organic matter is effectively the turnover time of organic to inorganic matter. For example, for Experiment P3.5, the latter ranges from 4.1 years at a depth of 179 m to 254.1 years at 4000 m. The vertical diffusion coefficient ( $A_v$ ) does not vary with depth. More realistic parameterizations of these processes would require vertical and horizontal structure in some of these modelling parameters. However, more observations are required to identify such patterns before they can be used in large scale models.

Table 3.1 Parameter values for numerical simulations of the nitrate distribution in the North Atlantic.

Experiments	Dissolved fraction ( $\sigma_d$ )	PON remineralization formulation	Restoring time ( $\tau$ )
E3.5	0.5	Exponential, $z^*=800$ m	30 days
E6.5	0.5	Exponential, $z^*=800$ m	60 days
E3.6	0.6	Exponential, $z^*=800$ m	30 days
P3.5	0.5	Power law, $a=0.858$	30 days
P6.5	0.5	Power law, $a=0.858$	60 days
P3.7	0.7	Power law, $a=0.858$	30 days

Table 3.2 The upper panel shows the simulated meridional nutrient transport across 24°N and 36°N, and the new production rate. The latter is obtained using a N:C Redfield ratio of 16:103, with the rate in *Gt yr<sup>-1</sup>* shown in italics. Estimates from other observational and modelling studies are shown in the lower panel.

Experiments	Nitrate ( $\text{kmol s}^{-1}$ )		DON ( $\text{kmol s}^{-1}$ )		New production ( $\text{mol-C m}^{-2} \text{ yr}^{-1}$ ) ( <i>Gt yr<sup>-1</sup></i> )
	24°N	36°N	24°N	36°N	
E3.5	23.3	91.7	-33.8	-67.7	2.8 ( <i>11.6</i> )
E6.5	22.2	83.4	-30.5	-63.1	2.3 ( <i>9.5</i> )
E3.6	22.8	92.0	-32.4	-72.3	3.0 ( <i>12.5</i> )
P3.5	15.2	83.4	-17.8	-74.4	3.4 ( <i>14.1</i> )
P6.5	15.7	77.2	-31.1	-69.4	2.8 ( <i>11.6</i> )
P3.7	15.6	87.2	-26.4	-81.7	3.6 ( <i>14.9</i> )

Other studies:

(a) Nitrate flux

Rintoul & Wunsch(1991);

at 24°N,  $-8.0 \pm 39 \text{ kmol s}^{-1}$

at 36°N,  $119.0 \pm 35 \text{ kmol s}^{-1}$

(b) New production,  $\text{mol-C m}^{-2} \text{ yr}^{-1}$  (*Gt yr<sup>-1</sup>*)

Model simulation :

Najjar et al. (1992), 2.9 - 3.6 (*12.0 - 15.0 Gt yr<sup>-1</sup>*)

Observational studies estimate:

Jenkins & Goldman (1985), 4.0 (*16.6 Gt yr<sup>-1</sup>*)

Rintoul & Wunsch (1991), 2.1 (*9.0 Gt yr<sup>-1</sup>*)

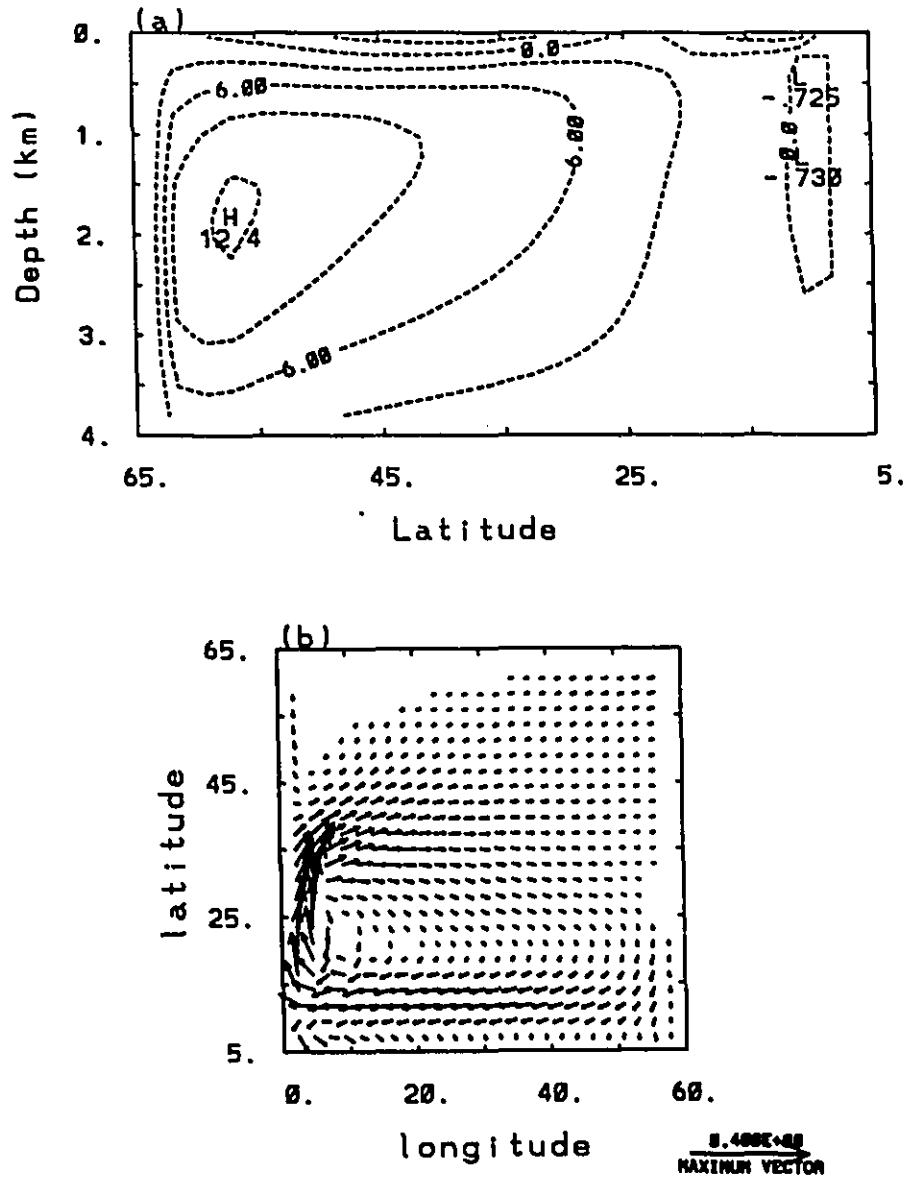


Figure 3.1 (a) The meridional overturning stream function ( $S_v$ ). (b) The horizontal circulation ( $\text{m s}^{-1}$ ) at a depth of 46 m. The fields of (a) and (b) are averaged over the last 100 years of a 2100 year integration, after an initial spin-up of 1200 years.

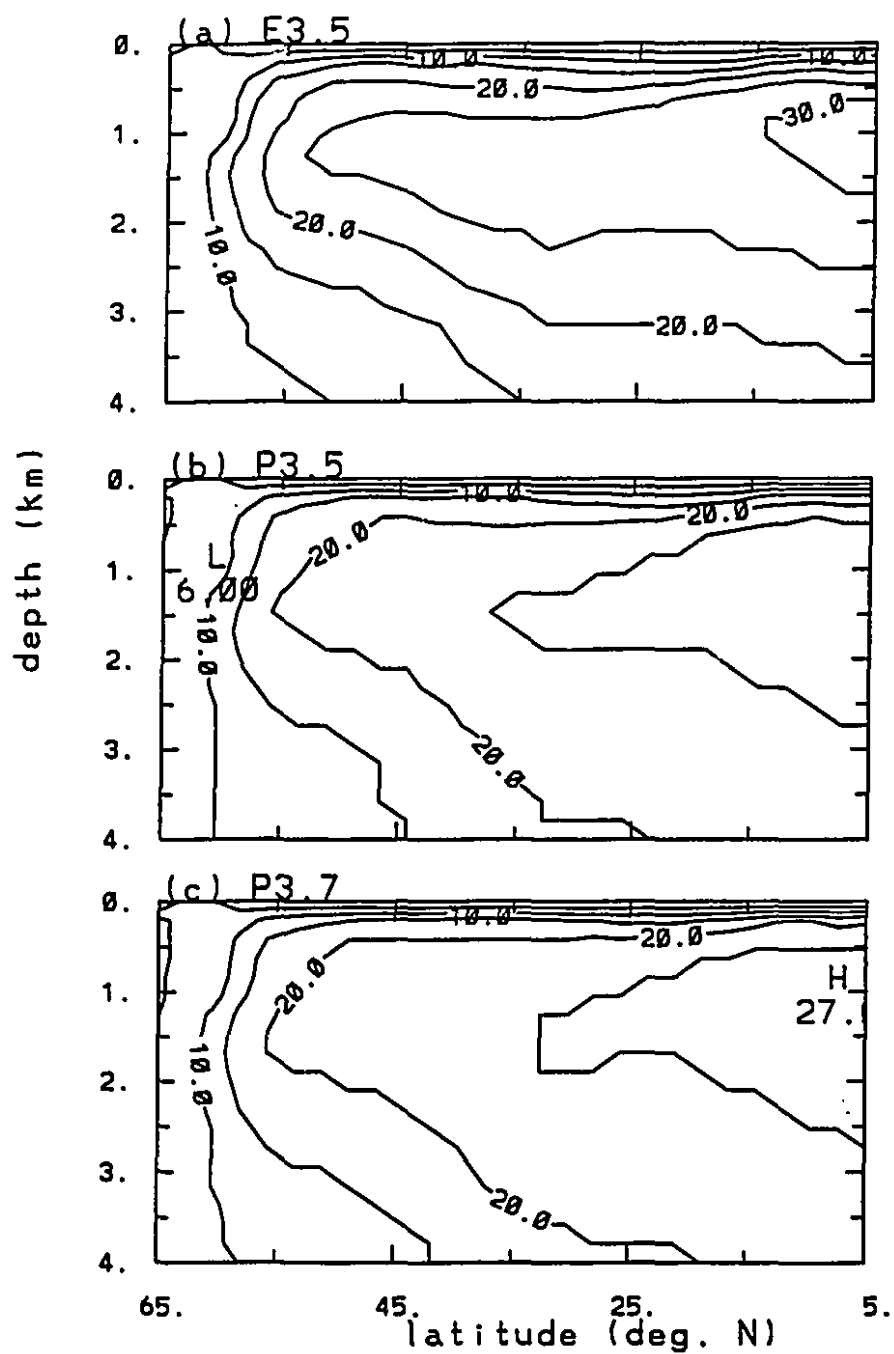


Figure 3.2 Meridional sections of the zonally averaged inorganic nitrate distribution ( $\text{mmol-N m}^{-3}$ ) for Experiments (a) E3.5, (b) P3.5, (c) P3.7.

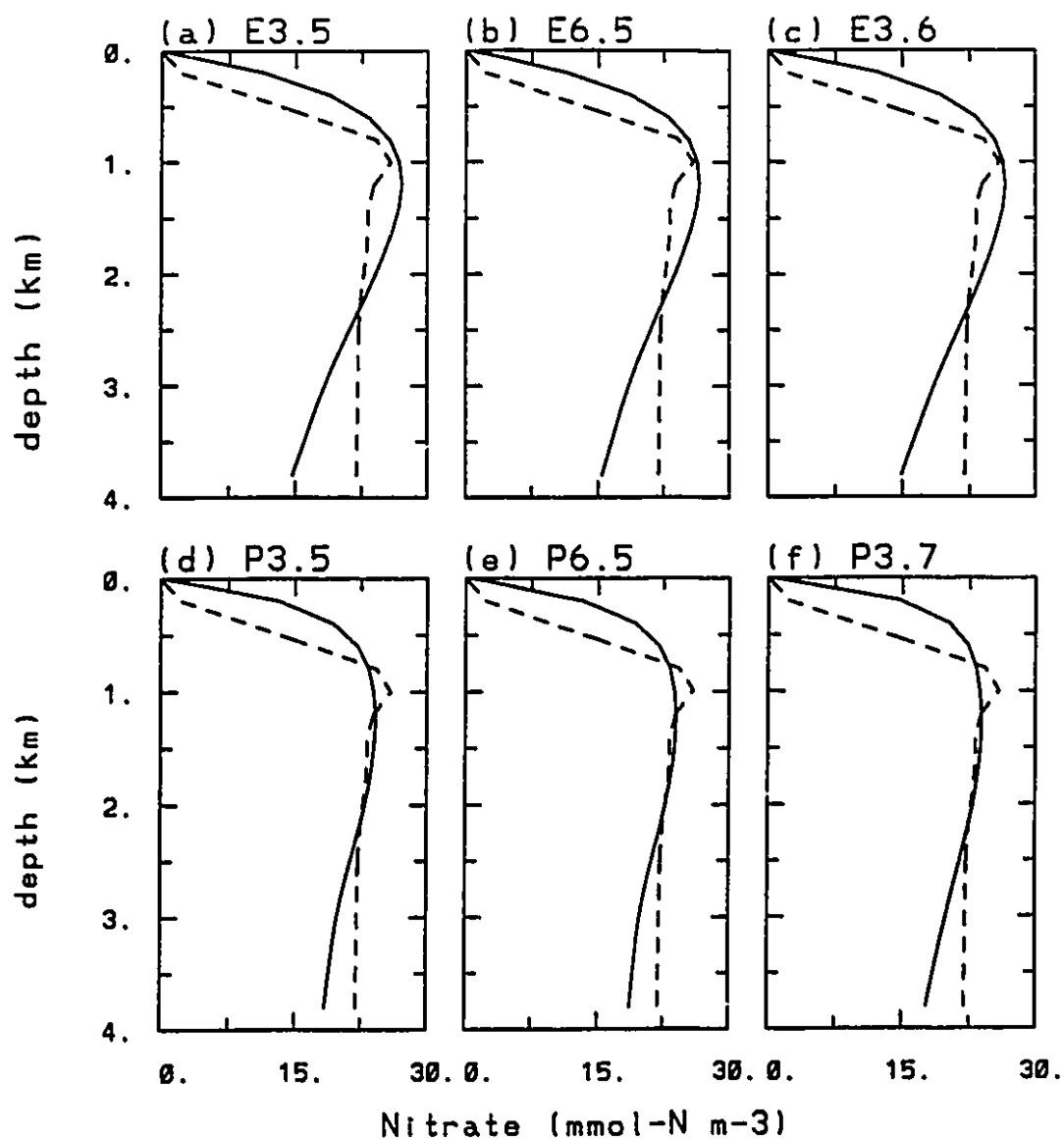


Figure 3.3 The basin averaged nitrate profiles for Experiments (a) E3.5, (b) E6.5, (c) E3.6, (d) P3.5, (e) P6.5 and (f) P3.7. The solid and dashed curves are from the model and observations (Broecker and Peng, 1982) respectively.

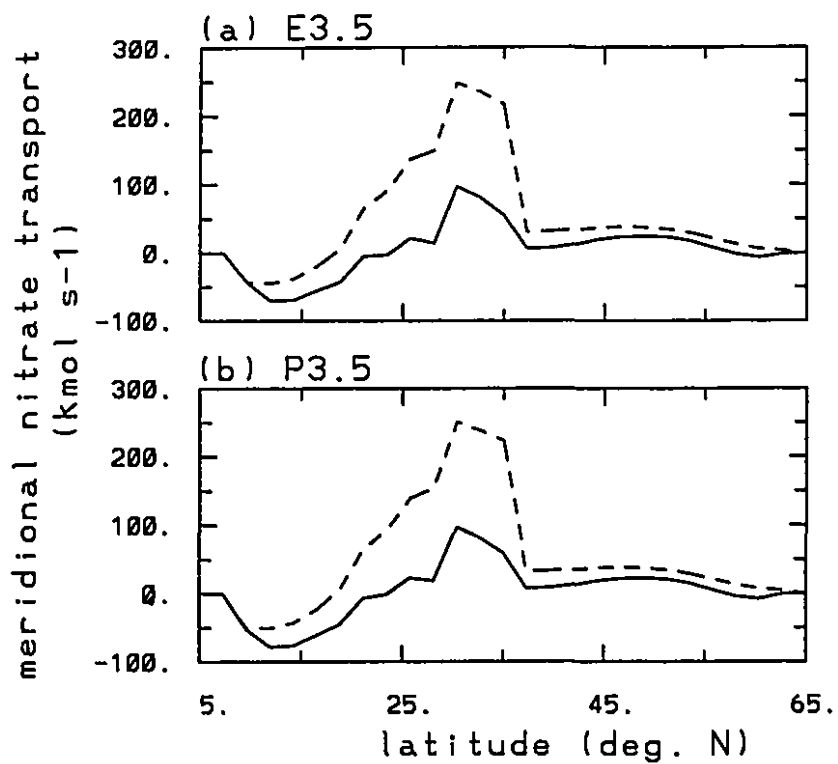


Figure 3. 4 Zonally and vertically integrated meridional nitrate transport (kmol s<sup>-1</sup>) for Experiments (a) E3.5, (b) P3.5. The dashed curves are the vertically integrated transport over the top 1000 m, while the solid curves are integrated over the depth of the ocean.

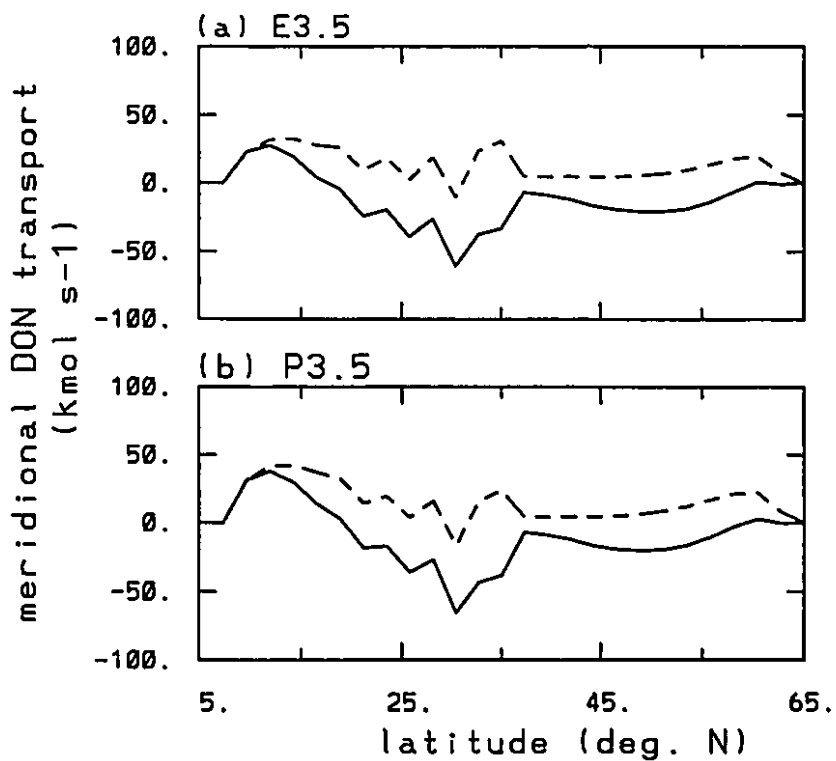


Figure 3.5 Zonally and vertically integrated meridional dissolved organic nitrogen transport ( $\text{kmol s}^{-1}$ ) for Experiments (a) E3.5, (b) P3.5. The dashed curves are the vertical integrated transport over the top 1000 m, while the solid curves are integrated over the depth of the ocean.

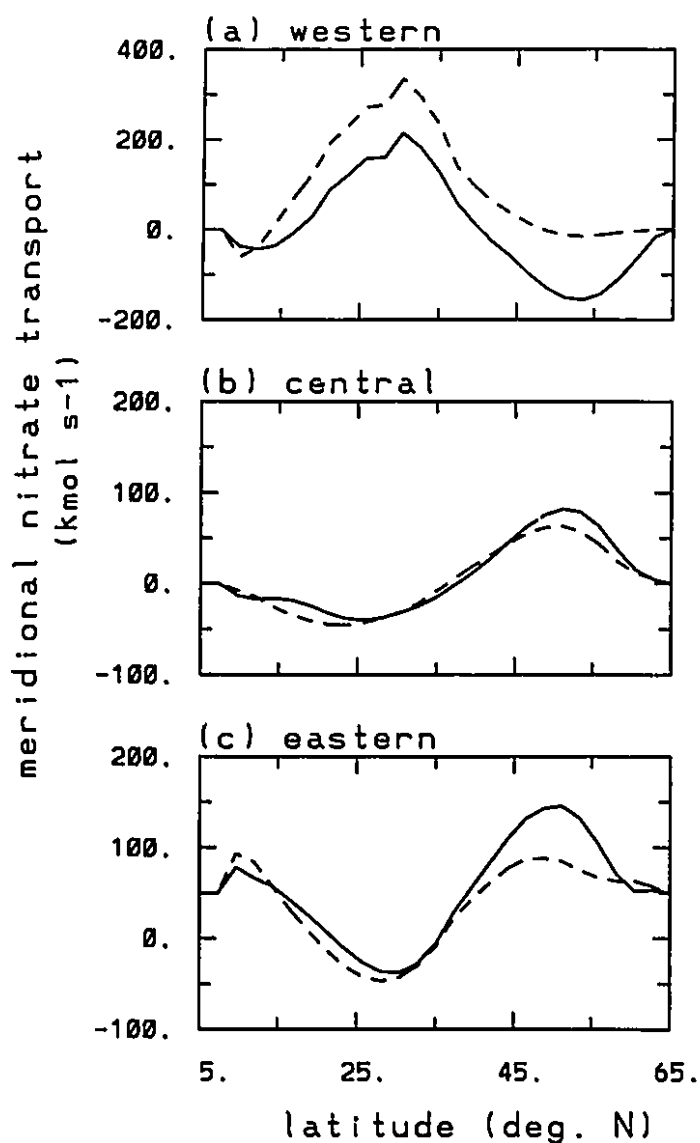


Figure 3. 6 Zonally and vertically integrated nitrate transport ( $\text{kmol s}^{-1}$ ) for Experiment P6.5 at the western ( $3^{\circ}$ - $17^{\circ}$  longitude), central ( $24^{\circ}$ - $38^{\circ}$  longitude), eastern ( $42^{\circ}$ - $56^{\circ}$  longitude) sections of the basin. The dashed curves are the vertically integrated transport over the top 1000 m, while the solid curves are integrated over the depth of the ocean. Notice the ordinate used in (a) is larger than in (b) and (c).

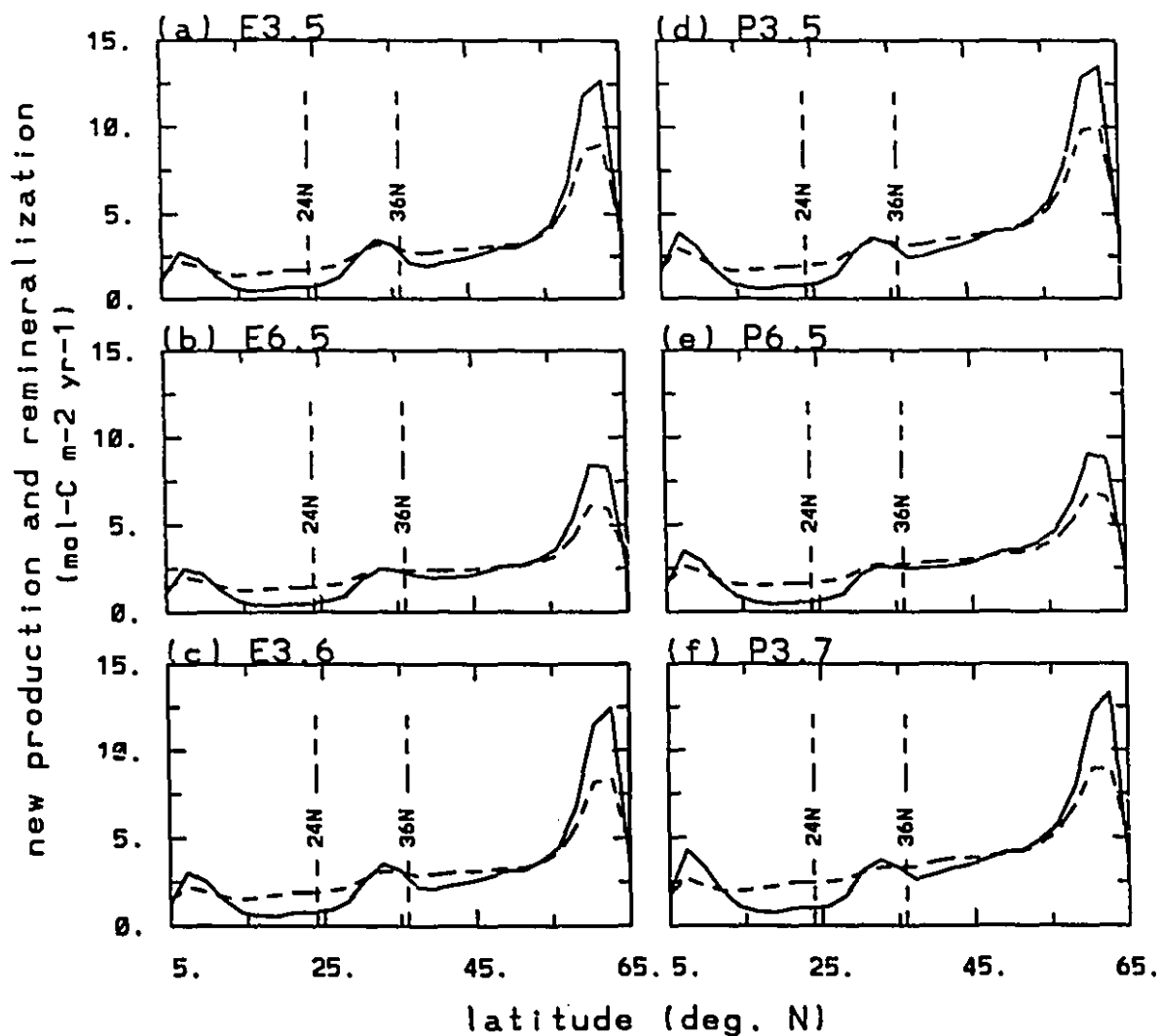


Figure 3. 7 Vertically integrated new production in the euphotic zone (solid line), and remineralization of total organic matter including both of PON and DON in the aphotic zone (dashed line) for Experiments (a) E3.5, (b) E6.5, (c) E3.6, (d) P3.5, (e) P6.5 and (f) P3.7. The unit is  $\text{mol-C m}^{-2} \text{ yr}^{-1}$ ; the Redfield ratio used is N:C=16:103. The vertical dashed lines indicate the  $24^{\circ}$ - $36^{\circ}$ N latitude band.

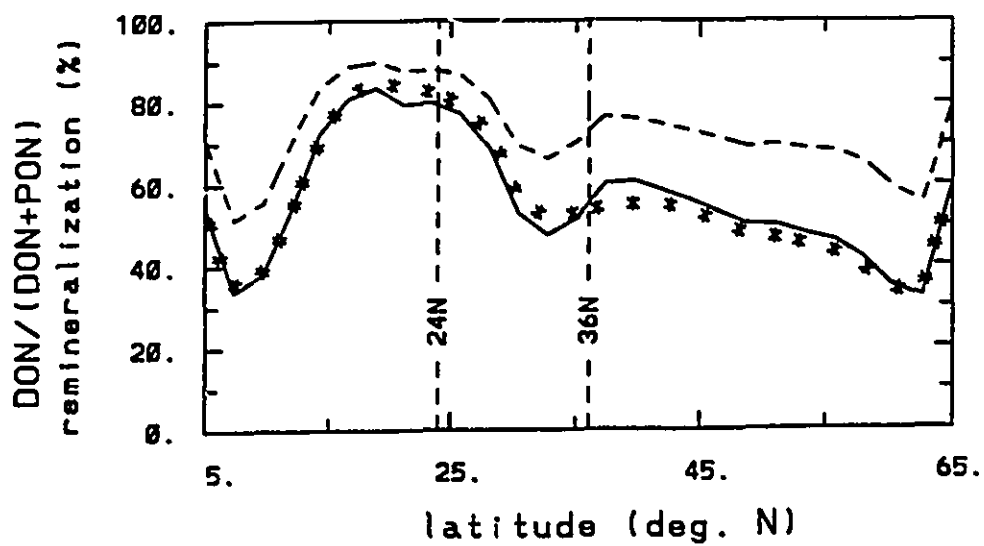


Figure 3. 8 Ratio in %, of the DON remineralization to the total DON and PON remineralization in the aphotic zone for Experiments P3.5 (solid), P6.5 (asterisk) and P3.7 (dashed). The vertical dashed lines indicate the 24<sup>0</sup>-36<sup>0</sup>N latitude band.

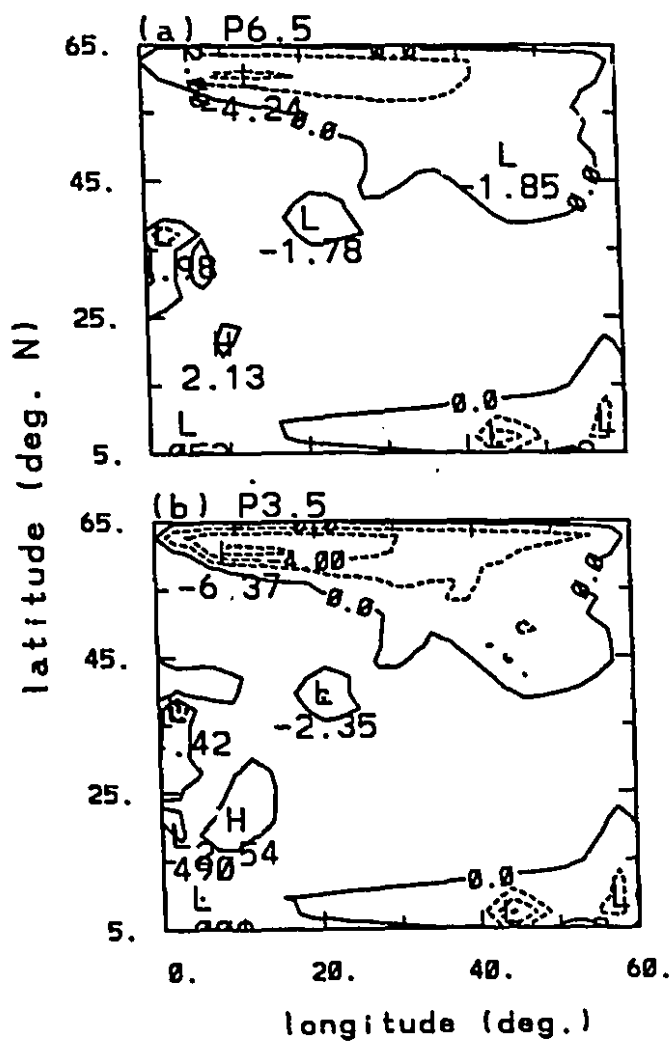


Figure 3.9 The horizontal distribution of remineralization anomaly (the negative values are in dashed line) for the Experiments (a) P6.5 and (b) P3.5. The vertical integration in aphotic zone is carried out from the base of euphotic zone to the bottom. The unit is  $\text{mol-C m}^{-2} \text{ yr}^{-1}$ .

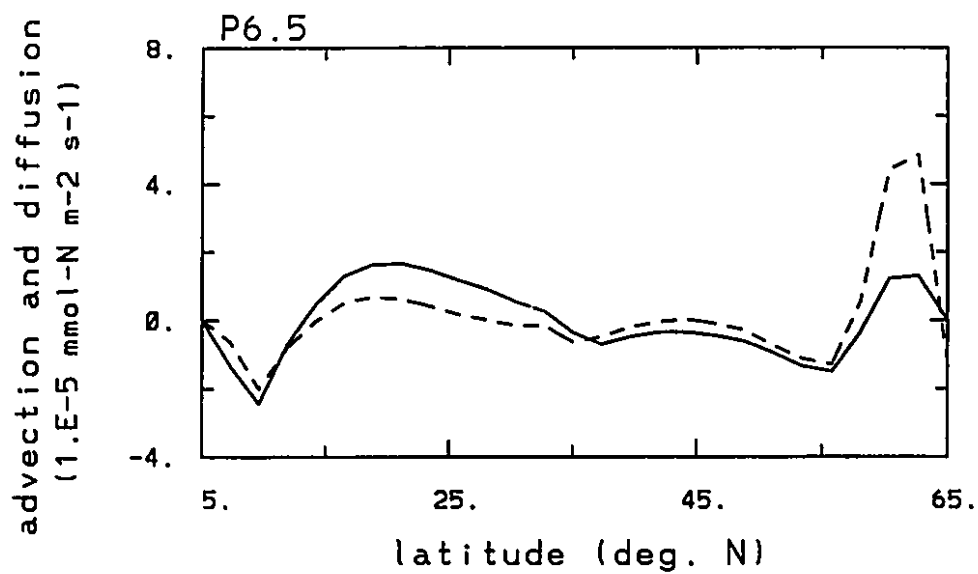


Figure 3.10 The zonally and vertically averaged horizontal advection ( $V \cdot \nabla[\text{NO}_3]$ , solid) and diffusion ( $A_h \nabla^2[\text{NO}_3]$ , dashed) terms for Experiment P6.5. The unit is  $10^{-5} \text{ mmol-N m}^{-2} \text{ s}^{-1}$ .

## **Chapter 4**

# **Modelling the seasonal cycle of oxygen in the North Atlantic Ocean**

### **4.1 Introduction**

The supersaturation of dissolved oxygen in the euphotic zone is observed over much of the open ocean during the stratified conditions of spring and summer (Reid, 1962; Shulenberger and Reid, 1981; Spitzer and Jenkins, 1989; Jenkins and Goldman, 1985). Jenkins and Goldman (1985) examined the long term hydrographic and dissolved oxygen record at the Panulirus site near Bermuda (Station S). Their results show the presence within the euphotic zone of a subsurface oxygen maximum of photosynthetic origin. Emerson (1987) reported on the seasonal cycles of oxygen, temperature and salinity at Ocean Weather Station P in the subarctic Pacific ocean, and found a regular 4-6% oxygen

supersaturation in the surface waters during the summers of the 10-year period 1969-1978. The supersaturation is due to the heating of the surface waters and the net effect of primary production and community respiration.

The oxygen content of the ocean depends on several factors: air-sea oxygen exchange, oxygen production and consumption rates by biological process, physical transport processes, temperature dependent solubility, and preformed surface oxygen concentration which is dependent primarily upon surface temperature. However, the relative importance of the different processes affecting oxygen accumulation in the euphotic zone is not easily determined from observations.

In chapter 3, we explored the annual nitrate cycle in the North Atlantic with a ocean circulation model coupled to a simple biological model. The role of Gulf Stream returning flow in nutrient transport was examined. Here, we use an extension of that model to assess the importance of biological and physical processes on oxygen production in the euphotic zone due to new production, and on oxygen utilization in the aphotic zone due to remineralization. To this end, we verify the physical model in the seasonal mode, and then we examine the seasonal oxygen variations. We also evaluate the relative importance of physical and biological processes in maintain oxygen supersaturation in the euphotic zone. The following section describes the model and experimental design; the seasonal cycle simulations are compared to observations and other modelling studies in section 4.3; the importance of the different processes is evaluated in section 4.4; and a summary is presented in section 4.5.

## 4.2 Model and experimental design

For the simulation of the seasonal oxygen cycle, we couple the physical model run in the seasonal mode, with the kinetic (as opposed to "restoring") biological model as described in Eq. (2.8) of Chapter 2. Recall in Eq. (2.8),  $H$  and  $R$  being constant and adjusted to give the best simulation compared to observations. Bacastow and Maier-Reimer (1991) used a kinetic model to simulate the flux of organic carbon associated with new production. They chose  $H=40 \text{ mmol-C m}^{-3}$ , equivalent to  $6 \text{ mmol-N m}^{-3}$ , using a Redfield ratio of  $N:C=16:103$  (Takahashi et al., 1985). The parameter  $R$ , which is a multiplier to obtain the new production (Eq. (2.7)), is then adjusted in such a way that the simulated nutrient field is closest to the observations. In our study, we take  $H=7 \text{ mmol-N m}^{-3}$ , and  $R$  is adjusted similarly as in Bacastow and Maier-Reimer (1991).

We have conducted 6 experiments; the experimental design is summarized in Table 4.1. All simulations include dissolved organic matter ( $\sigma_d > 0$ ). According to Najjar et al. (1992), observations of organic phosphorus fluxes as a fraction of new production suggest  $0.4 < \sigma_d < 0.8$ . Anderson (1993) and Anderson and Sarmiento (1994), using the model of Najjar et al. (1992) to study the time-mean, basin-wide Redfield ratio, suggest the value  $\sigma_d=0.5$  is a reasonable choice.

The nitrate and dissolved organic nitrogen distributions were initialized using typical depth profiles. The nitrate vertical profile was taken from Broecker and Peng (1982). For dissolved organic nitrogen, values in the top 900 m were taken from Jackson and Williams (1985), and below 900 m, held constant at the value at 900 m.

The physical model was first spun up for 1200 years with a timestep of 3 days, in order to obtain a statistically steady circulation. With the nutrient field included through the biological model, the coupled physical-biological model was run for another 2000 years. Convective adjustment takes place when there is static instability, and mixing of temperature and salinity in adjacent grid cells occur, leading to a stable profile. When convection occurs, the nutrient field is treated in the same way as the salinity field. Model diagnostics were constructed from averages during last 5 years of the simulation.

### **4.3 Seasonal cycle of oxygen**

The mass transport by the thermohaline circulation after 2000 years of simulation for the months of February and July in Experiment P5 are shown in Figure 4.1. Over the year, the maximum transport of 9.34 Sv is reached in October, and the minimum of 9.24 Sv in April, giving a seasonal variation of 0.1 Sv. This is comparable to the results obtained with other coarse resolution models in the North Atlantic (Bryan, 1979; Bryan and Lewis, 1979; Toggweiler et al., 1989a, b).

The simulated dissolved oxygen distribution is shown in Figure 4.2. Despite the somewhat idealized initial field, the simulated distribution is comparable to that observed (Fukumori et al., 1991, their Figures 42 and 48). Recall our model domain is of 60° longitudinal extent. We shall designate the mid-point of the zonal domain as being located at 30° longitude. We will examine the simulated fields at a mid-latitude (M) location at latitude 32°N and longitude 30°, as well as at a high latitude (H) point at

latitude 50°N and longitude 30°. Figures 4.3 and 4.4 show the seasonal cycles of temperature and density for Experiments P5 and G5 respectively. In the northern latitude band between 50° and 60°N in the late winter season (February-May) (Figure 4.3, Figure 4.4), strong vertical mixing draws down surface waters to the deep ocean. With the establishment of the seasonal thermocline in May, the top 400 m becomes stratified and vertical mixing is suppressed. The model simulated nitrate distribution (not shown) also agrees quite well with observations (Figures 45 and 51 of Fukumori et al. (1991)). The same experiments were also conducted using the restoring biological model; the results are almost identical to those obtained using the kinetic biological model.

Jenkins and Goldman (1935) showed that throughout the 1960s at Station S, the isopycnal surface  $\sigma=26.2$  deepened to 100 or 150 m in September-February, followed by shoaling and occasionally surfacing in late winter months of February and March. However, beginning in 1972, this isopycnal surface deepened persistently to about 200 m in 1976, and did not shoal above 100 m until the winter of 1977-1978.

The temperature and density fields at the mid-latitude (M) and high latitude points (H) throughout the year from Experiment P5 are shown in Figure 4.3. The annual cycle of the seasonal thermocline formation and destruction is clearly evident. The high latitude density field is characterized by the appearance and subsequent disappearance of the  $\sigma=25.8$  isopycnal surface. Stratification begins in spring (April-May) and intensifies until late summer (August-September), after which erosion of the thermocline is seen in the rapid outcropping and subsequent disappearance of many of the isopycnals. Extensive vertical mixing occurs in the late winter (February-May). At the mid-latitude location,

a characteristic isopycnal surface is  $\sigma=25.0$ .

In the high latitudes, the seasonal cycle of the simulated temperature and density fields is similar to that observed at the Ocean Weather Station India, and is in agreement with the model results of Fasham et al. (1993). The simulated temperature field is also comparable with observations at Station P, and is consistent with 1-dimensional model simulations (Emerson, 1987; Thomas et al., 1990; Archer et al., 1993). In the mid latitudes, the simulated seasonal thermocline is consistent with that observed at Station S in the Sargasso Sea (Jenkins and Goldman, 1985) and model simulations (Spitzer and Jenkins, 1989; Fasham et al., 1993; Price et al., 1986; Mellor and Yamada, 1974, 1982; Gaspar, 1988; Gaspar et al., 1990).

Experiment G5 is identical to P5, except for an increase in the vertical diffusivity from  $0.63$  to  $0.83 \text{ cm}^2 \text{ s}^{-1}$ . In this case, there is little variation of the mass transport by the thermohaline circulation, being about  $11.4 \text{ Sv}$  for each month. The increase in the magnitude of the transport is expected, as it is known to increase with the vertical diffusivity (Bryan, 1987). Figure 4.4 shows the temperature and density fields of Experiment G5 at the mid and high latitude locations. With stronger vertical diffusion, the seasonal thermocline signal is weaker than in Experiment P5. For example, the  $\sigma=25.0$  isopycnal surface of Figure 4.4(b) does not surface during the year, in contrast to Figure 4.3(b). Most of the result of this section are obtained with lower vertical diffusivity, in order to have a stronger seasonal signal.

We now turn to the simulation of the oxygen seasonal cycle. The monthly evolution of the oxygen super-saturation at the mid (M) and high (H) latitude locations

of Experiment P5 are shown in Figure 4.5. Oxygen begins to accumulate in the euphotic zone in early spring, reaching a maximum just above 100 m in late summer in the presence of stratification. The maximum erodes gradually, and mixing erases it completely in late winter. At the surface, the effect of forced gas exchange is seen in the appearance of the zero isoline from May through November (Figure 4.5(b)).

In late winter, strong vertical mixing brings up more nitrate to the euphotic zone, increasing new production. The oxygen so produced is not accumulated in the euphotic zone, but is transported downward to deeper layers, where the local oxygen concentration is under-saturated. This newly generated oxygen compensates for the oxygen deficiency in the deeper layers. This is seen in Figure 4.5(c) and Figure 4.5(d), where the zero super-saturation isoline comes to surface during the winter months of February to April. The mixing of severely oxygen under-saturated water from the aphotic zone with slightly oxygen super-saturated water from the euphotic zone produces oxygen under-saturated water in the euphotic zone from February to April. This occurs despite the production of oxygen by photosynthesis in the euphotic zone throughout the whole year.

The maximum oxygen super-saturation in the euphotic zone is located at a depth of about 75 and 80 m in the mid and high latitude locations respectively (Figure 4.5(a) and Figure 4.5(c)). The mid-latitude maximum is located in oligotrophic waters, giving a low oxygen accumulation maximum of  $0.24 \text{ ml l}^{-1}$  (Figure 4.5(a)), and the percentage of supersaturation is 3.6% (Figure 4.5(b)). At Station S in the Sargasso Sea ( $32^{\circ}\text{N}$ ,  $64^{\circ}\text{W}$ ), the average seasonal oxygen anomaly during the period 1961-1970 corresponds to an average super-saturation of  $0.4 \text{ ml l}^{-1}$  (Jenkins and Goldman, 1985), and the

percentage of supersaturation is about 6-8% for the same period (Musgrave et al., 1988). The high latitude maximum is larger, reaching a value of  $0.67 \text{ ml l}^{-1}$  (Figure 4.5(c)), the percentage of supersaturation is 8.2% (Figure 4.5(d)). At Station P in the North Pacific ( $50^{\circ}\text{N}$ ,  $145^{\circ}\text{W}$ ), oxygen supersaturation is maintained in the mixed layer during the summer months of May to August with a maximum about 10% ( $\sim 0.8 \text{ ml l}^{-1}$ ) in August (Emerson, 1987). As the mixed layer deepens during the period of surface cooling from September to December, the oxygen concentrations return to vertically uniform values, and the degree of supersaturation drops.

Thomas et al. (1990) simulated the oxygen supersaturation at Station P, using a 1-dimensional integral mixed layer model. Their results show a 8-10% oxygen supersaturation at a depth of 50 m (their Figure 4.5), somewhat higher than observations. In a later study, Thomas et al. (1993) obtained good agreement of the modelled and observed seasonal cycles of monthly mean surface dissolved oxygen values, using an eddy kinetic energy (EKE) model. By adjusting the production function, the EKE model can better simulate both the seasonal and short time evolution of the oxygen concentration, when compared with the integral model.

At the high latitude location, the simulated oxygen supersaturation and percentage of supersaturation (Figures 4.5(c) and 4.5(d)) are comparable with those of 1-dimensional models (e.g. Thomas et al., 1993). However, in the mid-latitude location, our results (Figures 4.5(a) and 4.5(b)) are lower than observed values; Spitzer and Jenkins (1989) reported a 10% oxygen super-saturation at Bermuda for the period 1985-1986. However, we note that our model is designed for long term climate simulations, and the results may

not be applicable to rapid changes.

#### 4.4 Oxygen flux

Emerson (1987) interpreted oxygen data at Station P from 1969-79 using a simple quasi-steady state model of mixed layer heating, gas exchange, and net biological oxygen production. It was assumed that the latter was stoichiometrically related to the net carbon export, giving a carbon flux of 100-300 mg-C m<sup>-2</sup> day<sup>-1</sup>. For the same station, the estimated biologically produced oxygen flux during the summer months of 1987-1988 was 13-17 mmol-O<sub>2</sub> m<sup>-2</sup> day<sup>-1</sup> (Emerson et al., 1991). Quay et al. (1993) studied the <sup>18</sup>O/<sup>16</sup>O ratio of dissolved oxygen measured in the upper subarctic Pacific ocean in 1988. Using the method of mixed layer oxygen budget analysis, they reported a rate of net biological oxygen production (new production) of 16 (range from 4 to 36), and 9 (range from 3 to 18) mmol-O<sub>2</sub> m<sup>-2</sup> day<sup>-1</sup> for Stations P and R respectively. These values are within the range of 7-23 mmol-O<sub>2</sub> m<sup>-2</sup> day<sup>-1</sup> integrated over the 0-100 m layer for the summers of 1987 and 1988 (Emerson et al., 1991).

At Station S in the Sargasse Sea, Jenkins and Goldman (1985) estimated the vertically integrated oxygen production rate to be of the order of 5 mol-O<sub>2</sub> m<sup>-2</sup> yr<sup>-1</sup> during the 1960-70 period, by considering insolation, heat budget and available <sup>3</sup>He/<sup>3</sup>H data. This is equivalent to 13.7 mmol-O<sub>2</sub> m<sup>-2</sup> day<sup>-1</sup>. The observed seasonal cycles of temperature, argon, helium and oxygen during 1985-86 were simulated using an upper ocean model by Spitzer and Jenkins (1989). They obtained a lower limit to the depth-

integrated new production below the mixed layer of  $4.3 \pm 1.7 \text{ mol-O}_2 \text{ m}^{-2} \text{ yr}^{-1}$  ( $11.8 \pm 4.7 \text{ mmol-O}_2 \text{ m}^{-2} \text{ day}^{-1}$ ) during 1985. New production within the mixed layer remained unconstrained because the mixed layer concentrations are mainly controlled by gas exchange with the atmosphere.

The monthly oxygen production rates (new production) at the mid (M) and high (H) latitude locations are shown in Table 4.2. The average production rates for the year for these two locations are 7.7 and 25.7  $\text{mmol-O}_2 \text{ m}^{-2} \text{ day}^{-1}$  respectively; these values are consistent with observations (Emerson et al., 1991, 1993; Quay et al., 1993). In the high latitude location, oxygen production peaks during March-June, due to enhanced late winter vertical mixing which introduces a large nutrient flux into the sunlit surface layers, supporting high productivity in the northern part of the basin. Sarmiento et al. (1993) showed that nitrate uptake fuels the early part of the phytoplankton bloom. Later, an increase in ammonium concentration leads to a subsequent inhibition of the nitrate uptake, replacing it by uptake of ammonium.

Figure 4.6 shows a latitude-time plot of the oxygen production rate, vertically integrated through the euphotic zone. The simulated high production rates in the northern basin during March-June are similar to those observed in the northern north Atlantic ocean. This high productivity region can be observed along the axis of the North Atlantic Current in satellite images of ocean colour (Esaias et al., 1986). We estimate the oxygen production rate in Experiment P5 as  $5.11 \text{ mol-O}_2 \text{ m}^{-2} \text{ yr}^{-1}$ , which is equivalent to a new production of  $41 \text{ g-C m}^{-2} \text{ yr}^{-1}$ . By considering the oxygen cycling at depth, Jenkins and Goldman (1985) estimated an oxygen consumption rate between 4.1 and  $5.9 \text{ mol-O}_2 \text{ m}^{-2}$

$\text{yr}^{-1}$ , depending on the data extrapolation to the larger depths. This yields a new production of 40 to 50  $\text{g-C m}^{-2} \text{yr}^{-1}$ , which is consistent with earlier estimates.

We now examine the air-sea oxygen flux. Quay et al. (1993) and Emerson et al. (1993) reported the gas evasion rates during summer time at the subarctic Pacific Stations P and R are respectively 42 (range from 19 to 57) and 24 (range from 5 to 38)  $\text{mmol-O}_2 \text{m}^{-2} \text{day}^{-1}$ . Gas evasion was found to be the dominant mechanism for maintaining the oxygen flux, causing the mixed layer oxygen concentration to decrease by 20 and 11  $\text{mmol-O}_2 \text{m}^{-2} \text{day}^{-1}$  for Stations P and R respectively.

The monthly oxygen flux to the atmosphere at locations M and H for our model experiment P5 is shown in Figure 4.7. These values are consistent with observational studies (Quay et al., 1993; Emerson et al., 1993). Jenkins and Goldman (1985) calculated the oxygen flux at Station S in the Sargasso Sea, using data from 1960-70. The integrated oxygen flux to the atmosphere from March through January is  $6.9 \text{ mol-O}_2 \text{ m}^{-2} \text{ yr}^{-1}$  ( $18.9 \text{ mmol O}_2 \text{ m}^{-2} \text{ day}^{-1}$ ). Two prominent features of the observed flux are the presence of two maxima in spring and fall, and the negative excursion during late winter. This behaviour is also found in our results (Figure 4.7). The spring maximum is consistent with high levels of photosynthesis. The autumn maximum is however enhanced by the deepening of the mixed layer, and hence results in part from the subsequent unloading of the photosynthetic oxygen sequestered at depth through the summer as well as enhanced productivity due to nutrient injection. It is important to note that these maxima result from the interaction between changing oxygen concentration and vertical exchange velocity. However, they are also consistent with both the known

biological cycling and the observed changes in water column oxygen inventories.

We close this section with a discussion of remineralization. Remineralization is often expressed in term of the equivalent amount of oxygen consumed, oxygen utilization rate (OUR). The biological oxygen production is related to nitrate uptake through Redfield ratio. At steady state over the annual cycle, in the absence of nitrification and heterotrophic  $\text{NO}_3$  uptake by bacteria (Kirchman et al., 1991), this production should equal the oxygen consumption. The OUR can thus be used to estimate the new production in the euphotic zone. The OUR itself can in turn be estimated in two ways. The first is process oriented, and accounts for the respiration due to specific processes such as bacterial activity (Packard et al., 1988; Cho and Azam, 1988) or the breakdown of large particles (Martin et al., 1987). The second approach uses advection-diffusion models (Volk and Hoffert, 1985).

Based on the high temperature catalytic oxidation (HTCO) method, Sugimura and Suzuki (1988) suggested that the concentration of DOC in the ocean was 200 to 400% higher than that estimated using older methods. Further evaluation of the analytic methodology (e.g., Sharp, 1993) found that the older analytical methods appear to be able to measure all of the DOC measured by HTCO methods. However with most current methods, fine details can be seen in the DOC distribution which were not available in the past. Carlson et al. (1994) showed that there are significant changes in DOC concentrations over short temporal and spatial scales. They also suggested that beside the traditional refractory and the very labile portion, a third pool, termed "semi-labile" would appear to have turnover times of many months to a few years. This pool is critical in the

carbon flux from areas of production to subsurface waters, and laterally away from these sites. The refractory pool has a turnover time on the order of ocean mixing cycles (hundred years) while the very labile pool has turnover times on hours to a day.

Comparing the OUR vertical profile in Experiments P7, P5 and P2 (Figure 4.8). We see the OUR in Experiment P2 changes proportionally the most with depth. The power law is used to parameterize the downward transport of particulate organic matter, with an equivalent e-folding depths of 200-300 m. On the other hand, the DOM remineralization is parameterized according to Eq. (2.14) (Cho and Azam, 1988), with an e-folding depth of 750 m. Remineralization of particulate matter is parameterized as an instantaneous process. In Experiment P2, 80% of the total newly formed organic matter exists in the form of sinking particulate matter, which falls through the water column. At a depth of 600 m, the calculated sinking particulate flux from Eq. (2.11) is about 24% of the flux at the bottom of euphotic zone, and the rest of the sinking particulate organic matter is remineralized between 114-600 m. The combined effects of the shallow remineralization scale and simultaneous remineralization result in most of the vertically sinking particulate organic matter being utilized just beneath the euphotic zone, with a steep remineralization gradient. If particulate organic matter is less dominant in the downward transport, as in Experiments P7 and P5, the decrease of the OUR signal with depth is less pronounced. The gradient of remineralization of dissolved organic matter below the euphotic zone is not as steep as that for particulate matter, a result which is consistent with the findings of Harrison (1992). The latter noted that remineralization of particulate matter decreases with depth, with a steeper gradient than for dissolved organic

carbon and nitrogen.

Experiments PK3 and PK1 are identical with Experiment P5, except that in PK3, DOM remineralization is parameterized according to Eq. (2.14), but with an e-folding depth of 300 m; in PK1, the DOM remineralization rate ( $\kappa$ ) is constant with depth. Comparison of Experiments P5 and PK3 shows that the shallow remineralization depth results in that most of remineralization taking place in the upper 600 m. The gradient of OUR signal is thus much steeper in PK3 than in the other experiments. The OUR gradient for PK1 is not as steep as in other experiments, as the use of a constant of remineralization rate implies a longer turnover time, and thus some of the DOM is transported to deeper layers.

The DOM turnover time is much shorter at shallow depths than in the deep layers. The reciprocal of the remineralization rate ( $\kappa^{-1}$ ) is effectively the turnover time of organic matter to inorganic matter. Observations suggest that the dissolved organic matter remaining at greater depth is refractory (e.g., Carlson et al., 1994; Packard et al., 1988; Cho and Azam, 1988; Jackson and Williams, 1985). The turnover time in Experiment P5 ranges from 3.2 years at a depth of 179 m to 221.4 years at 4000 m. However in Experiment PK1, the use of a constant remineralization rate results in a uniform turnover time of 108 years. The exponential parameterization of DOM remineralization is an approximation, and a proper e-folding depth is essential for modelling studies involving remineralization. To examine the sensitivity to the parameter dependence, the constant  $\kappa$  of Experiment PK1 and the 300 m e-folding depth of PK3 were chosen as extreme case; our result show that the OUR vertical profile depends on the detail of the DOM

rem mineralization parameterization.

Table 4.3 shows the monthly variation of the vertically integrated of OUR signal in the deep layers (600-4000 m) as a percentage fraction of the integrated signal over the aphotic zone (114-4000 m). In the annual mean, this ratio is 38.7%, 40.4% and 33.1% in Experiments P5, P7 and P2 respectively. The deep layers in Experiment P7 thus received proportionally more organic matter than in Experiments P2. In Experiment PK1, the slow turnover time as a result of the use of a constant  $\kappa$  results in more DOM being transported by the oceanic circulation to the deep layers prior to remineralization.

The result of our experiments suggest that the vertical OUR profile is sensitive to the downward transport mechanism. When particulate matter is dominant with a shallow remineralization scale, remineralization takes place just below the euphotic zone, and OUR decreases rapidly with depth. On the other hand, when dissolved matter is dominant, OUR decreases less rapidly with depth, as a fraction of the dissolved matter can now be transported to deeper layers. The vertically integrated OUR signal is  $5.1 \text{ mol-O}_2 \text{ m}^{-2} \text{ yr}^{-1}$  ( $3.1 \text{ mol-C m}^{-2} \text{ yr}^{-1}$ ),  $5.2 \text{ mol-O}_2 \text{ m}^{-2} \text{ yr}^{-1}$  ( $3.2 \text{ mol-C m}^{-2} \text{ yr}^{-1}$ ),  $5.2 \text{ mol-O}_2 \text{ m}^{-2} \text{ yr}^{-1}$  ( $3.1 \text{ mol-C m}^{-2} \text{ yr}^{-1}$ ),  $3.8 \text{ mol-O}_2 \text{ m}^{-2} \text{ yr}^{-1}$  ( $2.3 \text{ mol-C m}^{-2} \text{ yr}^{-1}$ ), and  $6.3 \text{ mol-O}_2 \text{ m}^{-2} \text{ yr}^{-1}$  ( $3.9 \text{ mol-C m}^{-2} \text{ yr}^{-1}$ ) for Experiments P5, P7, P2, PK1 and PK3 respectively. Using Jenkins and Goldman's (1985) data set and a 1-dimensional ocean model, Musgrave et al. (1988) estimated the OUR signal at a site in the subtropical North Atlantic to be about  $3\text{-}4 \text{ mol-O}_2 \text{ m}^{-2} \text{ yr}^{-1}$ , which is at the low end of the range of our simulated values.

## 4.5 Summary

The observed seasonal cycle of oxygen supersaturation within the euphotic zone is successfully reproduced by coupling a physical and a biological model. Approximately the right order of supersaturation is obtained; the supersaturation in the euphotic zone is mainly caused by photosynthetic processes, and is modulated by the seasonal cycle.

The simulated oxygen production rate is consistent with observational studies and other model results. The simulated oxygen flux to the atmosphere agrees qualitatively with observational studies, and this flux is comparable to the oxygen flux from biological production processes in the euphotic zone. During late winter (February-April) in the northern part of the model domain, strong convective mixing brings up nutrients to the euphotic zone, resulting in high new production. The oxygen produced during this photosynthetic process does not remain in the euphotic zone, but is physically transported downward to the aphotic zone, where it reduces the deep water oxygen deficiency.

The simulated OUR vertical profile is sensitive to the downward transport mechanism, and to the parameterization of remineralization of dissolved and particulate organic matter. When particulate matter dominates, remineralization occurs at shallow depths, and the OUR profile decreases rapidly with depth. When dissolved matter dominates, remineralization takes place at greater depths and OUR does not decrease as rapidly with depth. This sensitivity can be important in the interpretation of observational data.

The results from our model are comparable with the long term observations of

Jenkins and Goldman (1985). Since our physical model does not have a mixed layer, the surface temperature and salinity fields are restored to monthly climatological values on a time scale of 30 days. Hence pulse-like events which are important for the oxygen accumulation in the surface layer cannot be simulated. Our results are thus representative of longer term changes.

Table 4.1 Parameter values for the different experiments.  $\sigma_d$  is the fraction of new production used to generate dissolved nitrogen, with the remainder ( $1-\sigma_d$ ) being put into sinking particulate organic nitrogen.  $A_v$  is the vertical diffusivity.  $z'$  is e-folding depth scale of remineralization rate ( $\kappa$ ) of non-sinking and dissolved organic nitrogen (Eq. (2.14)), except in Experiment PK1, where a constant  $\kappa$  is assumed.

Experiment	$\sigma_d$	$z'$	$A_v$
P5	0.5	750 m	0.63 cm <sup>2</sup> s <sup>-1</sup>
P2	0.2	750	0.63
P7	0.7	750	0.63
G5	0.5	750	0.83
PK1	0.5	-	0.63
PK3	0.5	300	0.63

Table 4.2 The oxygen production rate as a result of new production of Experiment P5 at the mid (M) and high (H) latitude locations, in unit of  $\text{mmol-O}_2 \text{ m}^{-2} \text{ day}^{-1}$ . A Redfield ratio is used to convert nitrate to oxygen production.

Month	Location M	Location H
1	7.56	4.50
2	7.59	5.82
3	7.64	64.93
4	7.83	121.90
5	7.76	61.35
6	7.80	20.70
7	7.77	7.14
8	7.78	4.73
9	7.75	4.33
10	7.67	4.26
11	7.67	4.34
12	7.64	4.41
Mean	7.71	25.70

Table 4.3 The vertically integrated OUR signal of the deep ocean (600-4000 m) as a percentage fraction of that of the aphotic zone (114-4000 m), for Experiments P7, P5, P2, PK1, and PK3.

Month	P7	P5	P2	PK1	PK3
1	40.6	39.0	33.4	53.9	25.9
2	39.5	37.6	32.3	50.6	25.5
3	39.7	37.7	32.3	50.7	25.5
4	39.7	37.8	32.4	51.0	25.4
5	39.8	37.8	32.3	50.8	25.7
6	40.1	38.0	32.4	51.3	26.1
7	40.5	38.6	32.8	52.8	26.2
8	40.9	39.3	33.4	54.2	26.2
9	41.1	39.6	33.7	54.8	26.2
10	41.1	39.6	33.8	54.9	26.1
11	41.1	39.6	33.8	54.9	26.1
12	41.1	39.6	33.8	54.9	26.0
Mean	40.4	38.7	33.1	52.0	26.0

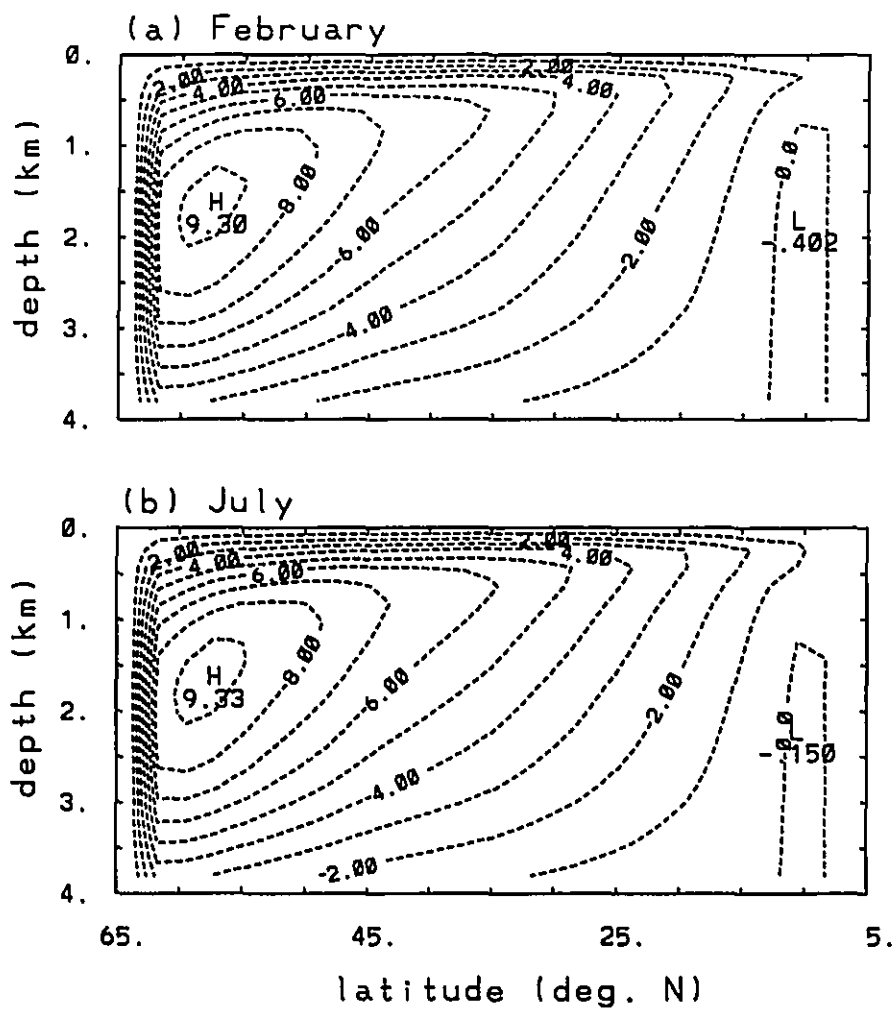


Figure 4.1 The magnitude of the thermohaline circulation (Sv) after 2000 years of model simulation of Experiment P5, for (a) February, and (b) July.

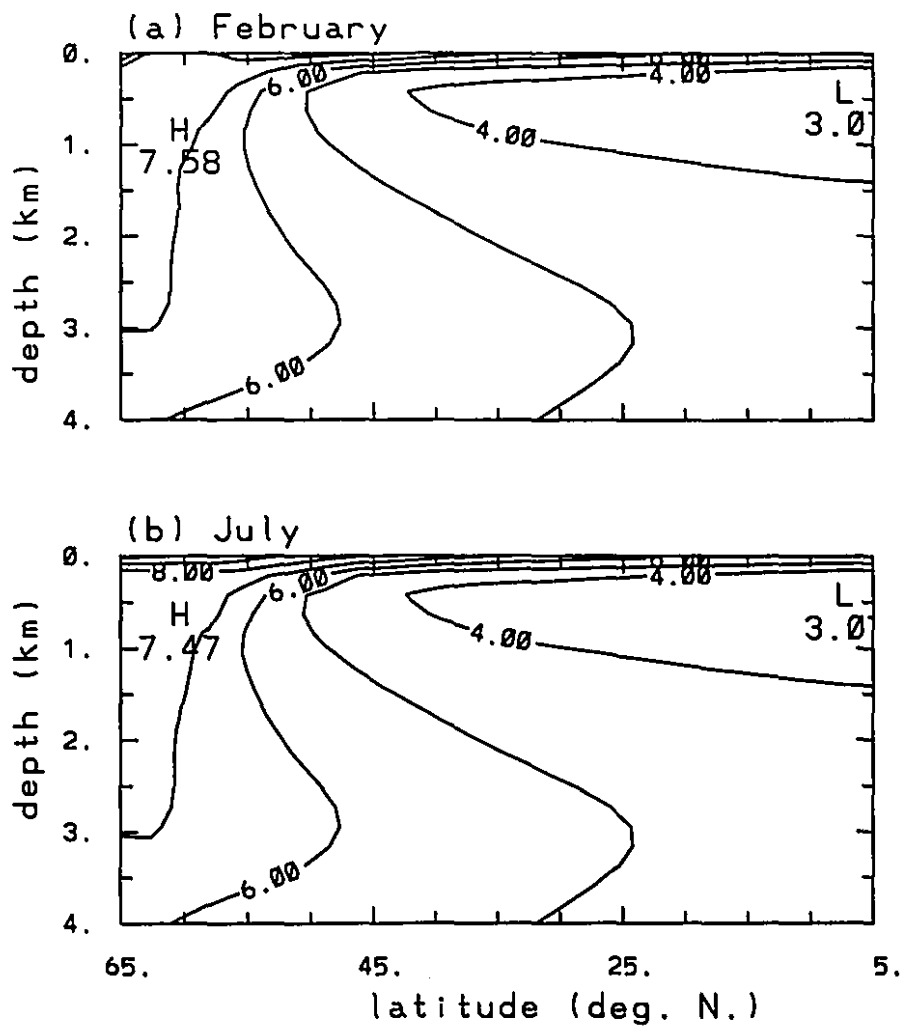


Figure 4.2 Meridional section of zonal averaged dissolved oxygen distribution ( $\text{ml l}^{-1}$ ) for Experiment P5 for (a) February, and (b) July.

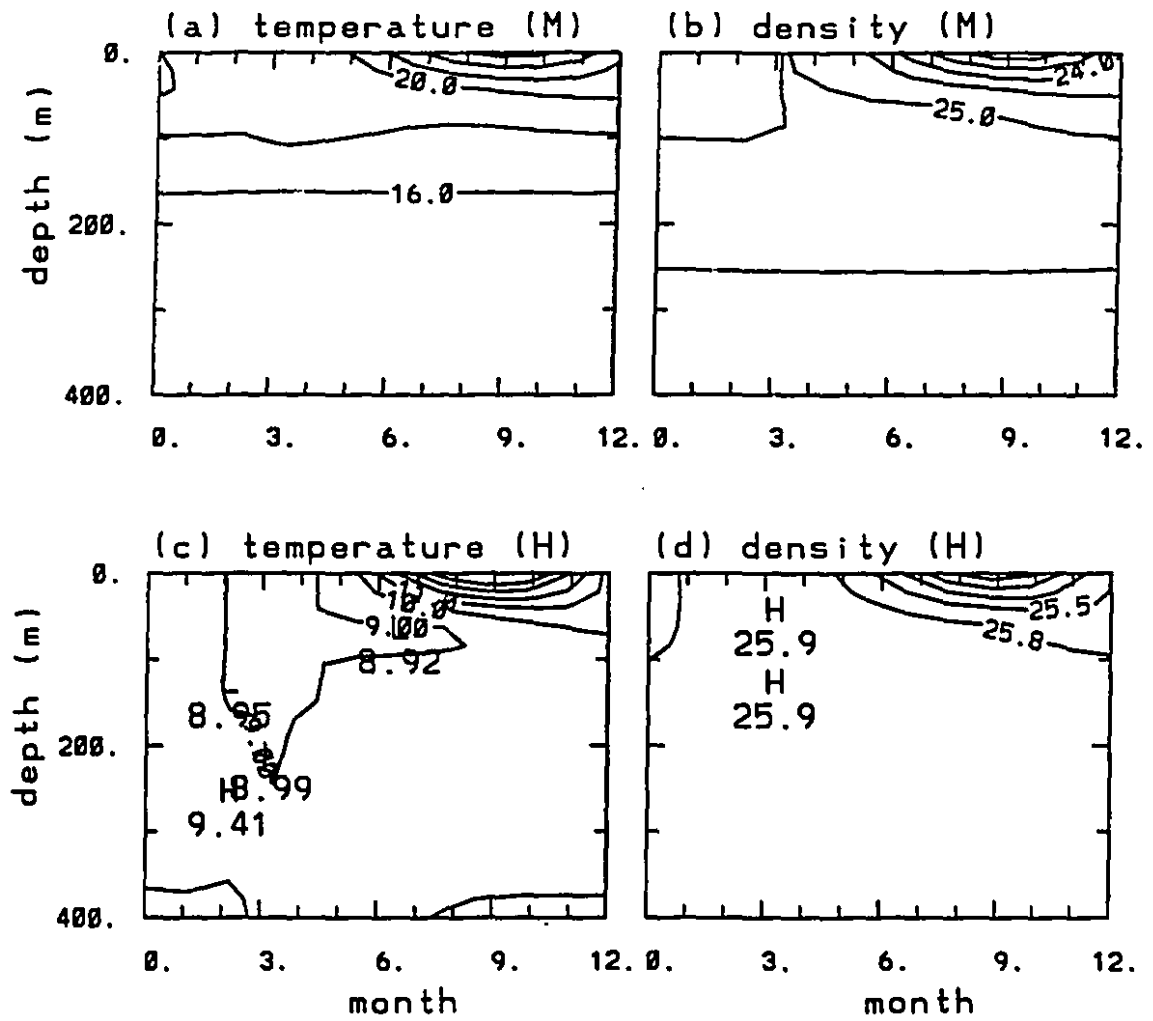


Figure 4.3 The seasonal cycle of temperature ( $^{\circ}\text{C}$ ) and density ( $\sigma$  unit) for Experiment P5 at the mid (M) and high (H) latitude location.

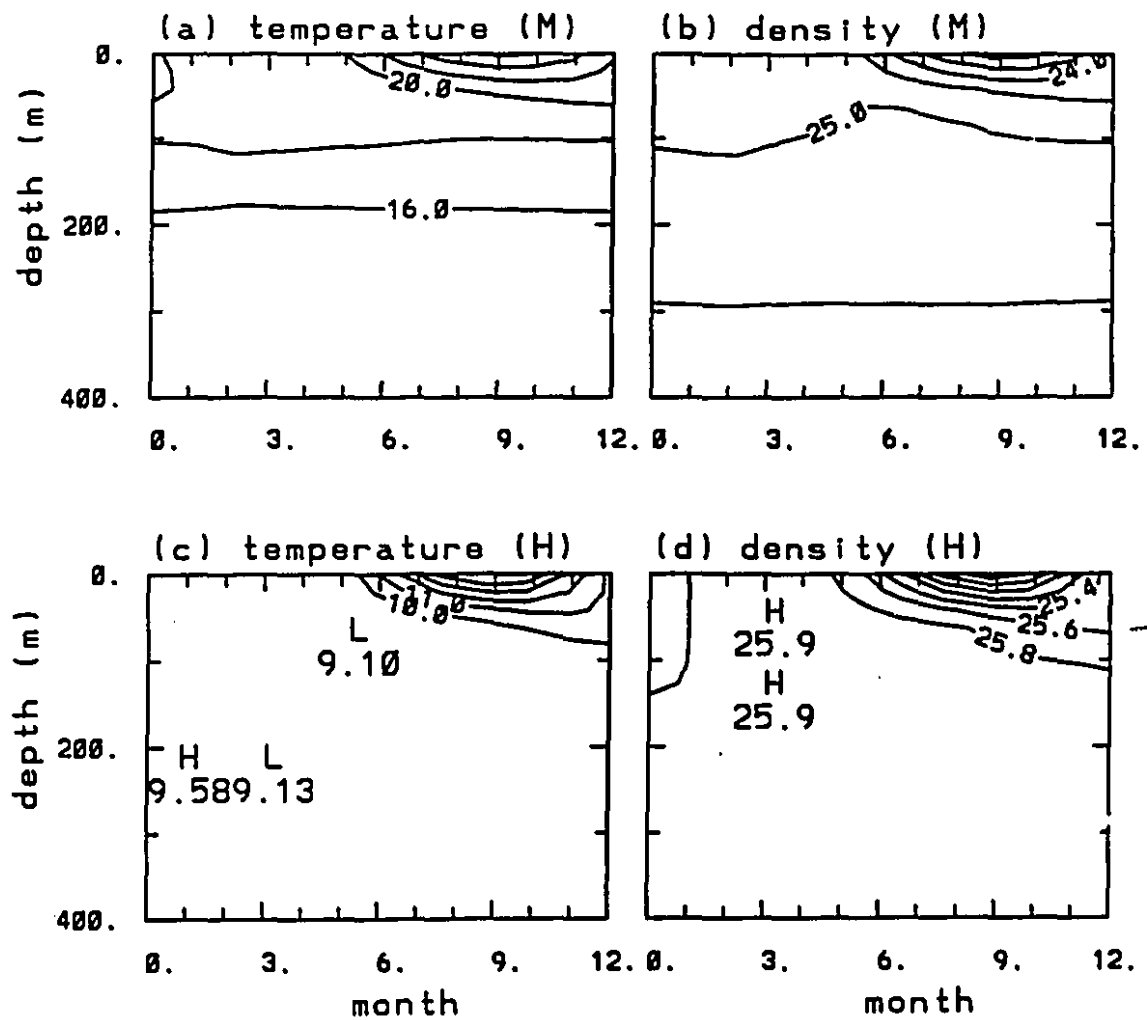


Figure 4.4 As Figure 3, but for Experiment G5 with an increased vertical diffusivity.

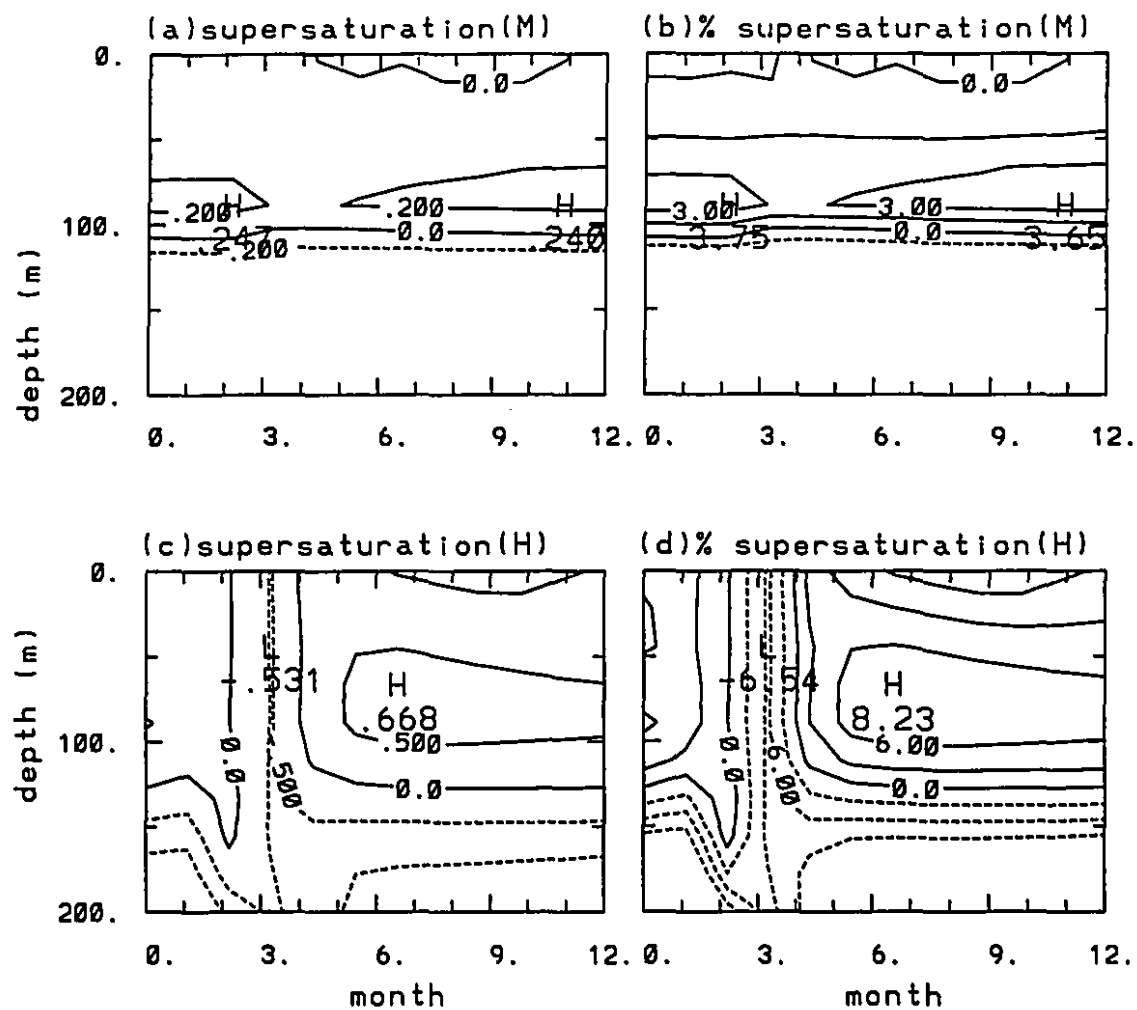


Figure 4.5 The seasonal cycle of oxygen supersaturation ( $\text{ml l}^{-1}$ ) and percentage supersaturation (%) in the top 200 m at the mid (M) and high (H) latitude locations, for Experiment P5.

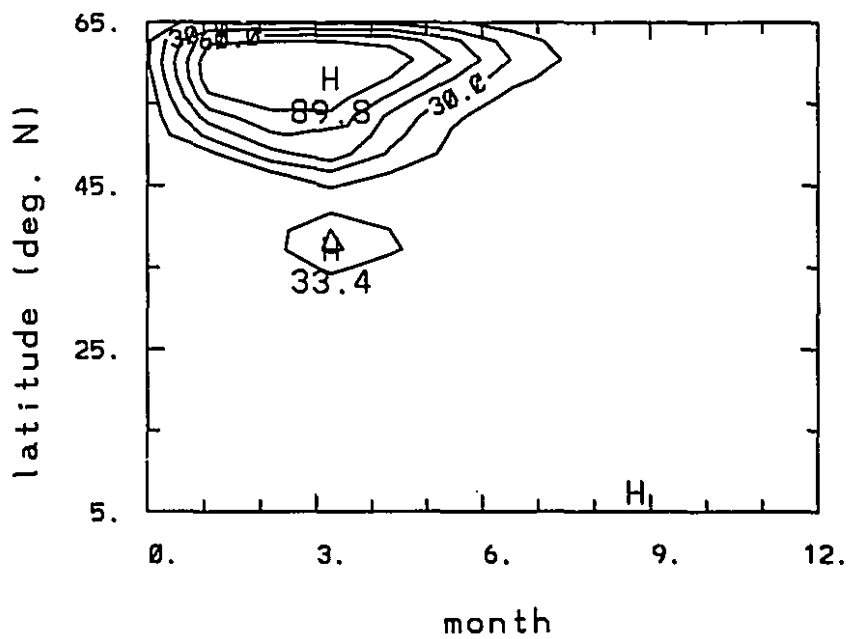


Figure 4.6 The seasonal cycle of the vertically and zonally averaged oxygen production ( $\text{mmol-O}_2 \text{ m}^{-2} \text{ day}^{-1}$ ) due to new production in the euphotic zone, for Experiment P5.

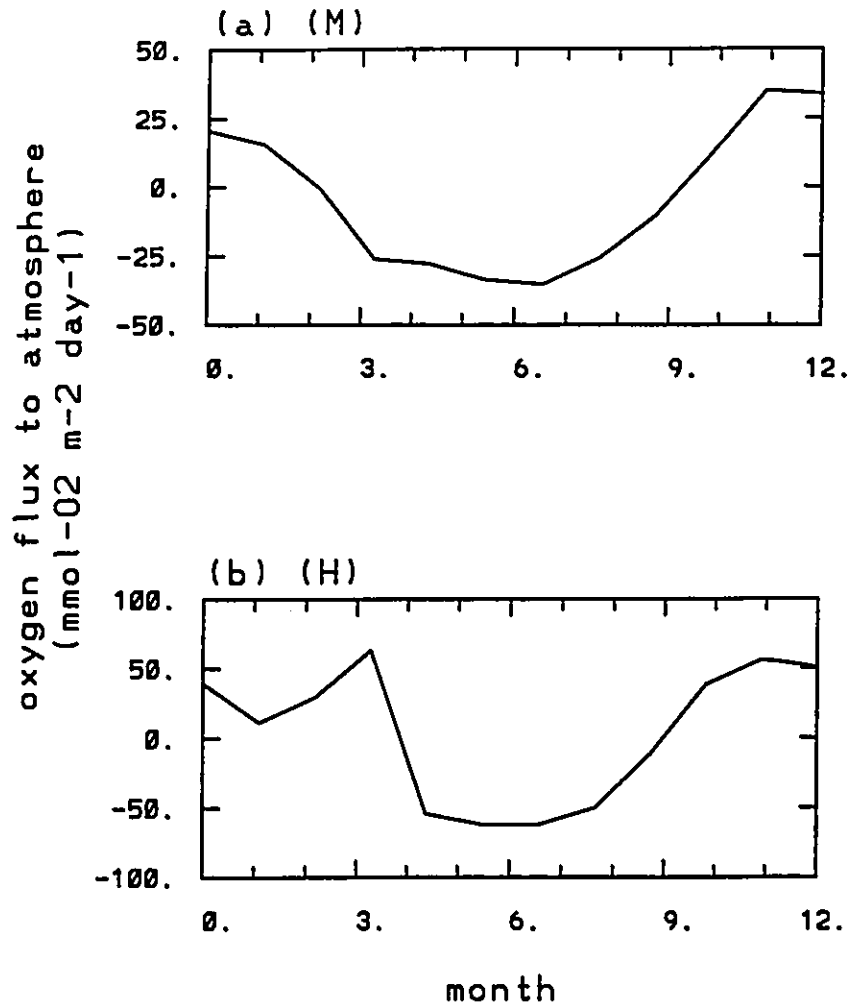


Figure 4.7 The seasonal cycle of the oxygen flux to atmosphere (mmol-O<sub>2</sub> m<sup>-2</sup> day<sup>-1</sup>) at the mid (M) and high (H) latitude locations, for Experiment P5.

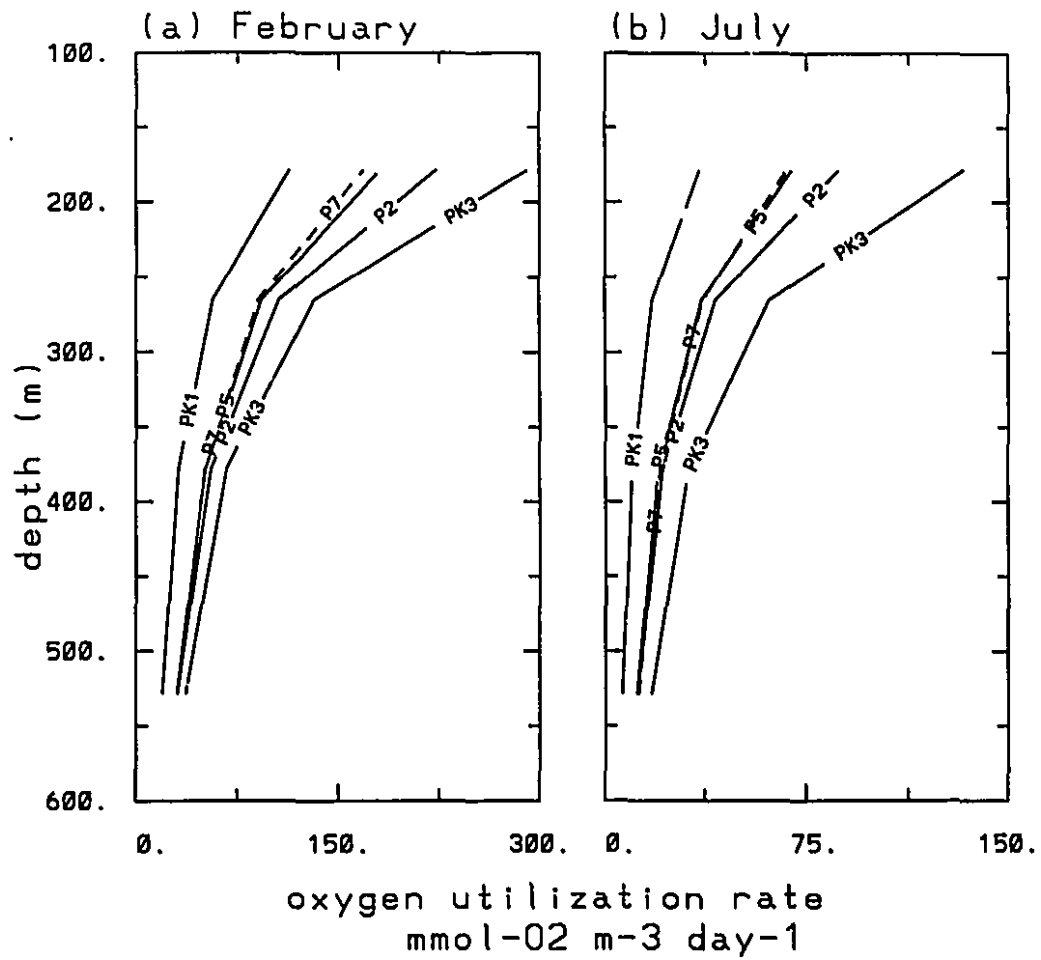


Figure 4.8 The vertical OUR profiles ( $\text{mmol-O}_2 \text{ m}^{-3} \text{ day}^{-1}$ ) for Experiments P7 (dashed), P5, P2, PK1, and PK3 at upper layer (100-600 m) for (a) February, and (b) July.

## Chapter 5

# Particle cycle modelling in the open ocean

### 5.1 Introduction

A significant portion of suspended matter in the ocean exists in the form of aggregates which is composed of organic detritus, inorganic particles, and microorganisms (Riley, 1963). The production, transfer, and decomposition of particulate organic matter in seawater are important for the cycling of biogeochemical elements in the oceans. Particles in the water column exist in a continuum of sizes (McCave, 1984), but two broad classes are frequently recognized: fine suspended material and sinking particles. Fine suspended material with a negligible settling velocity and long residence time constitutes most of the standing stock of particulate matter in the ocean. Sinking particles consisting of fecal pellets and marine snow aggregates are quantitatively rare, but their high settling rates lead to short turnover time. Although comparatively rare, these fast

sinking particles are responsible for the most of the vertical transport of material (Honjo et al. 1984; Fowler and Knauer 1986; Alldredge and Goschalk, 1988; Lee and Wakeham, 1988). Operationally, these two particles classes may be distinguished by different sampling collection methods, suspended material being collected mainly by filtration and sinking material by sediment traps.

The amount and chemical composition of organic matter in suspended and sinking particles result from a balance between the biological processes of production and decomposition, and the physical processes of aggregation and transport. The rate of formation of algal flocs depends on particle size, concentration, and stickiness, as well as on the mechanisms responsible for particle collision, such as Brownian motion, differential settlement and shear (Jackson, 1990; Kepkay, 1994). Fowler and Knauer (1986) show that the large detrital particles responsible for vertical flux are primarily biogenic and range in size and composition. These particles include small, discrete fecal pellets, and large amorphous particles or "snow" containing both organic and inorganic constituents.

The observed distributions of radionuclides, mainly thorium isotopes, can be explained by a reversible exchange model which includes two classes of particle populations: fine and large (Bacon and Anderson, 1982; Bacon et al. 1985; Nozaki et al. 1987; Bacon, 1988). The fine particles are defined as those collected by filtration and include most of the standing crop of particles with no significant settling flux. The large particles, on the other hand, are defined as those collected by sediment traps: they represent a negligible standing stock but play a predominant role in the vertical flux. The

estimated particle aggregation and disaggregation rates are determined using thorium isotope data (Nozaki et al., 1987).

Clegg and Whitfield (1990) developed a 1-dimensional particle cycling model with two particle size classes. They used observational data of particle flux and sinking rate to determine model parameters. Realistic standing concentrations of particulate material were obtained for a steady-state mesotrophic system. In particular, the model successfully simulated the dissolved and particulate profiles of  $^{234}\text{Th}$ ,  $^{228}\text{Th}$ ,  $^{230}\text{Th}$  and  $^{232}\text{Th}$  for a general open ocean case (Clegg and Whitfield, 1991). The model was also applied to particle cycling and  $^{234}\text{Th}$  data at three equatorial Pacific sites, to dissolved and particulate  $^{228}\text{Th}$ ,  $^{230}\text{Th}$ ,  $^{234}\text{Th}$  profiles at station P ( $50^{\circ}\text{N}$ ,  $145^{\circ}\text{W}$ ) (Clegg et al., 1991), and to  $^{234}\text{Th}$  time series and particle data obtained during the JGOFS North Atlantic Bloom Experiments (Clegg and Whitfield, 1993).

The interaction between suspended fine particles and sinking macroaggregates is not well understood, and modelling studies are thus useful. In this chapter, we analyze in detail a 1-dimensional particle cycling model, which is similar to that of Clegg and Whitfield (1990). The steady version of this model is then embedded in the 3-dimensional planetary geostrophic physical model described in Chapter 2. In the following section we present an analytic study of the Clegg and Whitfield (1990) steady state model. Section 5.3 describes numerical results of the 1-dimensional model, including a discussion of aggregation and disaggregation processes, and some comparison with observational results. The coupling of the 1-dimensional particle model with the 3-dimensional physical model is presented in section 5.4, and a summary in section 5.5.

## 5.2 Analysis of the 1-dimensional Clegg and Whitfield (1990) particle cycling model

The 1-dimensional particle cycling model developed by Clegg and Whitfield (1990) was described in Section 2.4 of Chapter 2. To facilitate the derivation of results analytically, we drop the vertical diffusion term in Equation (2.21). We assume that the time scale of vertical diffusion is much larger than that corresponding to typical sinking rates of large particles; this is in general a good assumption. The model equations then become (as in Clegg and Whitfield, 1990),

$$0 = P_r - P_s(\gamma + r_1) + r_2 P_1 \quad (5.1)$$

$$0 = r_1 P_s - P_1(\gamma + r_2) - \partial F_1 / \partial z \quad (5.2)$$

$$F_1 = P_1 S \quad (5.3)$$

Recall the primary production  $P_r = 0$  if  $z < -100$  m, i.e., there is no primary production below the euphotic zone.

The model can be solved analytically by substituting Eqs. (5.1) and (5.3) in (5.2).

The solution can be obtained in two parts. In the euphotic zone ( $z > -100$  m), we have,

$$P_s = P_r / (\gamma + r_1) + r_2 / (\gamma + r_1) [I(z) \int Q_2 I(z') dz' + AI(z)] \quad (5.4)$$

$$P_1 = I(z) \int Q_2 I(z') dz' + AI(z) \quad (5.5)$$

For the aphotic zone ( $z < -100$  m) where  $P_r = 0$ , the solution is ,

$$P_s = Br_2 / (\gamma + r_1) I(z) \quad (5.6)$$

$$P_1 = BI(z) \quad (5.7)$$

where:  $I(z) = \exp(-\int Q_1 dz)$  ;  $Q_1 = 1/S[\gamma + r_2 - r_1 r_2 / (\gamma + r_1)]$  (5.8)

$$Q_2 = - P_1 r_2 / \{(\gamma + r_2)S\} \quad (5.9)$$

there, A and B are constants which can be determined by boundary conditions at the surface and at the base of the euphotic zone. As we are interested in an analytic treatment of the vertical distribution in this section, we leave these constants of integration as undetermined constants. From Table 2.2, we note that  $r_2 > r_1 > \gamma$  at all depths, which implies  $Q_1 > 0$  and  $Q_2 < 0$ .

The fine particle concentration,  $P_s(z)$ , in the euphotic zone consists of a contribution from primary production (first term on the right hand side of Eq. (5.4)), and disaggregation associated with large particle breakup (second term on right hand side). The large particle concentration,  $P_l(z)$ , comes from the net aggregation/disaggregation of small particles from primary production (first term on the right hand side of Eq. (5.5)), and the vertical flux of large particles (second term on the right hand side). The vertical profiles of both the fine and large particle pools are associated with the exponentially decaying function with depth  $I(z)$ . Thus in general, concentrations decrease with depth from the surface. As the relative importance of the contributing terms to  $P_s(z)$  and  $P_l(z)$  varies from point to point, a variation of the vertical profile with location is expected. The overall decrease with depth of the fine and large particles is widely observed (Bishop et al., 1978; Bishop et al., 1980; Fowler and Knauer, 1986; Bishop et al. 1986; Alldredge and Silver, 1988; Silver and Gowing, 1991). For example, Bishop et al. (1986) showed that during July-August, November and December in Panama Basin, the particulate organic carbon concentration for size classes  $< 1 \mu\text{m}$ ,  $1-53 \mu\text{m}$  and  $> 53 \mu\text{m}$  in general decreased with depth. This is also true of the vertical distribution of particulate nitrogen

and phosphorus.

In the aphotic zone, Eqs. (5.6) and (5.7) show that the concentration of fine and large particle pools decreases exponentially with depth, with a characteristic scale given by  $Q_1$ . If we take the latter to be constant, say  $Q_1=k_1$ , we can then obtain an explicit expression for the flux in the aphotic zone.

$$F_1(z) = P_1S = F_{100} \exp[-k_1(|z| - 100)] ; z < -100 \text{ m} \quad (5.10)$$

Here,  $F_{100}$  is the flux at  $z = -100$  m; it depends on the sinking rate  $S$  which is also taken to be constant. Eq. (5.10) can be compared to the flux function of Martin et al. (1987):

$$F(z) = F_{100} (|z| / 100)^b ; z < -100 \text{ m} \quad (5.11)$$

where the exponent  $b = -0.858$ . This power function has an e-folding depth scale of 221 m below the base of the euphotic zone. To compare Eqs. (5.10) and (5.11), we take  $k_1^{-1} = 221$  m, with the sinking rate being  $S = 100 \text{ m day}^{-1}$ . Figure 5.1 shows the normalized flux of  $F_1(z)/F_{100}$  and  $F(z)/F_{100}$  as a function of depth for the two distributions; we have taken three values of the sinking rate  $S = 100, 200, 300 \text{ m day}^{-1}$ . Recall  $Q_1$  (and hence  $k_1$ ) depends on  $S$  through Eq. (5.8). For depths less than 400 m, Martin's power law and the exponential profile with  $S = 100 \text{ m day}^{-1}$  agree well. At larger depths, the latter gives a faster decay of the flux with depth than the former. In fact, Martin's power law gives results which are close in magnitude to the exponential formulation with  $S = 300 \text{ m day}^{-1}$  at a depth of about 2000 m. The discrepancy between the power law and the exponential formulation is thus due to the constant  $k_1$  in the latter. The rates of remineralization, aggregation and disaggregation are much larger in the upper several hundred meters than at depth, thus some vertical variation of  $k_1$  would be expected.

The dependence of the vertical profile of  $F_1(z)$  can be examined further. From Table 2.2, we see that  $\gamma/r_1 \ll 1$ , i.e., the rate constant for remineralization ( $\gamma$ ) is much less than that for aggregation ( $r_1$ ). This allows an expansion in the small parameter  $\gamma/r_1$  to obtain,

$$\begin{aligned} k_1 &= 1/S [\gamma + r_2 - r_2 r_1 / (\gamma + r_1)] = \gamma/S + r_2/S [1 - r_1 / (\gamma + r_1)] \\ &\approx \gamma/S + r_2 / r_1 \gamma/S = \gamma/S (1 + r_2 / r_1) \end{aligned} \quad (5.12)$$

The dependence of the exponential profile  $\exp(-k_1 z)$  for the flux  $F_1(z)$  on model parameters can be interpreted as follows. For slow sinking particulate matter with  $S$  small, the long travelling time in the upper ocean means that there is significant remineralization, resulting in a shallow e-folding depth for the flux  $F_1(z)$ . On the other hand, fast sinking particles with large  $S$  would have a shorter travelling time, resulting in less remineralization and hence a large e-folding depth.

We also note from Table 2.2 that  $r_2/r_1 \gg 1$ , i.e., the disaggregation rate constant ( $r_2$ ) is much larger than the aggregation rate constant ( $r_1$ ). This means that aggregation/disaggregation effects are important over a depth scale which is small compared to the e-folding depth scale given by  $\gamma/S$ . Most of the large particles are disaggregated in the surface layers, with very few reaching the deep ocean. We saw in Figure 5.1 that by tripling the sinking rate  $S$ , the predicted flux at depth using the exponential profile (Eq. (5.10)) better matches the power law of Martin et al. (1987), but the results in the upper few hundreds became worse. With the larger sinking rates, we increase the e-folding depth, and more large particles and macroaggregates can reach, and disaggregate, at greater depths.

The increased particle flux at depth due to an increase in sinking rate suggests that rapidly sinking particles could play an important role for the downward transport of organic matter of surface origin to deep layers. As they sink, macroaggregates and large particles intercept and accumulate fine suspended particles. Since these large particles escape relatively quickly from the upper few hundreds meters of the water column, where the remineralization effect is significant, their organic composition is not as much degraded compared to slowly sinking particles. At depth, when the macroaggregates and large particles break up, the undegraded organic matter originally from the surface is released to the fine particle pool.

The vertical transport of surface organic matter by rapidly sinking macroaggregates and large particles is reported by some observational studies. Wakeham and Canuel (1988) found that the apparent abundance of relatively undegraded phytoplankton "Marker" lipids is associated with fine particulate matter collected by *in-situ* filtration at mid-depth. Silver et al. (1986) also showed that the total number of suspended algal cells in the deep-sea should be a result of fast delivery. Phytoplankton at depth must have originated from the surface waters; despite negligible sinking velocity, ultra-plankton are numerically abundant in deep water (Silver et al., 1986). Photosynthetically-competent algae have been recovered from aphotic depths by Platt et al. (1983).

Wakeham and Canuel (1988) suggested that there is a large particle pool containing a large proportion of apparently undegraded algal cells, perhaps bound loosely together in marine snow aggregates, which are rapidly carried from the surface waters to depths of 1000-2000 m. Disintegration of these particles at depth will contribute

relatively undegraded algal material to the suspended particles pool sampled by in-situ filtration. The sinking rate varies between different particles, and the rapid vertical transport is an integration of both biological and physical processes (e.g., Alldredge and Silver, 1988, Alldredge and Gotschalk, 1989; Silver et al., 1986; Asper, 1987). More observational and data analysis are needed to identify clearly the importance of the large particles. However, our analysis of Eqs.(5.10)-(5.12) is consistent with the view that fecal pellets and marine snow may rapidly transport intact algal cells into the deep layers (e.g. Platt et al., 1983; Silver et al., 1986; Wakeham and Canuel, 1988).

### **5.3 Numerical results from the 1-dimensional particle cycling model**

Knauer and Martin (1981) measured both primary production and particulate flux at a site off the central California coast. Total primary production was  $245 \text{ g-C m}^{-2} \text{ yr}^{-1}$ , with a stable value over the 6-day measurement period. Clegg and Whitfield (1990) used these data to investigate the depth variation of the production and flux within the surface layer. The measurements of Knauer and Martin (1981) showed that the production rate decreases with depth in the surface layer (Clegg and Whitfield, 1990). Thomas et al. (1990) parameterize the new production in euphotic zone as cosine function, a similar approach was used here to parameterize the primary production in our model,

$$P_r = P_0 C \cos(0.5\pi|z|/z_0) \quad (5.13)$$

where  $P_0$  is the vertically integrated primary production rate,  $C$  is a constant which normalizes the cosine function to unity when integrated through the euphotic zone,  $z_0=100$

$m$  is the depth at the bottom of euphotic zone. Recall the depth in the euphotic zone is  $|z| \leq 100$  m. The model is run by using observed values of  $P_0$ , with both fields of fine particles ( $P_s$ ) and large particles ( $P_l$ ) initially set to zero. The different primary production rates ( $P_0$ ) used in our study are  $245 \text{ g-C m}^{-2} \text{ yr}^{-1}$  of Knauer and Martin (1981),  $103 \text{ g-C m}^{-2} \text{ yr}^{-1}$  of Clegg and Whitfield (1990) and  $130 \text{ g-C m}^{-2} \text{ yr}^{-1}$  estimated by Martin et al. (1987). The vertical profiles of primary production associated with these different rates are shown in Figure 5.2.

Using Knauer and Martin's (1981) primary production rate, we obtain the vertical flux simulated by the 1-dimensional model shown in Figure 5.3. The simulated flux using the remineralization rate of Table 2.2 is comparable to the data of Knauer and Martin (1981). Increasing the remineralization rate results in a reduced particulate sinking flux, with more sinking particles remineralized in the upper layers, while a decrease has the opposite effect. The export flux from the euphotic zone calculated in our model is  $57.3 \text{ g-C m}^{-2} \text{ yr}^{-1}$  at a depth of 100 m. Knauer and Martin's (1981) observational data were fitted by Clegg and Whitfield (1990); the latter then calculated an export flux at 100 m of  $46 \text{ g-C m}^{-2} \text{ yr}^{-1}$ . Betzer et al. (1984), using primary production data and organic carbon flux measurements below 200 m, obtained an equation for the export flux as a function of both surface primary production and depth. From the equation of Betzer et al. (1984) and the surface primary production rate of Knauer and Martin (1981), the export flux at 100 m was found to be  $57 \text{ g-C m}^{-2} \text{ yr}^{-1}$ . Our results compare reasonably with these estimates.

Now we compare our 1-dimensional time dependent model with the results of

Clegg and Whitfield (1990) and Martin et al. (1987). For the primary production rate of Clegg and Whitfield (1990), the simulated vertical flux is shown in Figure 5.4(a). At a depth of 100 m, Clegg and Whitfield (1990) estimated an export flux of  $18.4 \text{ g-C m}^{-2} \text{ yr}^{-1}$ , compared to our model value of  $21.3 \text{ g-C m}^{-2} \text{ yr}^{-1}$ . Using the same primary production rate, Betzer et al. (1984) calculated a flux of  $15.7 \text{ g-C m}^{-2} \text{ yr}^{-1}$ . However, an estimate of the flux using the Eq. (1) of Eppley and Peterson (1979) gives a higher value of  $26.5 \text{ g-C m}^{-2} \text{ yr}^{-1}$ .

We now turn to the simulated flux using Martin et al.'s (1987) estimate of the primary production (Figure 5.4(b)). To maintain their composite open ocean organic carbon flux profile for depth 100-2000 m layer, Martin et al. (1987) estimated a supporting primary production of  $130 \text{ g-C m}^{-2} \text{ yr}^{-1}$ . Using this increased primary production rate, our model yields a flux of  $26.3 \text{ g-C m}^{-2} \text{ yr}^{-1}$ , compared to an average open ocean observational estimate of  $18.4 \text{ g-C m}^{-2} \text{ yr}^{-1}$  ( $1.53 \text{ mol-C m}^{-2} \text{ yr}^{-1}$ , Martin et al., 1987). The estimate of Martin et al. (1987) is based on 123 flux measurements, and the fluxes at different sites varied from  $85.0 \text{ g-C m}^{-2} \text{ yr}^{-1}$  to  $13.4 \text{ g-C m}^{-2} \text{ yr}^{-1}$ . The simulated flux in our model is consistent with the model estimates of Eppley and Peterson (1979), Betzer et al. (1984), and Clegg and Whitfield (1990), but are larger than the average estimate of Martin et al. (1987).

Using Clegg and Whitfield's (1990) primary production rate of  $103 \text{ g-C m}^{-2} \text{ yr}^{-1}$ , our model simulated the concentration of total organic carbon ( $P_s+P_l$ ) shown in Figure 5.5(a). Clegg and Whitfield (1990) reported a maximum of  $24.0 \text{ mg-C m}^{-3}$  at about 30-40 m, in our model this maximum is  $30.0 \text{ mg-C m}^{-3}$  at around 50 m. But in general, this 1-

dimensional model is capable of reproducing the major features of the steady state particle cycle model of Clegg and Whitfield (1990). The percentage of mass ratio ( $P_l/P_s$ ) is shown in Figure 5.5(b). The maximum contribution from the large particles reaches 6.2% in the upper 20 m. Below 1000 m, the mass contribution drops to about 2.5-3%. The model results suggest that the particle flux involves only a small proportion of the total particle mass. For the layer below 1000 m, Table 2.2 shows that ratio of aggregation to disaggregation rate ( $r_1/r_2$ ) is about 2.1%. This rate ratio is comparable with the simulated mass ratio  $P_l/P_s$  below 1000 m. In the deep ocean, where the primary production is zero, if the remineralization rate is assumed to be small compared to the exchange rate between the  $P_s$  and  $P_l$  reservoirs, then the ratio  $P_l/P_s$  can be approximated by  $r_1/r_2$  from Eq. (5.1), as confirmed by our result. The simulated mass ratio can be compare to  $^{230}\text{Th}$  data obtained by Nozaki et al. (1987), although these measurements were obtained in the western Pacific and the Sea of Japan. For western Pacific sites AN-1 and AN-4, the estimated value of the  $P_l/P_s$  ratio is 1.56% and 1.60% respectively (Nozaki et al., 1987).

We now turn to a discussion of aggregation and disaggregation processes. Measurements of dissolved and particulate  $^{230}\text{Th}$  have shown that there is a continuous two-way exchange between  $P_s$  and  $P_l$  throughout the water column (Bacon and Anderson, 1982; Nozaki et al. 1987). Production by aggregation and disaggregation processes simulated by the model are shown in Figure 5.6(a). At steady state, the two effects are almost equal at all depths (except for the relatively small sinking flux of large particles). Thus the gain of suspended particles by disaggregation is balanced by the loss due to aggregation process, with a continuous exchange between the large and small particle

reservoirs and the accompanying aggregation and disaggregation in operation. This could be compared to the result of the  $^{230}\text{Th}$  by a reversible exchange model (Bacon and Anderson, 1982). At steady state, the gain of  $^{230}\text{Th}$  by uptake (adsorption) is balanced by the losses due to release (desorption) and radioactive decay. For the long-lived isotope  $^{230}\text{Th}$ , radioactive decay is negligible, and thus the main balance is between uptake and release.

The aggregation and disaggregation rates are difficult to observe or measure directly. Clegg and Whitfield (1991) pointed out that, while  $r_1/r_2$  may be determined quite accurately in deep water from  $^{230}\text{Th}$  profiles, estimates of the absolute values of the rate constants are subject to large errors. The value of  $r_1$  and  $r_2$  previously obtained from  $^{230}\text{Th}$  measurements in the deep ocean by Nozaki et al. (1987) range from  $150 \text{ yr}^{-1}$  to about  $750 \text{ yr}^{-1}$  for  $r_2$ , with an almost constant ratio ( $r_1/r_2$ ). Clegg and Whitfield's (1991) calculations suggest that the  $^{230}\text{Th}$  distribution is insensitive to cycling rates between small and large particles reservoirs for values of  $r_2$  greater than about  $51 \text{ yr}^{-1}$ . To investigate the model sensitivity to aggregation and disaggregation rates, we increase  $r_1$  and  $r_2$  by a factor of 5 for depths below 600 m, keeping their ratio constant;  $r_2$  thus increases from  $148 \text{ yr}^{-1}$  to  $750 \text{ yr}^{-1}$ . The results are shown in Figure 5.6(b). The total particulate organic carbon concentration remains unchanged for the layers above 600 m, and the change is negligible below this depth. This shows that the simulated deep ocean particle distributions are insensitive to the absolute values of  $r_1$  and  $r_2$  over the range determined by Nozaki et al. (1987). Similar results were also found by Clegg and Whitfield (1990, 1991).

Altabet et al. (1991) investigated the source and transformation of large, fast-sinking particles in the North Atlantic ocean using nitrogen isotope ratio  $^{15}\text{N}/^{14}\text{N}$  as an *in situ* tracer. The increase in  $\delta^{15}\text{N}$  for suspended particles with depth is thought to result from progressive decomposition and removal of dissolved nitrogen depleted in  $^{15}\text{N}$ . Similarly,  $\delta^{15}\text{N}$  values for sinking particles would be expected to increase with depth, although less rapidly for suspended particles, as the large sinking speeds of the large particle allow much less time for decay. However Altabet et al found that  $\delta^{15}\text{N}$  values for sinking particles actually decreased with depth during low-flux periods in the open ocean, implying that the fine and large particle pools may not interact as intensely as supposed. They suggested that micro-environments within large, sinking particles may enhance microbial activity that leads either to the selective removal of  $^{15}\text{N}$ -enriched material or the addition of  $^{15}\text{N}$ -depleted material. More studies are needed to identify clearly the interaction between the suspended and sinking particles.

#### **5.4 Embedding the 1-dimensional particle model in the 3-dimensional circulation model**

In this section, we couple the steady state 1-dimensional particle model (Eq.(5.1)-(5.3)) with the planetary geostrophic circulation model. The simulated zonally averaged distribution of the vertical flux of large particles ( $F_l$ ) and concentration of suspended organic carbon particles ( $P_s$ ) are shown in Figure 5.7. Both quantities have their largest values in the upper few hundred meters. In the northern latitude band ( $50^{\circ}$ - $60^{\circ}\text{N}$ ), the

formation of deep water leads to a downward transport of particulate matter, which in turn results in a high concentration of suspended fine particles, and also a high particle flux through aggregation at depths of 500-1000 m. A downward transport of nutrient in the northern model domain is also found in simulations of nitrate distribution (Su et al., 1994). Martin et al. (1987) showed results of a California-Hawaii carbon flux section: in the open ocean area, the flux at depths of 100, 500 and 1000 m is about 18-24, 6-12 and 3.5-7.2 g-C m<sup>-2</sup> yr<sup>-1</sup>, respectively; these values are not for a zonally averaged distribution. Nevertheless, the magnitude of our model flux at depth is comparable with their results.

The horizontal distribution of the particle flux at the bottom at the euphotic zone ( $z=114$  m) is shown in Figure 5.8(a). Throughout most of the mid-latitude band 15°-35°N, the flux is less than 12 g-C m<sup>-2</sup> yr<sup>-1</sup>, with the flux near the northern edge of the domain being larger than in the mid-latitude band 15°-35°N. A similar pattern is also found for the suspended particle field (Figure 5.8(b)). The high concentrations are associated with the Gulf Stream circulation: the maximum in the northern half of the domain (35°N-50°N) results from advection of the fine particles by the northward flowing Gulf Stream. This high concentration of fine particulate organic matter in turn supports a high large particle concentration through aggregation. The importance of the Gulf Stream in lateral transport of dissolved and suspended nutrient has been studied through both observational data analysis (Martin et al., 1987; Rintoul and Wunsch, 1991) and model simulations (Bacastow and Maier-Reimer, 1991; Najjar et al. 1992; Su et al., 1994).

The magnitude of export flux simulated in our model (Figure 5.8(a)) is comparable with some observational studies. The flux reaches a maximum of about  $20.2 \text{ g-C m}^{-2} \text{ yr}^{-1}$  at latitude of  $45^{\circ}\text{N}$ . In the northern part of the domain, the flux is above  $12 \text{ g-C m}^{-2} \text{ yr}^{-1}$ ; and in the  $15^{\circ}$ - $40^{\circ}\text{N}$  latitude band, it is in the range of  $8$ - $12 \text{ g-C m}^{-2} \text{ yr}^{-1}$ . The export flux estimated by Martin et al. (1987) at six offshore stations (VERTEX 2, 4, 5, II, III and NPEC) ranged from  $13.4 \text{ g-C m}^{-2} \text{ yr}^{-1}$  to  $85 \text{ g-C m}^{-2} \text{ yr}^{-1}$  at a depth of 100 m. In an open ocean location such as VERTEX 4, located in the transition region between the California Current and subtropical gyre, the flux was about  $24.6 \text{ g-C m}^{-2} \text{ yr}^{-1}$ . The flux at VERTEX 5, located in the subtropical gyre, was  $14 \text{ g-C m}^{-2} \text{ yr}^{-1}$  (Martin et al. 1987). Using Martin et al's function (Eq.(5.11)), we calculate the flux at the base of euphotic zone ( $z=114 \text{ m}$ ) to be  $22 \text{ g-C m}^{-2} \text{ yr}^{-1}$  and  $12.5 \text{ g-C m}^{-2} \text{ yr}^{-1}$  at VERTEX 4 and 5 locations respectively. Interpolating carbon flux data from Knauer and Martin (1981), gives a flux of  $9.6 \text{ g-C m}^{-2} \text{ yr}^{-1}$  at a depth of 114 m.

The simulated concentration of suspended particulate organic matter ( $P_s$ ) at the bottom of the euphotic zone is shown in Figure 5.8(b). The concentration reaches a maximum of  $22 \text{ mg-C m}^{-3}$  near  $45^{\circ}\text{N}$ . In the northern part of the model domain, it is above  $12 \text{ mg-C m}^{-3}$ ; and in the  $15^{\circ}$ - $40^{\circ}\text{N}$  latitude band, it is about  $10 \text{ mg-C m}^{-3}$ . Wakeham and Canuel (1988) reported concentrations of  $17 \text{ mg-C m}^{-3}$  at a depth of about 114 m in the VERTEX II and III stations, which are located 400 km off Mexico. Karl and Knauer (1984) reported suspended particulate organic matter concentrations of about  $20 \text{ mg-C m}^{-3}$  at a depth of 100 m at VERTEX I, a station approximately 100 km off Point Sur, California. Our simulated concentration magnitudes agree with these observational data.

The domain averaged vertical profiles of total organic carbon ( $P_s+P_f$ ) and organic carbon flux ( $F_f$ ) are shown in Figure 5.9. The profiles are consistent with simulated results of the 1-dimensional time dependent model, which are in turn comparable with the results of Clegg and Whitfield (1990). This result is expected as advection and horizontal diffusion only redistribute particulate matter within the domain. The  $P_f$  concentration can be estimated by dividing the particle flux by the constant sinking rate  $S=100$  m day<sup>-1</sup>. The  $P_f/P_s$  ratio estimated in this way lies in the range of 2-5%. The corresponding ratio for the 1-dimensional model presented in Section 5.3 is about 2-6%.

We close this discussion by noting that in the upper 30 m, the remineralization, aggregation and disaggregation rates are much higher than the layers below (Table 2.2). In the top 30 m, there are 5 levels for the 1-dimensional model, but only 1 level for the 3-dimensional model. This means that the vertical structure due to the layer rate variations is better simulated in the former model. The vertical profiles simulated by the 1-dimensional model show a relative low flux and particulate concentrations at the surface, and a maximum located at the about 50 m depth. Due to the poorer vertical resolution in the surface layers, the 3-dimensional model cannot resolve these fine vertical structure resulting from remineralization, aggregation and disaggregation processes. The particulate concentration and flux near the surface are thus higher in the 3-dimensional model, compared to the 1-dimensional results. This can be seen by comparing Figure 5.4, Figure 5.5 and Figure 5.9. At greater depths, the general decrease with depth is simulated by both models. Our results suggest that coarse resolution models are able to reproduce the major features of the particulate concentration and flux distribution.

## 5.5 Summary

The 1-dimensional particle cycling model of Clegg and Whitfield (1990) has been analyzed in detail. An analytical solution is obtained for the steady state model. The solution shows that fast sinking particles may escape the upper few hundred meters of the water column quickly, with little degradation. When these particles reach greater depths and disaggregate there, suspended organic matter of surface origin has therefore been transported downward. Our analysis shows that with an increase sinking rate, the particle flux e-folding depth increases. This suggests the importance of fast sinking particles in the vertical transport of undegraded organic matter to deep layers.

Based on the steady state Clegg and Whitfield model, a 1-dimensional time dependent model was developed and tested. This model is forced by different values of the primary production rate at the surface, with both the fine and large particle fields initially set to zero. The simulated concentration of suspended organic particles and large particle flux agree with observational studies, and with the steady state model results of Clegg and Whitfield (1990). Aggregation and disaggregation occur throughout the water column, with material being transferred between fine and large particle pools through a continuous two-way exchange. The downward transport of organic material is mainly accomplished by large, sinking particles. The latter have a small mass ratio relative to the total particulate pool. The ratio of large to fine particle concentration ( $P_l/P_s$ ) ranges from 5-6% in the upper 50 meters, to about 2.5-3% at depths below 1000 m.

The particle model has also been embedded in the 3-dimensional physical model.

The simulated organic carbon flux and particulate organic matter concentration are comparable with observational studies. The domain averaged vertical profile of particulate concentration and vertical flux are comparable with 1-dimensional model simulations and observational studies.

The particle model groups all types of particulate matter only according to two size classes. Thus aggregation refers to the rate of production of fecal material and formation of large aggregates through biological and physical processes, while disaggregation refers to mechanisms of breakup, dissolution and grazing of large particles, which are then reassimilated into the small suspended size fraction. Proper estimates of aggregation and disaggregation rate constants ( $r_1$ ,  $r_2$ ), essential for modelling, are not easily obtained through observations. Estimates from  $^{230}\text{Th}$  data (Nozaki et al., 1987) show that although the ratio of  $r_1/r_2$  is almost constant, the value of  $r_1$  and  $r_2$  themselves can vary over a large range. In addition, some spatial variation in  $r_1$  and  $r_2$  and the remineralization rate can be expected. Such variation could lead to different results in a more complete model.

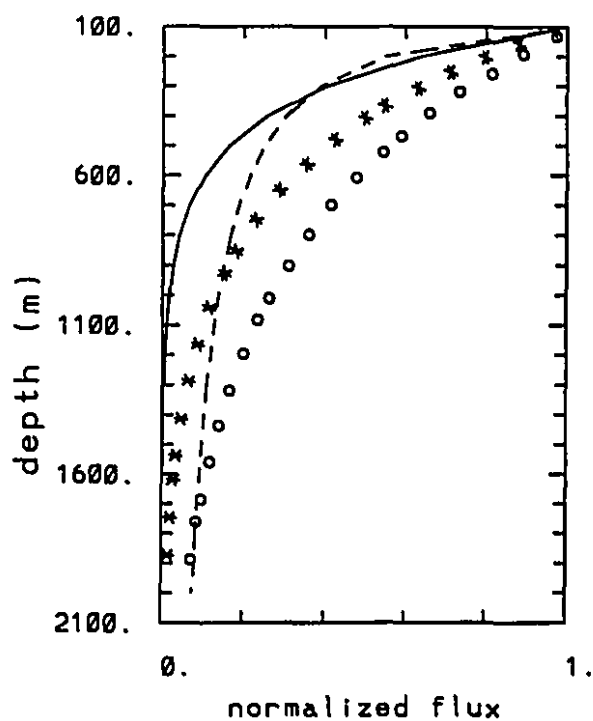


Figure 5.1 The normalized flux  $F_1/F_{100}$  and  $F(z)/F_{100}$  for the exponential formulation of Eq. (5.10) with sinking rates  $S=100$  (solid), 200 (asterisk), 300 (circle)  $\text{m day}^{-1}$ . The dashed line is from Martin et al. 's (1987) power law formulation, Eq. (5.11).

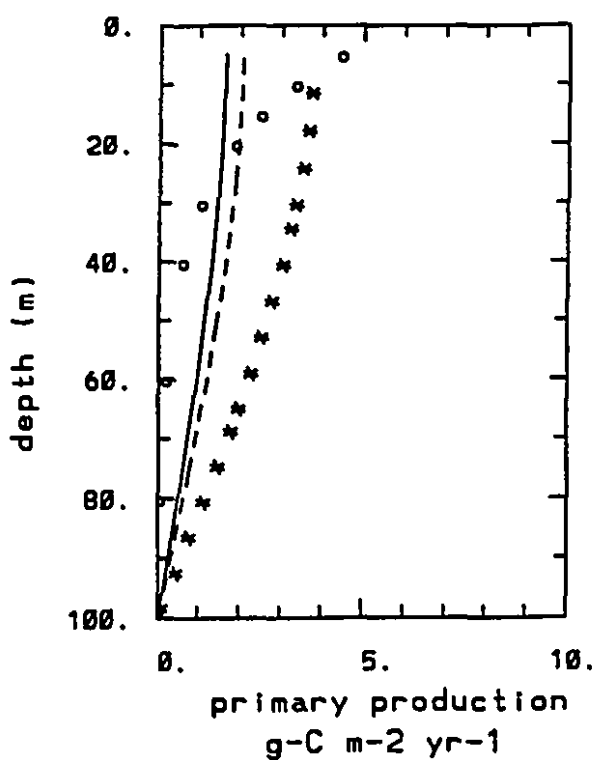


Figure 5.2 Vertical profile of primary production with primary production rates ( $P_0$ ) of  $103 \text{ g-C m}^{-2} \text{ yr}^{-1}$  of Clegg and Whitfield (1990) (solid),  $130 \text{ g-C m}^{-2} \text{ yr}^{-1}$  of Martin et al. (1987) (dashed), and  $245 \text{ g-C m}^{-2} \text{ yr}^{-1}$  of Knauer and Martin (1981) (asterisk). The open circles (o) represent the primary production used in Clegg and Whitfield's (1990) particle cycling model.

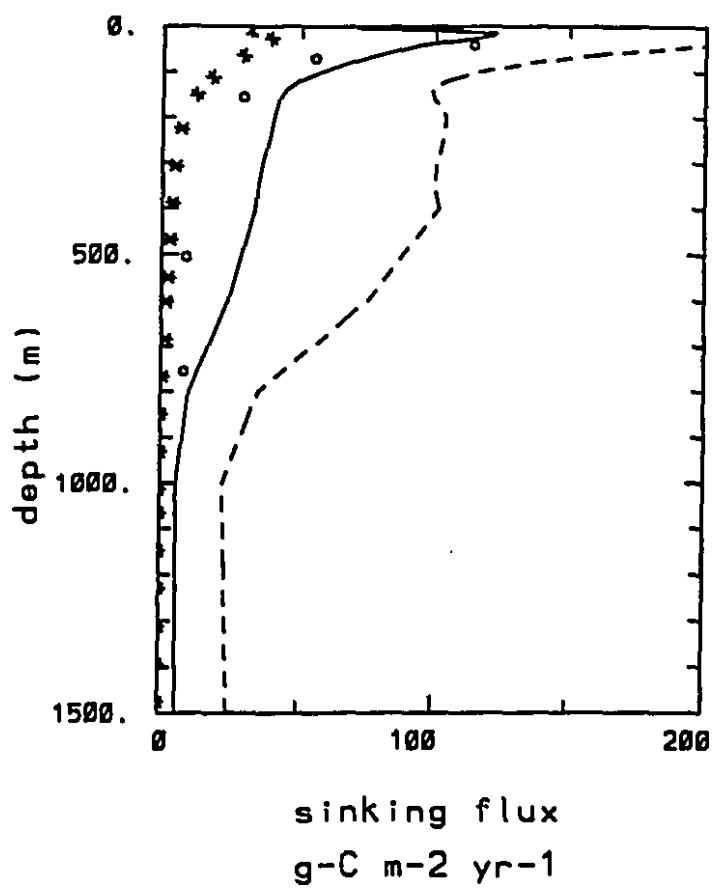


Figure 5.3 The simulated particulate organic carbon sinking fluxes using the remineralization rates of Table 2.2 (solid), and half (dashed) and double (asterisk) that rate. The observational data (o) are from Knauer and Martin (1981). The units are  $\text{g-C m}^{-2} \text{ yr}^{-1}$ .

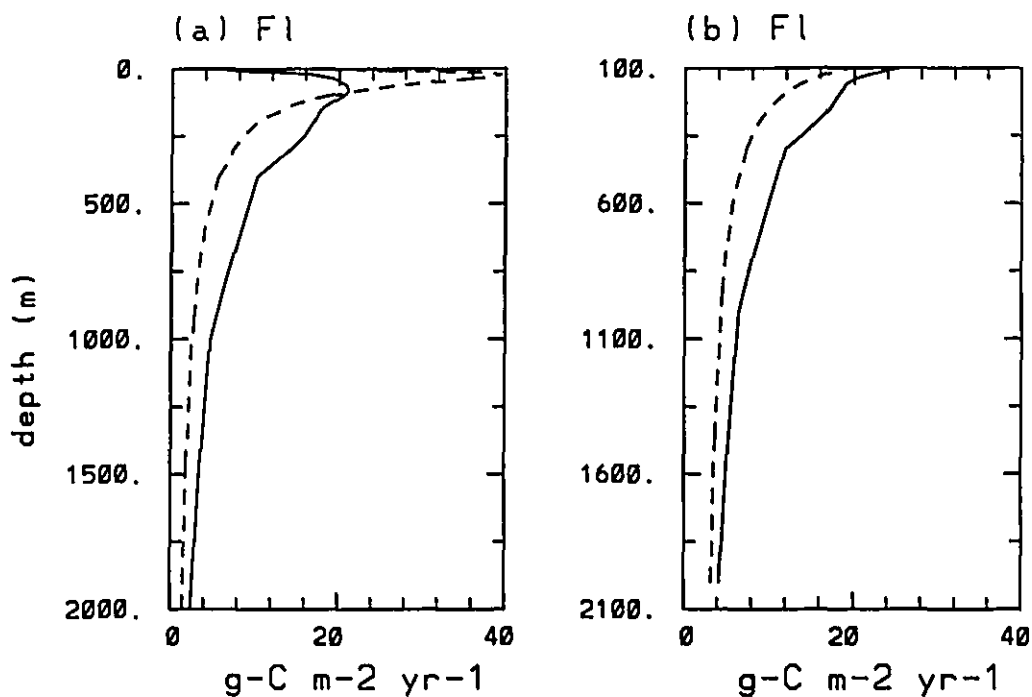


Figure 5.4 The simulated large particle organic carbon flux ( $F_1$ ) using different primary production rates ( $P_0$ ): (a)  $103 \text{ g-C m}^{-2} \text{ yr}^{-1}$  of Clegg and Whitfield (1990); (b)  $130 \text{ g-C m}^{-2} \text{ yr}^{-1}$  of Martin et al. (1987). The solid curves are the simulated flux, while the dashed curves are the fluxes calculated by Clegg and Whitfield (their Table A1) in (a), and Martin et al. (their Figure 5) in (b).

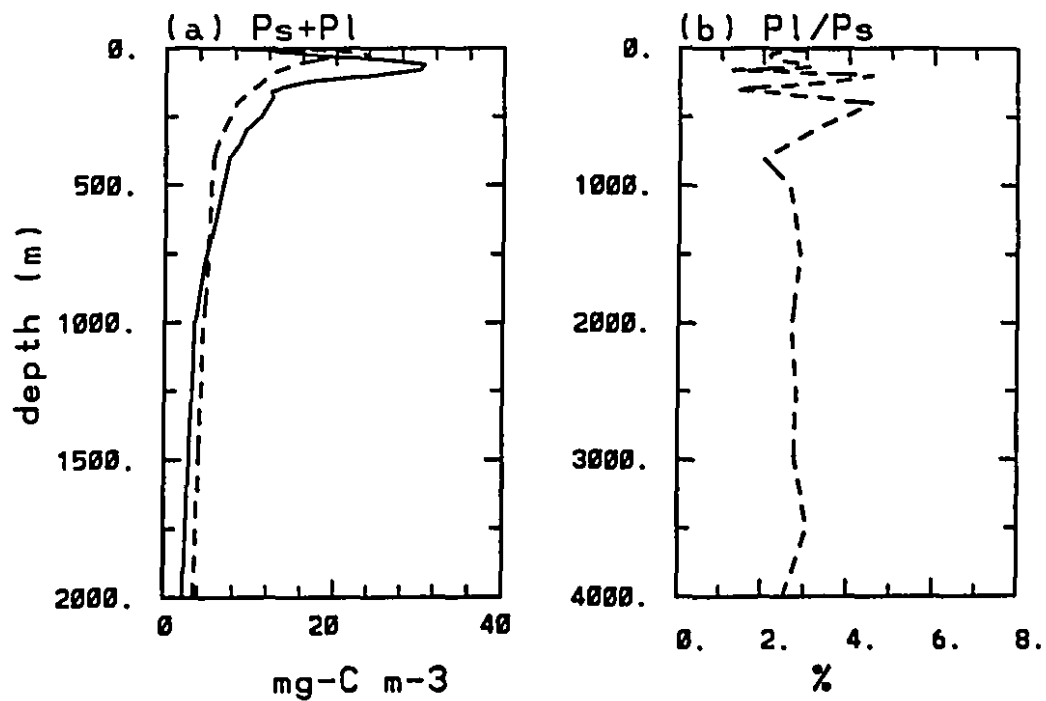


Figure 5.5 (a) The simulated total organic carbon concentration ( $P_s + P_l$ ) (solid), and the Clegg and Whitfield's (1990; their Figure 8) estimate (dashed). (b) The percentage of mass ratio  $P_l/P_s$  simulated by the model. The maximum value of 6.2% is reached in the upper 20 m. A primary production rate of  $103 \text{ g-C m}^{-2} \text{ yr}^{-1}$  from Clegg and Whitfield (1990) is assumed.

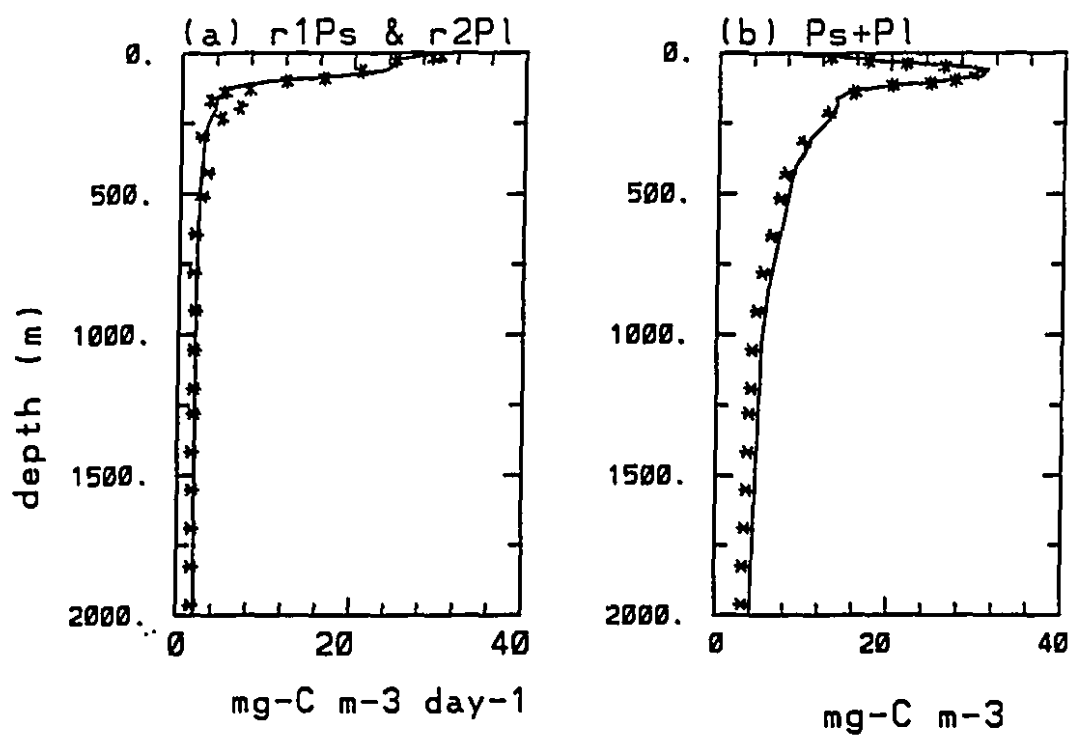


Figure 5.6 (a) The simulated aggregation ( $r_1P_s$ ; solid) and disaggregation ( $r_2P_l$ ; asterisk) rates at steady state. (b) The simulated particulate organic carbon concentration ( $P_s+P_l$ ) using the aggregation and disaggregation rates of Table 2.2 (solid), and an increase of these rates by a factor of 5 below 600 m, keeping their ratio constant (asterisk). The primary production rate used is  $103 \text{ g-C m}^{-2} \text{ yr}^{-1}$ , as in Figure 5.5.

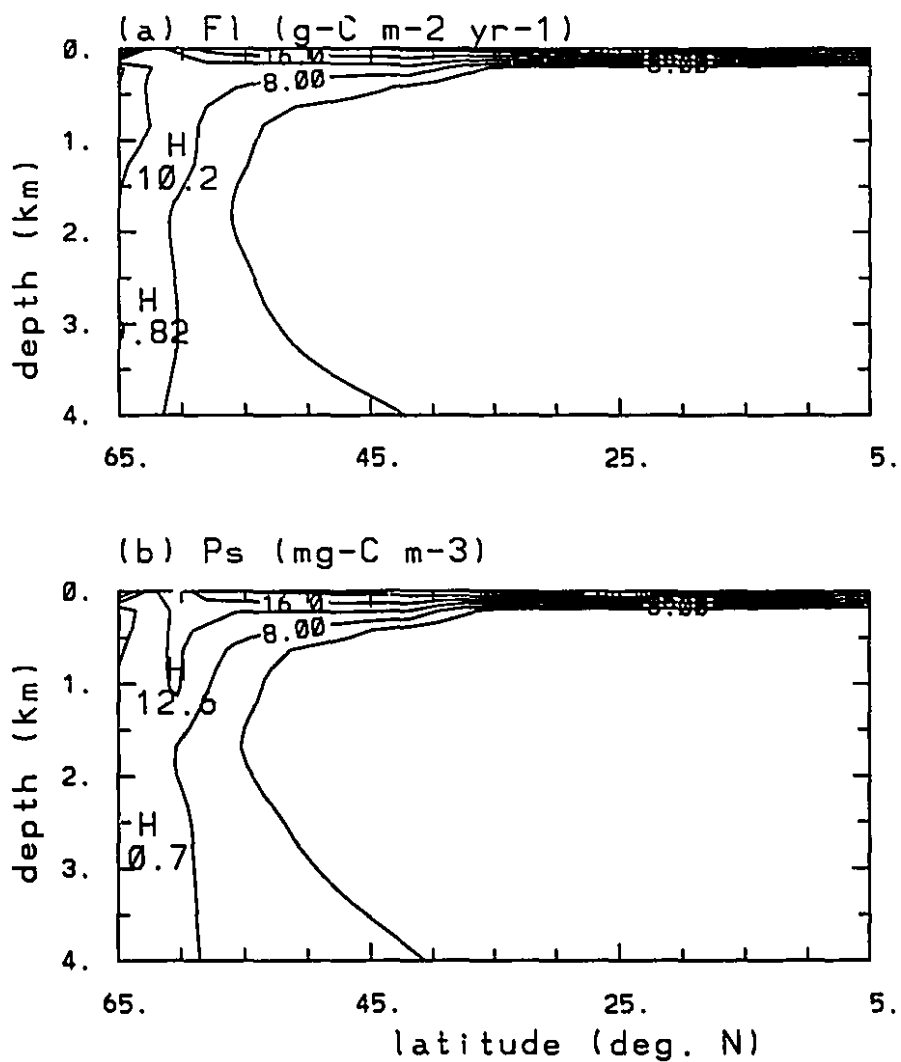


Figure 5.7 The simulated zonally averaged distribution of (a) large particle flux ( $F_1$ ); and (b) suspended particulate organic carbon concentration ( $P_s$ ).

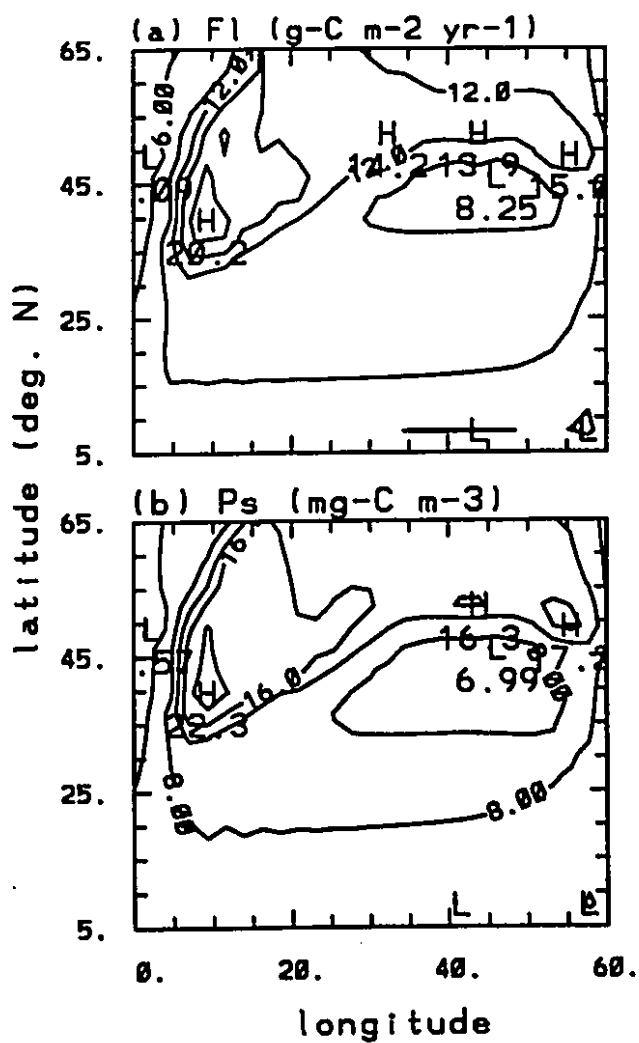


Figure 5.8 The horizontal distribution of (a) the large particle flux ( $F_1$ ), and (b) the concentration of suspended organic carbon particles ( $P_s$ ); at a depth of 114 m, the bottom of the euphotic zone.

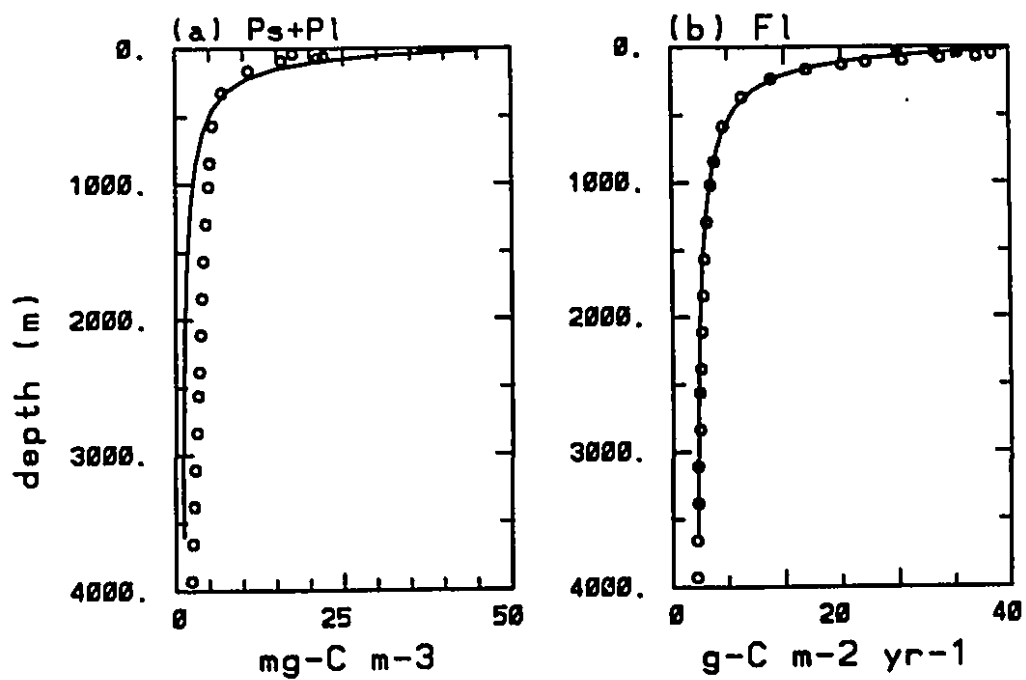


Figure 5.9 The domain averaged vertical profile of (a) total organic carbon concentration ( $P_s+P_l$ ), and (b) large particle flux ( $F_l$ ), simulated by the 3-dimensional model. Results from Clegg and Whitfield's (1990; their Figure 8 and Table A1) 1-dimensional model are shown by the open circles.

## Chapter 6

### Conclusions

In this thesis, we have coupled a physical model with a biological model to examine nutrient cycling in the North Atlantic Ocean. The physical model is a 3-dimensional planetary geostrophic ocean general circulation model (Zhang et al., 1992). Two different formulations are used to represent new production in the biological model. The first is based on new production being given by a restoring condition of surface nitrate to its observed concentration (restoring model), and the other on nitrate limiting the rate of new production (kinetic model). The latter formulation is an extension of the Michaelis-Menton kinetics equation. The biological model includes both organic and inorganic matter. Later, a particle model consisting of two particle size classes is included.

The restoring model is coupled with the annual mean mode of the physical model. The coupled model is used to examine the hypothesis (Martin et al., 1987) that latera!

transport and decomposition of slow or non-sinking organic matter causes a non-local balance between remineralization rate and the overlying new production rate in some open ocean regions. The model results agree well with the North Atlantic nutrient transport calculated from observed nutrient and hydrographic data. There is a net northward transport of inorganic nitrate in the mid-latitude band of 25°-40°N due to the strong northward flowing Gulf Stream in the western part of the basin. This northward transport is balanced by a southward flux of dissolved organic nitrogen in the Gulf Stream recirculation gyre. Remineralization of dissolved organic matter during its transit in the subtropical gyre supplies the required source of regenerated nitrate to the Gulf Stream. These results support the hypothesis that lateral transport and decomposition of slow or non-sinking organic matter contribute to the remineralization in the open ocean (Martin et al. 1987).

The model results suggest that the thermohaline overturning circulation and the Gulf Stream horizontal recirculation play important roles in the nutrient distribution of the North Atlantic. An estimate of the global new production of 2.3-3.6 mol-C m<sup>-2</sup> yr<sup>-1</sup>, or 9.5 to 14.9 Gt C yr<sup>-1</sup> is obtained.

The physical ocean circulation model is next tested in the seasonal mode, and then coupled with the kinetic model to investigate the oxygen seasonal cycle in the North Atlantic. The simulated temperature and density fields both show seasonal variation. The simulated oxygen seasonal cycle agrees well with results of observational studies and 1-dimensional model simulations. Photosynthetic processes produce oxygen supersaturation within the euphotic zone, with the maximum being located at a depth of about 75-80 m.

In the aphotic zone, most of the organic matter has been remineralized back to inorganic matter in the depth of 114-600 m. The onset of vertical mixing in late winter (February-April) brings up nitrate rich water to the surface layers, thus increasing new production. At the same time, there is a downward transport of oxygen. The model results suggest the oxygen utilization rate (OUR) below the euphotic zone provides a useful estimate of basin averaged new production.

A 1-dimensional time dependent particle cycling with two particle size classes is then developed, following Clegg and Whitfield (1990). The steady state solution of this model is first examined. The simulated total organic carbon concentration and large particle flux are consistent with observational studies and other 1-dimensional model simulations. The simulated aggregation and disaggregation processes occur reversibly throughout the water column, but mostly within the upper few hundred meters.

The large particles have a low mass ratio relative to the particulate organic carbon pool. The ratio of large to small particle concentration ranges from 5-6% in the surface layer in the upper 50 m, to about 2.5-3% at depths below 1000 m. The downward transport of organic carbon is mainly accomplished by the fast sinking large particles. These particles may play an important role in the downward transport of organic matter of surface origin to deeper layers.

The steady state version of the particle model is coupled with the 3-dimensional planetary geostrophic circulation model. The magnitudes of the simulated organic carbon flux and total organic carbon concentrations are comparable with observations. The domain averaged vertical profiles of total organic carbon and vertical large particle flux

are consistent with 1-dimensional model simulations and observational studies. We note that spatial variability of the model parameters, especially the aggregation/disaggregation rate constants, could be important in future 3-dimensional modelling studies.

## Bibliography

- Aldredge, A. L., The chemical composition of macroscopic aggregates in two neritic seas, *Limnol. Oceanogr.*, 24, 855-866, 1979.
- Aldredge, A. L., and E. O. Hartwig, Aggregate dynamics in the sea: workshop report, American institution of Biological Science, New York, 1987.
- Aldredge, A. L. and M. W. Silver, Characteristics dynamics and significance of marine snow, *Progress in Oceanography*, 20, 41-82, 1988.
- Aldredge, A. L. and C. C. Gotschalk, Direct observations of the mass flocculation of diatom blooms: Characteristics, settling velocities and formation of diatom aggregates, *Deep-Sea Res.*, 36, 159-171, 1989.
- Altabet, M. A., Variations in nitrogen isotopes composition between sinking and suspended particles: implication for nitrogen cycling and particle transformation in the open ocean, *Deep-Sea Res.*, 35, 535-554, 1988.
- Altabet, M. A., Particulate new nitrogen fluxes in the Sargasso Sea, *J. Geophys. Res.*, 94, 12771-12779, 1989.
- Altabet, M. A., W. G. Deuser, S. Honjo and C. Stienen, Seasonal and depth-related changes in the source of sinking particles in the North Atlantic, *Nature*, 354, 136-

139, 1991.

Anderson L. A., The determination of Redfield ratios for use in global oceanic nutrient cycle models, Ph.D thesis, 294pp., Princeton Univ., Princeton, N.J., 1993.

Anderson, L. A., and J. Sarmiento, Redfield ratios of remineralization determined by nutrient data analysis, *Global Biogeochem. Cycles*, 5, 65-81, 1994.

Anderson, R. F., M. P. Bacon and P. G. Brewer, Removal of  $^{230}\text{Th}$  and  $^{231}\text{Pa}$  from the open ocean, *Earth and Planet. Sci. Lett.*, 62, 7-23, 1983.

Archer, D., S. Emerson, T. Powell and C.S. Wong, Numerical hindcasting of sea surface  $\text{pCO}_2$  at Weathership Station Papa, *Prog. Oceanog.*, Vol. 32, 319-351, 1993.

Asper, V. L., Measuring the flux and sinking speed of marine snow aggregates, *Deep-Sea Res.*, 34, 1-17, 1987.

Bacastow, R., and E. Maier-Reimer, Dissolved organic carbon in modelling oceanic new production, *Global Biogeochem. Cycles*, 5, 71-85, 1991.

Bacon, M. P. and R. F. Anderson, Distribution of thorium isotopes between dissolved and particulate forms in the deep sea, *J. Geophys. Res.*, 87, 2045-2056, 1982.

Bacon, M. P., C. -A. Huh, A. P. Fleer and W.G. Deuser, Seasonality in the flux of natural radionuclides and plutonium in the deep Sargasso Sea, *Deep-Sea Res.*, 32, 273-286, 1985.

Bacon, M. P., Tracers of chemical scavenging in the ocean: boundary effects and large-scale chemical fractionation, *Philosophical Transaction of the Royal Society of London*, A325, 147-160, 1988.

Bennett, A. F. and W. B. White, Eddy heat flux in the subtropical North Pacific, *J.*

- Phys. Oceanogr.*, 16, 728-740, 1986.
- Bensen, B. B., Some thoughts on gases dissolved in the oceans, in *Proc. Symp. of Mar. Geochem.*, edited by D. R. Schink and J. T. Cotless, Univ. of Rhode Island Occasional Publ., No.3, 91-107, 1965.
- Berger W. H., V. S. Smetacek and G. Wefer, Ocean productivity and paleoproductivity-an overview, in *Productivity of the Ocean; Present and Past*, edited by W. H. Berger, V. S. Smetacek, and G. Wefer, p. 1-34, John Wiley and Sons, Chichester, 1989.
- Betzer P. R., W. J. Showers, E. A. Laws, C. D. Winn, G. R. Ditullio and P. R. Kroopnick, Primary productivity and particle fluxes on a transect of the equator at 153°W in the Pacific Ocean, *Deep-Sea Res.*, 31, 1-11, 1984.
- Bishop, J. K. B., D. R. Ketten and J. M. Edmond, The chemistry, biology and vertical flux of particulate matter from the upper 400m of the Cape Basin in the south-east Atlantic, *Deep-Sea Res.*, 25, 1121-1161, 1978.
- Bishop, J. K. B., R. Collier, D. R. Ketten and J. M. Edmond, The chemistry, biology and vertical flux of particulate matter from the upper 1500m of the Panama Basin, *Deep-Sea Res.*, 27, 615-640, 1980.
- Bishop, J. K. E., J. Stepien and P. H. Wiebe, Particulate matter distribution, chemistry and flux in the Panama Basin: response to environment forcing, *Progress in Oceanography*, 17, 1-59, 1986.
- Broecker W. S. and T. -H. Peng, Tracers in the sea, Eldigio Press, Palisades, New York, 1982.

- Bryan, F., Parameter sensitivity of primary equation ocean general circulation model, *J. Phys. Oceanogr.*, 17, 970-985, 1987.
- Bryan, K., A numerical method for the study of the circulation of the world ocean, *J. Phys. Oceanogr.*, 4, 347-376, 1969.
- Bryan, K., Models of the world ocean, *Dyn. Atmos. Oceans.*, 2, 327-338, 1979.
- Bryan, K. and L. J. Lewis, A water mass model of the world ocean circulation, *J. Geophys. Res.*, 84, 2503-2517, 1979.
- Buesseler K. O., M. P. Bacon, J. K. Cochran and H. D. Livingston, Carbon and nitrogen export during the JGOFS North Atlantic Bloom Experiment estimated from  $^{234}\text{Th}$ : $^{238}\text{U}$  disequilibria, *Deep-Sea Res.*, 39, 1115-1137, 1992.
- Buesseler K. O., H. D. Livingston, S. Honjo, B. J. Hay, T. Konuk and S. Kempe, Scavenging and particle deposition in the southwestern Black Sea-evidence from Chernobyl radiotracers, *Deep-Sea Res.*, 37, 413-430, 1990.
- Carlson, C. A., H. W. Ducklow, and A.F. Michaels, Annual flux of dissolved organic carbon from the euphotic zone in the northwestern Sargasso Sea, *Nature*, 371, 405-408, 1994.
- Cauwet, G., Organic chemistry of sea water particulates: concepts and developments, *Oceanol. Acta*, 1, 99-105, 1978.
- Chen, W. and P. J. Wangersky, A high-temperature catalytic oxidation method for the determination of marine dissolved organic carbon and its comparison with the UV photo-oxidation method, *Mar. Chem.*, 42, 95-106, 1993.
- Cho, B. C. and F. Azam, Major role of bacteria in biogeochemical fluxes in the ocean's

- interior, *Nature*, 332, 441-443, 1988.
- Clegg S. L. and M. Whitfield, A generalised model for scavenging of trace metals in the open ocean, I, Particle cycling, *Deep-Sea Res.*, 37, 809-832, 1990.
- Clegg S. L. and M. Whitfield, A generalised model for scavenging of trace metals in the open ocean, II, Thorium Scavenging, *Deep-Sea Res.*, 38, 91-120, 1991.
- Clegg S. L., M. P. Bacon and M. Whitfield, Application of a generalized scavenging model to thorium isotope and particle data at equatorial and high-latitude sites in the Pacific Ocean, *J. Geophys. Res.*, 96, 20655-20670, 1991.
- Clegg S. L., M. Whitfield, Application of a generalized scavenging model to time series  $^{234}\text{Th}$  and particle data obtained during the JGOFS North Atlantic Bloom Experiment, *Deep-Sea Res.*, 40, 1529-1545, 1993.
- Coale K. H. and K. W. Bruland,  $^{234}\text{Th}$ : $^{238}\text{U}$  disequilibria within the California Current, *Limnol. and Oceanogr.*, 30, 22-33, 1985.
- Coale K. H. and K. W. Bruland, Oceanic stratified euphotic zone as elucidated by  $^{234}\text{Th}$ : $^{238}\text{U}$  disequilibria, *Limnol. and Oceanogr.*, 32, 189-200, 1987.
- Cox, M. D. and K. Bryan, A numerical model of the ventilated thermocline, *J. Phys. Oceanogr.*, 14, 674-687, 1984.
- Cox, M. D., An eddy resolving numerical model of the ventilated thermocline, *J. Phys. Oceanogr.*, 15, 1312-1324, 1985.
- Craig H. and T.L. Hayward, Oxygen supersaturation in the ocean: Biological versus physical concentration and their application, *Science*, 235, 199-202, 1987.
- Druffel, E. R. M., P. M. Williams, J. E. Bauer and J. R. Ertel, Cycling of dissolved and

- particulate organic matter in the open ocean, *J. Geophys. Res.*, 97, 15639-15659, 1992.
- Dugdale, R. C., Nutrient limitation in the sea: Dynamics, Identification, and Significance, *Limnol. Oceanogr.*, 12, 685-695, 1967.
- Dugdale, R. C. and J. J. Goering, Uptake of new and regenerated forms of nitrogen in primary productivity, *Limnol. Oceanogr.*, 12, 196-206, 1967.
- Eisma, D., J. Boon, R. Groenewegen, V. Ittekkot, J. Kalf and W. G. Mook, Observations on macro-aggregates, particle size and organic composition of suspended matter in the Ems estuary, *Mitt Geol. Palaont. Inst., Univ. Hamburg*, 55, 295-314, 1983.
- Emerson, S., Seasonal oxygen cycles and biological new production in surface waters of the subarctic Pacific Ocean, *J. Geophys. Res.*, 92, 6535-6544, 1987.
- Emerson, S., P. Quay, C. Stump, D. Wilbur and M. Konx, O<sub>2</sub>, Ar, N<sub>2</sub> and <sup>222</sup>Rn in surface waters of the subarctic ocean: new biological O<sub>2</sub> production, *Global Biogeochem Cycles*, 5, 49-69, 1991.
- Emerson, S., P. Quay and P. Wheeler, Biological productivity determined from oxygen mass balance and incubation experiments, *Deep Sea Res.*, 40, 2351-2358, 1993.
- Eppley, R. W. and B. J. Peterson, Particulate organic matter flux and planktonic new production in the deep ocean, *Nature*, 282, 677-680, 1979.
- Esaias W. E., G. C. Feldman, C. R. McClain and J. A. Elrod, Monthly satellite-derived phytoplankton pigment distribution for the North Atlantic basin, *EOS, Trans. Amer. Geophys. Uni.*, 67, 835-837, 1986.
- Esbensen, S. K. and Y. Kushnir, Heat budget of the global ocean: Estimates from surface

- marine observations, *Report 29*, Climate Research Institute, Oregon State University, Corvallis, Oregon, 271pp, 1981.
- Farley, K. J. and F. M. M. Morel, Role of coagulation in the kinetics of sedimentation, *Environ. Sci. Technol.*, 20, 187-195, 1986.
- Fasham, M. J. R., J. L. Sarmiento, R. D. Slater, H. W. Duclow and R. Williams, A seasonal three-dimensional ecosystem model of nitrogen cycling in the North Atlantic euphotic zone: A comparison of the model results with observation from Bermuda Station 'S' and OWS 'India', *Global Biogeochem. Cycles*, 7, 379-415, 1993.
- Fiadero M. E. and H. Craig, Three-dimension modelling of tracers in the deep Pacific Ocean. I. salinity and Oxygen, *J. Mar. Res.*, 36, 323-355, 1978
- Fowler S. W. and G. A. Knauer, Role of large particles in the transport of elements and organic compounds through the oceanic water column, *Progress in Oceanography*, 16, 147-194, 1986.
- Fukumori, I., F. Martel and C. Wunsch, The hydrography of the North Atlantic in the early 1980s, An Atlas, *Progress in Oceanography*, 27, 1-110, 1991.
- Gaspar P., Modelling the seasonal cycle of the upper ocean, *J. Phys. Oceanogr.*, 18, 161-180, 1988.
- Gaspar P., Y. Gredoris and J.M.Lefebvre, Simple eddy kinetic energy model for simulation of the oceanic vertical mixing: test at station Papa and Lotus cite, *J. Geophys. Res.* 95, 16179-16194, 1990.
- Harrison, W. G., Regeneration of nutrients, in *Primary Productivity and Biogeochemical*

- Cycles in the sea*, edited by P. G. Falkowski and A. D. Woodhead, p. 385-407, Plenum Press, New York, 1992.
- Hellerman, S. and M. Rosenstein, Normal monthly wind stress over the world ocean with error estimates, *J. Phys. Oceanogr.*, *13*, 1093-1104, 1983.
- Honjo S., Seasonality and interaction of biogenic and lithogenic particulate flux at the Panama Basin, *Science*, *218*, 893-894, 1982.
- Honjo, S., Doherty, K. W., Agrawal, Y. C., Asper, V. L., Direct optical assessment of large amorphous aggregates (marine snow) in the deep ocean, *Deep-Sea Res.*, *31*, 67-76, 1984.
- Honeyman, B. D. and P. H. Santschi, A Brownian-pumping model for oceanic trace metal scavenging: evidence from Th isotopes, *J. Mar. Res.*, *47*, 951-992, 1989.
- Jackson, G. A. and P. M. Williams, Importance of dissolved organic nitrogen and phosphorus to biological nutrient cycling, *Deep Sea, Res.*, *32*, 223-235, 1985.
- Jackson, G. A., Implications of high dissolved organic matter concentration for oceanic properties and processes, *Oceanography*, *1(2)*, 28-33, 1988.
- Jackson, G. A., A model of the formation of marine algal flocs by physical coagulation processes, *Deep-Sea Res.*, *37*, 1197-1211, 1990.
- Jahne, B., Zur parameteterisierung des Gasaustausches mit Hilfe von Laborexperimenten, Doctoral Dissertation, University of Heidelberg, 124 p., 1980.
- Jahne, B., G. Heinz and W. Dietrich, Measurement of the diffusion coefficients of sparingly soluble gases in water, *J. Geophys. Res.* *92*, 10767-10776, 1987.
- Jahnke R. A., Ocean fluxes studies: a status report, *Rev. of Geophys.*, *28*, 381-391,

1990.

Jenkins, W. J., Oxygen utilization rates in North Atlantic sub-tropical gyre and primary production in oligotrophic system, *Nature*, 300, 246-248, 1982.

Jenkins, W. J. and J. C. Goldman, Seasonal oxygen cycling and primary production in the Sargasso Sea, *J. Mar. Res.*, 43, 465-491, 1985.

Jenkins, W. J., The use of anthropogenic tritium and helium-3 to study subtropical gyre ventilation and circulation, *Phil. Trans. R. Soc., London, Ser. A*, 325, 43-56, 1988.

Johnson, B. D. and P. E. Kepkay, Colloid transport and bacterial utilization of oceanic DOC, *Deep-Sea Res.*, 39, 855-869, 1992.

Joos, F., J. L. Sarmiento and U. Siegenthaler, Estimates of the effect of Southern Ocean iron fertilization on atmospheric CO<sub>2</sub> concentration, *Nature*, 349, 772-775, 1991a.

Joos, F., U. Siegenthaler and J. L. Sarmiento, Possible effects of iron fertilization in the Southern Ocean on atmospheric CO<sub>2</sub> concentration, *Global Biogeochem. Cycles*, 5, 135-150, 1991b.

Karl, D. M. and G. A. Knauer, Vertical distribution, transport, and exchange of carbon in the northeast Pacific Ocean: evidence for multiple zones of biological activity, *Deep-Sea Res.*, 31, 221-243, 1984.

Kepkay, P. E., Particle aggregation and the biological reactivity of colloids, *Mar. Ecol. Prog. Ser.*, 109, 293-304, 1994.

Kirchman D.I., Y. Suzuki, C. Garside and H.W. Ducklow, High turnover rates of dissolved organic carbon during a spring phytoplankton bloom, *Nature*, 352, 612-614, 1991.

- Krishnaswami, S., D. Lal, B. L. K. Smoayajulu, R. F. Weiss and H. Craig, Large-volume *in situ* filtration of deep Pacific waters: Mineralogical and radioisotope studies, *Earth and Planet. Sci. Lett.*, *32*, 420-429, 1976.
- Knauer, G. A. and J. H. Martin, Primary production and carbon-nitrogen fluxes in the upper 1500 m of the Northeast Pacific, *Limnol. Oceanogr.*, *26*, 181-186, 1981.
- Kolber, Z. S., R. T. Barber, K. H. Coale, S. E. Fitzwater, R. M. Greene, K. S. Johnson, S. Lindley and P. G. Falkowski, Iron limitation of phytoplankton photosynthesis in the equatorial Pacific Ocean, *Nature*, *371*, 145-149, 1994.
- Kranck, K. and T. Milligan, T., Macflocs from diatoms: *in situ* photography of particles in Bedford Basin, Nova Scotia, *Mar. Ecol. Prog. Ser.*, *44*, 183-189, 1988.
- Kurz K. D. and E. Maier-Reimer, Iron fertilization of the austral ocean -the Hamburg model assessment, *Global Biogeochem. Cycles*, *7*, 229-244, 1993.
- Lee, C. and S. G. Wakeham, Organic matter in seawater: biogeochemical processes, in *Chemical Oceanography, Vol. 9*, edited by J. P. Riley and R., Chester, p. 248-289, Academic Press, 1988.
- Levitus, S., Climatological atlas of the world ocean, *NOAA Prof. Pap.*, *13*, U.S. Government Printing Office, Washington, D.C., 1982.
- Liss, P.S. and L. Merlivat, Air-sea gas exchange rates: Introduction and synthesis, in *The Role of Air-Sea Exchange in Geochemical Cycling*, edited by Buat Menard, p. 113-127, D. Reidel, 1986.
- Longhurst, A. R. and W. G. Harrison, The biological pump: Profiles of plankton production and consumption in the upper ocean, *Prog. Oceanogr.*, *22*, 47-122,

1989.

Martin J. H., G. A. Knauer, D. M. Karl, and W. W. Broenkow, Vertex: Carbon cycling in the Northeast Pacific, *Deep-Sea Res.*, 34, 267-285, 1987.

Martin J. H., Glacial-interglacial CO<sub>2</sub> Change: The iron hypothesis, *Paleoceanography*, 5, 1-13, 1990.

Martin, J. H., K. H. Coale, K. S. Johnson, S. E. Fitzwater, R. M. Gordon, S. J. Tanner, C. N. Hunter, V. Elrod, J. Nowicki, T. Coley, R. Barber, S. Lindley, A. Watson, K. Van Scoy, C. Law, M. Liddicoat, R. Ling, T. Stanton, J. Stockel, C. Collins, A. Anderson, R. Bidigare, M. Ondrusek, M. M. Latasa, F. Millero, K. Lee, W. Yao, J. Zhang, G. Friederich, C. Sakamoto, F. Chavez, K. Buck, Z. Kolber, R. Greene, P. Falkowski, S. Chisholm, F. Hoge, B. Swift, S. Turner, P. Nightingale, P. Liss and N. Tindale, The iron Hypothesis: Ecosystem tests in Equatorial Pacific waters, *Nature*, 371, 123-129, 1994.

McCave I. N., Vertical fluxes of particles in the ocean, *Deep-sea Res.*, 22, 491-502, 1975.

McCave I. N., Size spectra and aggregation of suspended particles in the deep ocean, *Deep-Sea Res.*, 31, 329-352, 1984.

Mellor, G. L. and Yamada, T., A hierarchy of turbulence closure models for planetary boundary layers, *J. Atmos. Sci.*, 31, 1791-1806, 1974.

Mellor, G. L. and T. Yamada, A development of a turbulence closure model for geophysical fluid problems, *Rev. Geophys. Space Phys.*, 20, No. 4, 851-875, 1982.

- Meybeck M, Carbon, nitrogen and phosphorus transport by world rivers, *American Journal of Science*, 282, 402-450, 1982.
- Moore R. M. and K. A. Hunter, Thorium adsorption in the ocean: reversibility and distribution amongst particle sizes, *Geo himica et Cosmochimica Acta*, 49, 2253-2257, 1985.
- Murray, J. W., J. N. Downs, S. Strom, C.-L. Wei and H. W. Jannasch, Nutrient assimilation, export production and  $^{234}\text{Th}$  scavenging in the eastern equatorial Pacific, *Deep Sea Res.*, 35, 1471-1489, 1989.
- Murray, J. W., R. T. Barber, M. R. Roman, M. P. Bacon and R. A. Feely, Physical and biological controls on carbon cycling in the equatorial Pacific, *Science*, 266, 58-65, 1994.
- Musgrave, D. L., J. Chou and W. J. Jenkins, Application of a model of upper ocean physics for studying seasonal cycles of oxygen, *J. Geophys. Res.*, 93, 15679-15700, 1988.
- Najjar, R. G., Simulations of the phosphorus and oxygen cycles in the world ocean using a general circulation model, Ph.D thesis, 190 p., Princeton Univ., Princeton, N.J., 1990.
- Najjar, R., J. L. Sarmiento and J. R. Toggweiler, Downward transport and fate of organic matter in the ocean: simulations with a general circulation model, *Global Biogeochemical Cycles*, 6, 45-76, 1992.
- Nozaki Y., H.-S. Yang and M. Yamada, Scavenging of thorium in the ocean, *J. Geophys. Res.*, 87, 2045-2056, 1987.

- O'Melia, C. R., Particle-particle interactions, in *Aquatic surface chemistry*, edited by W. Stumm, p. 385-404, John Wiley & Sons, New York, 1987.
- O'Melia, C. R. and C. L. Tiller, Physicochemical aggregation and deposition in aquatic environments, in *Environmental Particles, Vol. 2*, edited by J. Buffle and H. P. van Leeuwen, International Union of Pure and Applied Chemistry, Environmental Analytical and Physical Chemistry Series, p. 353-385, Lewis Publishers, Ann Arbor, 1993.
- Parkard, T.T., M. Denis, M. Rodier and P. Garfield, Deep-ocean metabolic CO<sub>2</sub> production: calculation from ETS activity, *Deep Sea Res.*, *35*, 371-382, 1988.
- Platt, T. D., D. V. Subba Rao, J. C. Smith, W. K. Li, B. Irwin, E. P. W. Horn and D. D. Sameoto, Photosynthetically-competent phytoplankton from the aphotic zone of the deep ocean, *Mar. Ecol. Prog. Ser.*, *10*, 105-110, 1983.
- Platt T. and W. G. Harrison, Biogenic fluxes of carbon and oxygen in the ocean, *Nature*, *318*, 55-58, 1985.
- Peng, T-H. and W. S. Broecker, Dynamical limitations on the Antarctic iron fertilization strategy, *Nature*, *349*, 227-229, 1991a.
- Peng T-H. and W. S. Broecker, Factors limiting the reduction of atmospheric CO<sub>2</sub> by iron fertilization, *Limnol. Oceanogr.*, *36*, 1919-1927, 1991b.
- Price, J. F., R. A. Weller and R. Pinkle, Diurnal cycling: observations and models of the upper ocean response to diurnal heating, cooling and wind mixing, *J. Geophys. Res.*, *91*, 8411-8427, 1986.
- Quay, P.D., S. Emerson, D.O. Wilbur, C. Stump and M. Knox, The  $\delta^{18}\text{O}$  of dissolved

- O<sub>2</sub> in the surface waters of the subarctic Pacific: a tracer of biological productivity, *J. Geophys. Res.*, 98, 8447-8453, 1993.
- Redfield, A. C., B. H. Ketchum and F.A. Richards, The influence of organism on the composition of seawater, in *The sea*, edited by M. N. Hill, Vol.2, 26-77, Interscience, New York, 1963.
- Reid J. L., Distribution of dissolved oxygen in the summer thermocline, *J. Mar. Res.*, 20, 138-148, 1962.
- Ridal, J. J. and Moore, R. M., Resistance to UV and persulfate oxidation of dissolved organic carbon produced by selected marine phytoplankton, *Mar. Chem.*, 42, 167-188, 1993.
- Riebesell, U., Particle aggregation during a diatom bloom. I. Physical, *Mar. Ecolo. Prog. Ser.*, 54, 273-280, 1991a.
- Riebesell, U., Particle aggregation during a diatom bloom. II, Biological aspects. *Mar. Ecolo. Prog. Ser.*, 54, 281-291, 1991b.
- Riebesell, U., Comparison of sinking and sedimentation rate measurements in a diatom winter/spring bloom, *Mar. Ecolo. Prog. Ser.*, 54, 109-119, 1989.
- Riley, G. A., Organic aggregates in seawater and the dynamics of their formation and utilization, *Limnol. Oceanogr.*, 8, 372-381, 1963.
- Rintoul, S. R., and C. Wunsch, Mass, heat, oxygen and nutrient fluxes and budgets in the North Atlantic Ocean, *Deep Sea Res.*, 38, Suppl. 1, S355-377, 1991.
- Ryther J. H., Photosynthesis and fish production in the sea. The production of organic matter and its conversion to higher forms of life vary throughout the world ocean,

*Science*, 166, 72-76, 1969.

Santschi, P. H. and B. D. Honeyman, Radioisotopes as tracers for interactions between trace elements colloids and particles in natural waters, in *Trace metals in the environment 1, Heavy metals in the environment*, edited by J.-P. Vervet, p. 229-246, Elsevier, New York, 1991a.

Santschi, P. H. and B. D. Honeyman, Are thorium scavenging and particle fluxes in the ocean regulated by coagulation? in *Radionuclides in the study of marine processes*, edited by P. J. Kershaw and D. S. Woodhead, Elsevier Applied Science, New York, 1991b.

Sarmiento, J. L., Thiele, G., Key, R. M. and Moore, W. S., Oxygen and nitrate new production and remineralization in the North Atlantic subtropical gyre, *J. Geophys. Res.*, 95, 18303-18317, 1990.

Sarmiento, J. L. and J. C. Orr, Three-dimensional simulations of the impact of South Ocean nutrient depletion on atmospheric CO<sub>2</sub> and ocean chemistry, *Limnol. Oceanogr.*, 36, 1928-1950, 1991.

Sarmiento, J. L., R. D. Slater, M. J. R. Fasham, H. W. Ducklow, J. R. Toggweiler and D. T. Evan, A seasonal three-dimensional model of nitrogen cycling in the North Atlantic euphotic zone, *Global Biogeochem. Cycles*, Vol. 7, No.2, 417-450, 1993.

Sharp, J. H., The dissolved organic carbon controversy: an update, *Oceanography*, 6, 45-50, 1993.

Sharp, J. N., R. Bennet, C. A. Carlson, R. Dow and S. E. Fitzwater, Re-evaluation of high temperature combustion and chemical oxidation for measurements of

- dissolved organic carbon in seawater, *Limnol. Oceanogr.*, 38, 1774-1782, 1994.
- Shulenberger E. and J.L. Reid, The Pacific shallow oxygen maximum, deep chlorophyll maximum, and primary productivity, reconsidered. *Deep-Sea Res.*, 28, 267-271, 1986.
- Siegenthaler, U., and J. L. Sarmiento, Atmospheric carbon dioxide and the ocean, *Nature*, 365, 119-125, 1993.
- Silver, M. W. and M.M. Gowing, The 'Particle' flux : origins and biological components, *Progress in Oceanography*, 26, 74-113, 1991.
- Silver, M. W., M. M. Gowing and P. J. Davoll, The association of photosynthetic picoplankton and ultraplankton with pelagic detritus through the water column (0-2000m), in *Photosynthetic Picoplankton*, edited by T.Platt and W.K.W. Li, *Can. Bull. Fish. Aq. Sci.*, 214, 311-341, 1986.
- Silver, M. W., Alldredge, A. L., Bathypelagic marine snow: deep-sea algal and detrital community, *J. Mar. Res.*, 39, 501-530, 1981.
- Smetacek, V.S., Role of sinking on diatom life-history cycles: ecological evolutionary and geological significance, *Mar. Biol.*, 84, 239-251, 1985.
- Spitzer W.S. and W.J. Jenkins, Rates of vertical mixing, gas exchange and new production: Estimates from seasonal gas cycles in the upper ocean near Bermuda, *J. Mar. Res.*, 47, 169-196, 1989.
- Su L., C. A. Lin and K. L. Denman, Nitrogen cycles modelling of the North Atlantic Ocean, submitted to *Global Biogeochem. Cycles*, 1994.
- Suess E., Particulate Organic carbon flux in the ocean-surface productivity and oxygen

- utilization, *Nature*, 288, 260-263, 1980.
- Sugimura, Y. and Y. Suzuki, A high-temperature catalytic oxidation method for the determination of non-volatile dissolved organic carbon in seawater by direct injection of a liquid sample, *Mar. Chem.*, 24, 105-131, 1988.
- Takahashi, T., W. S. Broecker and S. Langer, Redfield ratio based on chemical data from isopycnal surfaces, *J. Geophys. Res.*, 90, 6904-6924, 1985.
- Thomas, F., J. F. Minster, P. Gaspar and Y. Gregoris, Comparing the behaviour of two ocean surface models in simulating dissolved O<sub>2</sub> concentration at O.W.S.P, *Deep Sea Res.*, 40, 395-408, 1993.
- Thomas, F., V. Garson and J. F. Minster, Modelling the seasonal cycle of dissolved oxygen in the upper ocean at Ocean Weather Station P, *Deep Sea Res.*, 37, 463-491, 1990.
- Toggweiler, J. R., Deep-sea carbon, A burning issue, *Nature*, 334, 468, 1988.
- Toggweiler, J. R., Is the downward dissolved organic matter flux important in the carbon transport? in *Productivity of the Ocean; Present and Past*, edited by W. H. Berger, V. S. Smetacek, and G. Wefer, p. 65-83, John Wiley and Sons, Chichester, 1989.
- Toggweiler, J. R., K. Dixon, and K. Bryan, Simulations of radiocarbon in a coarse-resolution world ocean model 1: Steady state distributions, *J. Geophys. Res.*, 4, 8217-8742, 1989a.
- Toggweiler, J. R., K. Dixon, and K. Bryan, Simulations of radiocarbon in a coarse-resolution world ocean model 2: Distributions of bomb-produced <sup>14</sup>C, *J. Geophys.*

- Res.*, 94, 8243-8264, 1989b.
- Trent, J. D., A. L. Shanks and M. W. Silver, *In situ* and laboratory measurements on macroscopic aggregates in Monterey Bay, California, *Limnol. Oceanogr.*, 23, 626-635, 1978.
- Volk, T. and M. I. Hoffert, Ocean carbon pumps: analysis of relative strengths, in *Carbon Dioxide and the Carbon Cycle, Archean to Present*, Geophys, edited by W.S. Broecker. Monogr. Ser., vol. 32, 99-110, AGU, Washington, D.C., 1985.
- Wakeham S. G. and E.A. Canuel, Organic geochemistry of particulate matter in the eastern tropical North Pacific Ocean: implication for particle dynamics, *J. Mar. Res.*, 46, 183-213., 1988.
- Walsh I., J. Dymond and R. Collier, Rates of recycling of biogenic components of settling particles in the ocean derived from sediment trap experiments, *Deep Sea Res.*, 35, 43-58, 1988.
- Watson, A. J., C. S. Law, K. A. Van Scoy, F. J. Millero, W. Yao, G. Friederich, M. I. Liddicoat, R. H. Wanninkhof, R. T. Barber and K. Coale, Implications of the "Ironex" iron fertilisation experiment for atmospheric carbon dioxide concentrations, *Nature*, 367, 447-450, 1994.
- Warren, B.A., The insensitivity of subtropical mode water characteristic to meteorological fluctuations, *Deep Sea Res.*, 19, 1-20, 1972.
- Wells, J. T. and A. L. Shanks, Observations and geologic significance of marine snow in a shallow-water, partially enclosed marine embayment, *J. Geophys. Res.*, 92, 13185-13190, 1987.

- Weiss, R., The solubility of nitrogen, oxygen and argon in water and seawater, *Deep Sea Res.*, 17, 721-735, 1970.
- Wunsch, C., The general circulation of the North Atlantic west of 50°W determined from inverse methods, *Rev. Geophys. and Spa. Phys.*, 10, 751-285, 1978.
- Zhang, S., C. A. Lin and R. J. Greatbatch, A thermocline model for ocean climate studies, *J. Mar. Res.*, 50, 99-124, 1992.
- Zhang, S., R. J. Greatbatch and C. A. Lin, A reexamination of the polar haloline catastrophe and implications for coupled ocean-atmosphere modelling, *J. Phys. Oceanogr.*, 23, 287-299, 1993.
- Zhang, S., C. A. Lin and R. J. Greatbatch, A decadal oscillation due to the coupling between an ocean circulation model and a thermodynamic sea-ice model, *J. Mar. Res.*, 53, 79-106, 1995.